A study of monomer liquid mixtures and polymer network formation at a solid surface using molecular dynamics

Joao Gregorio

Department of Chemical Process and Engineering
University of Strathclyde, Glasgow

February 21, 2023

This thesis is the result of the author's original research. It has been composed by the author and has not been previously submitted for examination which has led to the award of a degree.

Acknowledgements

I would like to start by thanking both my supervisors Dr. Karen Johnston and Dr. Paul Mulheran for all the hard work and patience they put into guiding me during this journey. None of this would have been possible without their combined effort in mentoring me during my Ph.D project.

A note of thank you also to Dr. Dominic Wadkin-Snaith for his role in my supervision and for proving a link with Solvay, which co-funded this Ph.D project. Our discussions and exchanges of ideas proved invaluable for the completion of this work.

I would also like to thank all my friends in Glasgow, in and outside of the Department of Chemical and Process Engineering, that helped me during this journey: Sofia Alves, Carla Ferreira, Carlota Mendez, Georgia Sanxaridou, Cecilia Barrera, Daria Stoliaskaia, David McKechnie, Martin Prostredny, Michael Chrubasik, Neret Pujol-Navarro, Paul Duncan, Robert Roy, Ruben Rosario, Russell Miller, Sarahjane Wood and Scott Davidson. Thank you all so very much for your friendship and for making it so easy for me find a welcoming place in this city.

I would like to give a very special thanks to my good friend Rui Apostolo for his continued friendship and support, both on professional and personal settings. May our friendship endure, and when this is all done the first dram in on me.

My warmest and most sincere thank you goes to the love of my live. Thank you, Filipa Silva, for always being there for me, for all your unconditional support, for believing in me when I ever doubted myself, for always caring for me, and for always loving me. I cannot fully express in words how thankful I am to you.

Finally, I want to thank both my mom and dad for all that they have done for me. This is as much my achievement as it is yours. I also want to leave a special thank you, and a very thigh hug, to my younger brother for always believing in me. Never give up, I have no doubt you will achieve great things in live.

Abstract

Fibre-reinforced composites are used in a wide variety of industries for their light weight, high strength and durability. However, the structure of the polymer matrix near the fibre interface is not well understood and difficult to characterise experimentally. The aim of this project is to use molecular dynamics (MD) simulations to elucidate the effect of a fibre on polymer network structure.

The DREIDING force field has been widely used, in molecular simulations, to predict thermomechanical properties in reinforced epoxy composites, such as the well-known EPON-862/DETDA matrix. This work compares four variations of this force field with OPLS and presents the structural and dynamical properties of the liquids. The OPLS force field is deemed appropriate to study such systems and presents several advantages over DREIDING force field variations, such as a ease of use. Results show that there is a distinct interface region adjacent to the carbon fibre-like surface that differs from the centre region. Additionally, density, molecular orientation, and molecular conformation away from the surface match values found in bulk.

To study the effects of crosslinking, we have developed a generic bead-spring model to investigate polymerisation near a surface. The model is based on a Lennard-Jones (LJ) liquid in conjunction with the Kremer-Grest model, at constant pressure, and with a probabilistic approach towards achieving bond formation between individual monomer particles. This model was easily implemented, in LAMMPS, and was also used to study the properties of liquids and liquid mixtures near a surface. The same distinct interface region adjacent to the surface was also observed.

The polymerisation mechanism, by which crosslinking occurred, was representative of a step-growth mechanism, with and without the surface present. T is consistent with the epoxy curing process, represented by the aforementioned EPON-862/DETDA system. Additionally, it was verifiable that when a particular chemical species adsorbs to the surface more strongly, other molecular species are displaced from the interface region and move towards the centre film region. The resulting sterochemical

imbalance can cause the resulting crosslinked network to contain higher amounts of non-bonded monomers.

Often, carbon fibre surfaces dipped into epoxy resins (e.g. EPON-862) prior to inserting them in a epoxy/hardener mixture, in an attempt to improve surface adhesion. The stoichimetric imbalance shown to exist near the surface is further aggravated by this procedure and leads to a cured material of lower quality. This work sets the precedent for review of such fibre sizing procedures. In addition, the developed bead-spring crosslinking model allows for quick and efficient similar studies

Contents

List of Figures

List of Tables

List of Tables

1. Introduction

The purpose of this work is to gain insight into the liquid structure of pre-polymer liquids near the surfaces of reinforcement carbon fibres and to better understand how the structural changes in the liquid propagate to the cured material and affect the properties of polymer composites. Molecular dynamics (MD) simulations are used as a tool to explore this effect due to their capacity to study the small region that is the interface between fibre and polymer matrix. A polymer composite material is a material formed by at least two separate, and different components where at least one of them is a polymer [15, 26, 27]. They are not considered mixtures or solid solutions, since their individual components, in regards to their chemical and physical structure, are fully separate within the polymer composite.

Fibre-reinforced composites are widely used throughout industry in a great variety of applications ranging from coatings to structural components. One example of such can be found in the aviation industry, where the Airbus A350 is made of more than 50% carbon fibre reinforced polymers [65, 86].

Carbon-fibre reinforced polymers (CFRP) are a specific type o composite materials, which consist on polymer matrices reinforced by carbon fibres inserted in their structure as the reinforcement material [15, 26, 27]. The orientation of carbon fibre in the reinforced materials defines if it is a good thermal and electrical conductor or insulator depending on fibre orientation [26].

The adhesion between the fibre and the polymer matrix greatly affect the quality and properties of the composite material, hence they have been object of study, with epoxy resins being of particular interest given their wide range of applications and versatility [72]. The presence of a fibre creates an interface region where the polymer has a more dominant crystalline structure than the bulk.

Understanding the interactions in interface between fibres and polymer is fundamental towards improvement of polymer composite manufacture and properties. This work focus on exploring molecular behaviour in this region to gain insight into the

molecular structure of cured CFRPs and their properties.

1.1 Organisation of thesis

The background chapter (chapter 2) describes the structure of carbon fibre reinforced composites, and reviews literature studies that address the adhesion between the carbon fibres and the reinforced polymer matrices. A methodology chapter (chapter 3) in which molecular dynamics is detailed as a simulation-based methodology for the research that is carried out in the remainder of this work.

Chapter 4 studies how a graphitic surface affects the liquid structure of a liquid EPON-862/DDS model system, without any curing taking place. Several force fields are explored on a bulk system, without any carbon fibre surfaces, and the selected force field is utilised to study the interactions of the pre-polymer mixture near a carbon fibre surface. This chapter also forms the basis for a manuscript in preparation.

In chapter 5, I develop a crosslinking algorithm capable of simulating crosslinking using a generic polymer model system. The method consists on a mixture between the Kremer-Grest and the Lennard-Jones liquid models and achieves at accurately reproducing a crosslinking reaction.

This algorithm is applied in chapter 6 to study the effects that a surface has on liquid structure of binary polymer mixtures and how those effects propagate into the crosslinked network.

The last chapter contains a brief conclusion (chapter 7) summarising all the findings of the previous three results chapters. The appendices give all force field parameters utilised in this work.

2. Background

This chapter is focused on reviewing relevant literature in the context of carbon fibre reinforced polymers. The structure of carbon fibres is described, both on a macroscopic and molecular level. Precursor materials for carbon fibres are also discussed in the context of their manufacture. The concept of carbon nanotubes is also introduced, and differences between traditional carbon fibres and carbon nanotubes are also explored.

This is followed by a literature review on studies addressing: current methods of carbon fibre (and nanotube) reinforced composite manufacture and processing; typical properties of carbon fibre reinforced composites; the current state of the art in terms of improving adhesion between the carbon fibre surfaces and the polymer matrices; and a specific look at epoxy-based carbon fibre composites. This last topic stems from the fact that, currently, epoxy-based carbon fibre reinforced composites are the most widely utilised composite materials in the world [15, 26, 27].

Lastly, a brief introduction on the computational simulation of carbon fibre reinforced composites is provided, before being fully addressed in chapters 4 and 5.

2.1 Polymer composites and carbon fibre reinforced composites

Composite materials are used in a wide variety applications, which range from high-end applications within the aerospace and aeronautical industries, to having lower-end uses as components in sports gear and as insulation materials [42, 63, 111]. Typically higher-end application require the carbon fibres to be of better quality (i.e. Carbon fibres with higher carbon content and greater crystalline structure), which requires great care during their manufacture process, while lower-end applications usually utilise lower quality carbon fibres which are cheaper to make in industrial settings. Fibre composites have become a commonplace material in recent years. Out of the several fibre composite materials, carbon fibre reinforced composites are currently re-

garded as the material of choice in replacement of traditional aluminium alloys in the aeronautical sector [16]. This has shown to decrease weight of specific aircraft parts by between 20% and 40%, while maintaining the structural integrity of aircraft [111]. Additionally, complex shapes are easier to fabricate, when using composite materials instead of traditional alloys, reducing the number of parts necessary for the aircraft and minimising waste [111]. However, they are also more costly to manufacture and repair than traditional alloys and are more prone impact damage.

2.1.1 Structure of carbon fibre reinforced composites

Composite materials are made of two distinct phases: the carbon fibre and the polymer matrix; with different individual properties, and bonding or adhesion between these phases directly relates to the structural integrity of the composite. Typically, each individual fibre is very stiff and has a high strength to weight ratio, meaning that they are able to resist breaking or cracking despite being lightweight [91]. Individual fibres can also be braided together to form filaments, which can be woven to create carbon fibre fabric. Similarly to graphitic sheets, the fibres in a carbon filaments may not all share the same relative orientation to each other, making carbon filaments amorphous to some degree [20]. Sheets of carbon fibre fabric can be stacked with each other and with alternating polymer layers to form laminate composite materials. These materials retain most of the properties of carbon fibre, while having added flexibility due to the polymer material. However, laminate composites are still prone to failure. Two of the most common types of critical failure in carbon fibre reinforced composite materials are fibre pull-out and delamination, and both occur almost exclusively due to lack of adhesion between the carbon fibres and the polymer matrix.

Fibre pull-out failure consists of the carbon fibres embedded in the polymer matrix sliding out from the polymer matrix due to week surface-matrix adhesion [15]. Delamination occurs in laminate composites, where layers of woven carbon fibre fabric are layered with coats of polymer material, and consists of multiple layers separating and breaking. It also results from lack of adhesion between the carbon surface and polymer matrix, although it can be advanced by impacts suffered by the compos-

ite [10, 30]. Delamination can also result in secondary cracking of the polymer matrix and fibre fracture, as shown in Figure 2.1 [56].

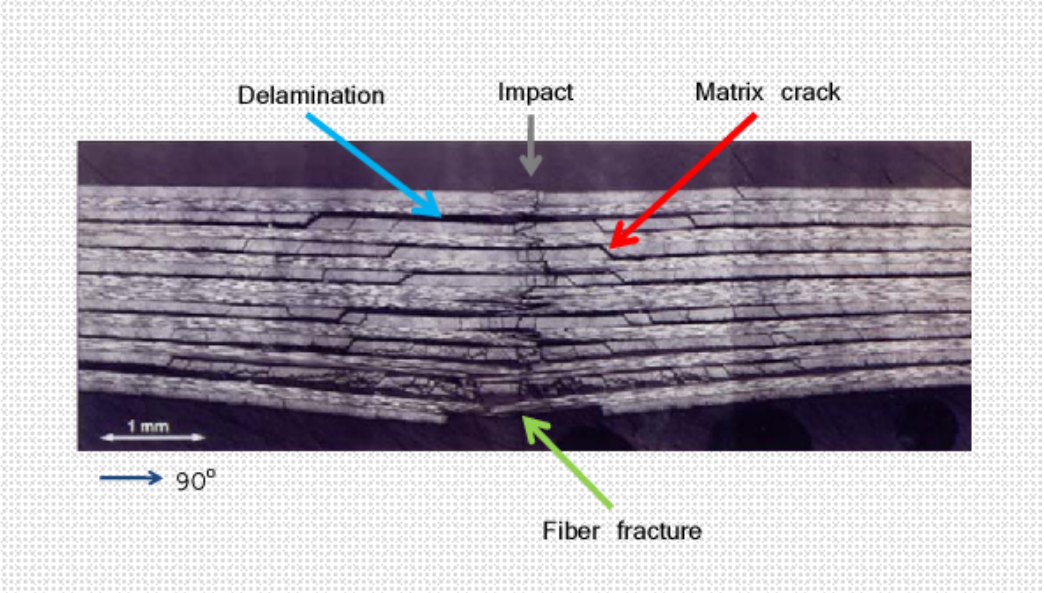

Figure 2.1: Highlight of composite delamination to to impact. Retrieved from "Computers Structures" [56] with permission from Elsevier.

Due to the nature of both these failure mechanisms, understanding how the carbon fibres and polymer matrices interact becomes extremely relevant in order to manufacture improved carbon fibre composites with increase resistance to failure. Lack of affinity between the carbon fibre surfaces and the polymer matrices is the key factor that leads to these failure mechanisms. This work will focus on researching these interactions in order to better understand them. The chemical structure of the fibre surface and its respective roughness also greatly determine how well the adhesion between both phases takes place [93].

The inherent roughness of the carbon surface itself can improve or worsen adhesion by physical effects instead of chemical effects, while the chemical surface of the carbon fibre can be modified via the grafting of functional groups to the surface to improve its adhesion with the polymer matrix [27].

2.2 Structure and properties of carbon fibre surfaces

Carbon fibres typically consist of aligned layers of graphene sheets, carbon atoms arranged in a planar hexagonal lattices resembling a honeycomb pattern, of varying diameters between 5 and 10μm, as is shown in Figure 2.2. These sheets are mostly composed of carbon atoms, however impurities may be contained within the lattice structure making the designation of ”graphitic sheets” more accurate for describing them. In addition, individual graphitic sheets in carbon fibres may not share the same relative orientation to one another, breaking planar symmetry of the fibres themselves, as is also shown in Figure 2.2.

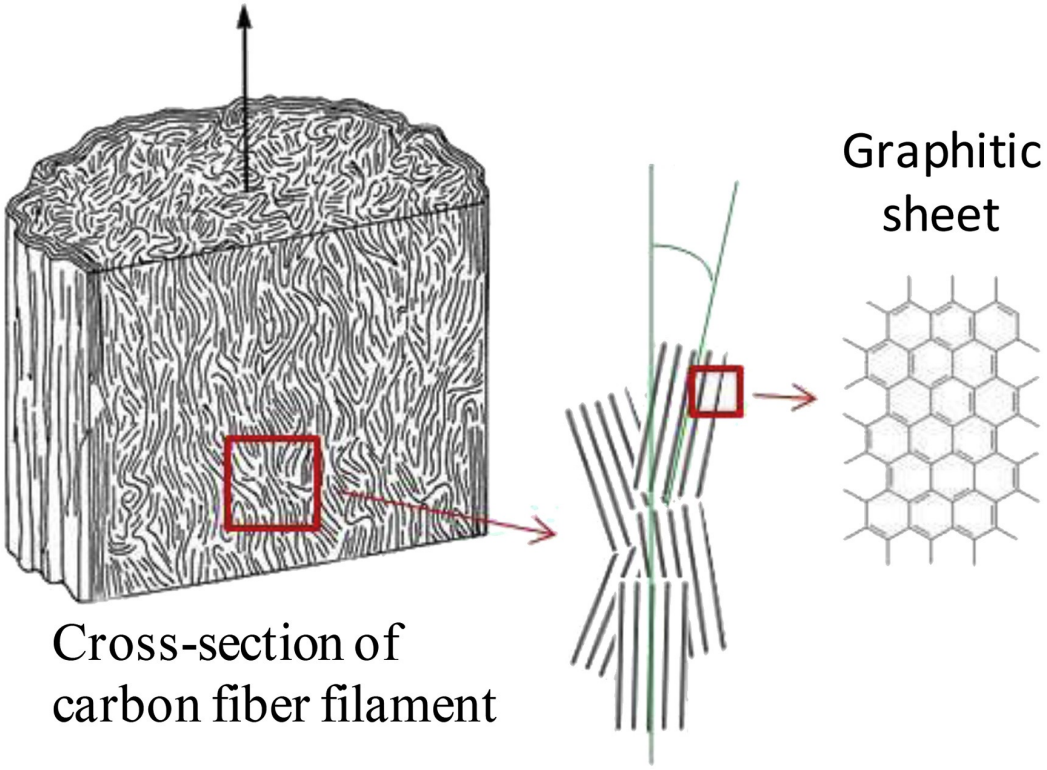

Figure 2.2: Internal structure of carbon fibres. Retrieved from ”Carbon” [20] with permission from Elsevier.

Both the degree of crystallinity and purity of the carbon fibres, are key factors which affect their properties [86]. Depending on these factors, carbon fibres are classified into three types, which also relate to their overall quality. Type I and type II fibres both

exhibit a high percentage of crystalline carbon. However, type I fibres have a greater overall percentage of carbon, meaning that long-range ordering of individual fibres is greater than in type II fibres, which has individual fibres arranged more amorphously. While type I and type II fibres display anisotropic properties, due to their greater percentage of crystalline structure, type III fibres are isotropic, given their greatly amorphous structure [86, 91].

Type I carbon fibres are characterised by having a higher Young's modulus, which means that high amounts of stress are required to manifest tangible strain on the fibres. Type II carbon fibres, on the other hand, have greater strength and are more deformation resistant. Lastly, type III carbon fibres have bow low Young's modulus and low strength. In terms of performance, type I fibres are utilised for high-end applications, followed by type II fibres in medium-to-high end applications. Type III fibres are advantageous only in terms of their manufacturing cost, which is lower than both two other fibre types, and are utilised for mainstream applications where performance is not the most relevant factor [91]. Typically, type I fibres are reserved for high-end applications, such as critical components in the aeronautical sector, while Type II fibres are generally used for non-critical applications in the same sectors. Type III fibres find their use in insulation materials and in sports equipment.

A highly relevant and specific type of carbon fibre are carbon nanotubes, which consist of a single graphitic sheet rolled onto itself. Carbon nanotubes can be single walled (SWCNT) when they consit of a single sheet of graphitic carbon or multi walled (MWCNT) when they consist of multiple concentrical sheets, as shown in Figure 2.3 [96].

Much like typical carbon fibres, rolling a graphic sheets onto themselves destroys the planar geometry of the structure, however, and unlike typical carbon fibres, it also creates directionality along the axis on which the sheet is rolled. Because of this added dimension, the ratio between length and thickness of the nanotube.

In addition, because carbon nanotubes are composed of rolled graphitic sheets, they tend to have increased thermal and electrical conductivity. This is because electrons are not subject to the need to transition between different graphitic sheets and

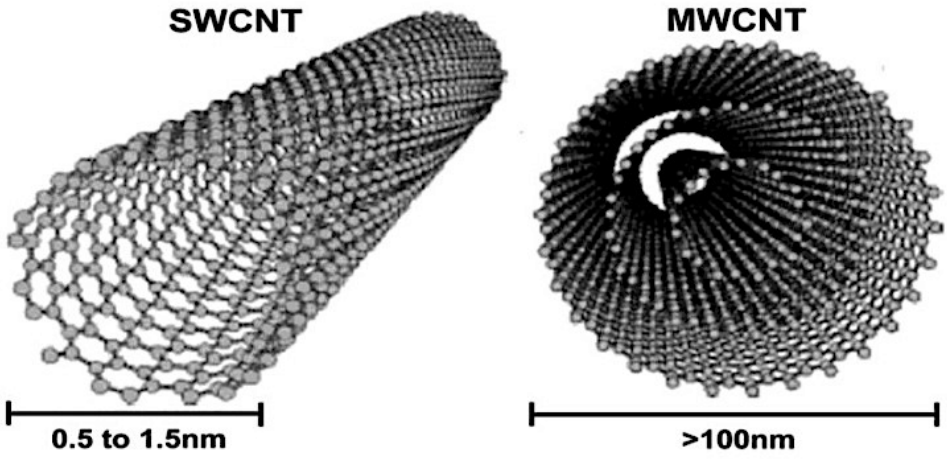

Figure 2.3: Single walled (SWCNT) and multi walled (MWCNT) structure of carbon nanotubes. Retrieved from "Polímeros" [96], under a CC-BY copyright licence.

can travel along the axial direction of the nanotube, being able to more freely traverse the entire structure. Also, both conductivities are higher in carbon nanotubes with higher carbon content, and where the graphitic sheet has less defects.

However, highly pure carbon nanotubes are difficult to fabricate. Carbon nanotubes, as a material, usually exist as a mixture of both high-purity crystalline and low-purity imperfect individual nanotubes. The single rolled graphitic sheet is an idealised scenario often utilised to represent and characterise carbon nanotubes. Figure 2.4 shows several Scanning Electron Microscope (SEM) pictures of a carbon fibre nanotube, and highlights the roughness and imperfections of its surface. Defects and impurities affect not only thermal and electrical conductivity, but also have an impact the structural properties.

Carbon nanotubes have an estimated tensile modulus of approximately $1\mathrm{TPa}$ and strengths between 10 and 52GPa, with failure occurring first on the outer layers of carbon nanotube aggregates, while the inside tubes resisting failure. The tensile modulus of aluminium, for example is in the range of only MPa which is several orders of magnitude lower. Despite these properties, individual nanotubes still tend to slip between each other without breaking, when forced, posing a serious problem to their use.

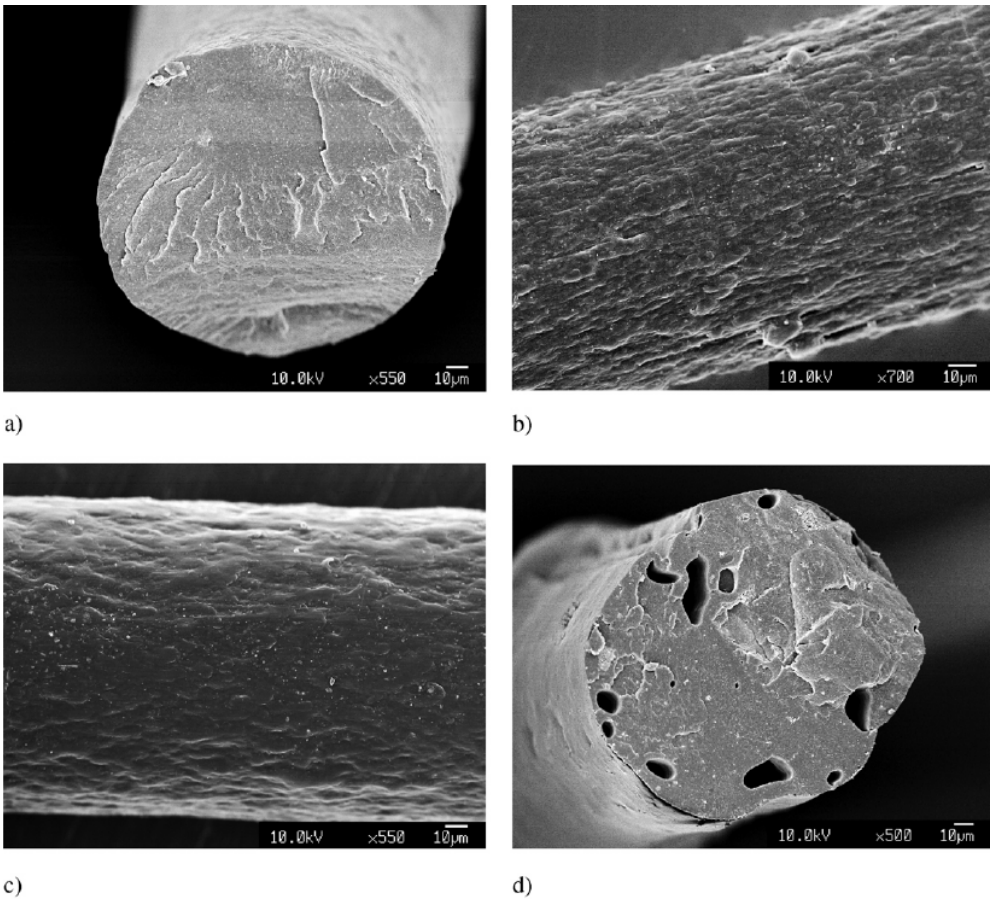

Figure 2.4: SEM images of nanocomposite fibres. Retrieved from ”Polymer” [101] with permission from Elsevier.

2.2.1 Precursor materials of carbon fibres

The type of carbon fibres is closely associated with its precursor material [27, 44]. Polyacrylonitrile (PAN) is a synthetic organic plastic that is incapable of being melted, under normal circumstances, since its degradation point is lower than its melting point. Historically, it is also the first material recognized as a precursor to carbon fibres [27], and it can be oxidized by a thermal process, followed by carbonisation at very high temperatures, above 1000 ^{o}C, and under non-reactive atmospheric conditions to produce carbon fibres. PAN-based carbon fibres are generally classed as type I or type II fibres.

Another carbon fibres precursor material is pitch [27, 44]: a designation for high

viscosity tarry substances. Pitch exists both as a bi-product of natural resources, such as oil and coal, and as a product of synthesis using polyaromatic polymers as starting compounds. The process of turning pitch into carbon fibres is highly complex and several different routes can be followed. Pitch is naturally an isotropic material, however it can be turned into its anisotropic form via heat treatment. Isotropic pitch can be used to produce type III fibres while anisotropic pitch serves as the core material for higher quality type I fibres.

The last common precursor for typical carbon fibres is cellulose [27, 44]. The nature of cellulose as a precursor material prevents the created carbon fibres from being high quality. This is due to the nature of the cellulose matrix, which is fairly discontinuous and contains little to no degree of molecular orientation, meaning that the resulting carbon fibres will lack any crystalline orientation.

Carbon nanotubes differ from typical carbon fibres also in their precursor material. The most common method for carbon nanotube manufacture is chemical vapour deposition (CVD), which consists on precipitating carbon from sources such as methane or asphalt to its solid form.

2.3 Polymer matrix

Polymer matrices utilised in carbon fibre composite manufacturing can differ based on their ability to be remelted: thermoplastics and thermosets [53]. The main difference between both these types of materials resides in the fact that thermoplastics can be remelted while thermosets cannot, and degrade if heated above a certain threshold [51].

2.3.1 Thermoplastics

By definition, a thermoplastic is a polymer substance that becomes pliable when heated to a certain temperature, and solidifies when cooled. Thermoplastics are made of polymer molecules, with a high average molecular weight, that are entangled, in a topological sense, with each other without any chemical bonding between them.

The lack of chemical bonding between polymer chains allows these materials to become more pliable with an increase in temperature, because bonding between chains is week compared with thermal energies at high temperatures [106]. The polymer molecules themselves can be grown via different polymerisation reaction mechanisms, including step- and chain-growth mechanisms [43]. Polymers formed via chain-growth polymerisation grow by having their terminal ends react with compatible monomers, while polymers formed by step-growth polymerisation grow via pairs of compatible reactive monomers bonding, slowly forming longer polymer molecules.

This quality of thermoplastics to be re-heated without degradation of molecular structure allows for their fabrication via techniques such as injection molding or extrusion. These techniques are based on ”forcing” the liquefied thermoplastic material into the desired shape by inserting it into a mold, prior to cooling it down to its final shape. This also allows these materials to be easily recyclable since thermoplastic parts can be heated up, purified, and recast into new shapes [99].

Thermoplastics can have an amorphous or crystalline structure, and that structure is dependent on temperature. The same thermoplastic material can have distinct properties depending on temperature, provided it remains above its glass transition temperature and bellow its melting point. A thermoplastic with an amorphous structure will also be more prone to chemical degradation and cracking since it lacks the crystalline structure [99].

These properties confer thermoplastics the ability to be highly impact and deformation resistant, in addition to also being highly pliable and strong. Also, depending on the ratio of their crystalline and amorphous structures, thermoplastics can also be very resistant to chemical attacks. The versatility of thermoplastics enables them to be used from low-end applications, such as grocery plastic bags, to higher-end applications, such as automobile parts. However, their application is limited to situations where temperature remains stable, and within know boundaries, since they are easily deformed by temperature shifts, and their properties change.

2.3.2 Thermosets

Unlike thermoplastics, polymer chains in thermoset materials form covalent bonds between them, creating a rigid 3D network. This reaction is irreversible and the created bonds cannot be broken, meaning that thermoset materials cannot be recast [51].

Typically, thermoset materials are made of at least two different components: a resin and a hardener. The hardener molecules, often also called crosslinkers, have the potential for forming chemical bonds with the resin molecules, allowing for the growth a 3D network. The initial material is often a soft solid or a viscous liquid, containing a mixture of these two components which hardens when cured [51]. Curing is the process by which the covalent bonds between resin and hardener are formed. The curing process can be induced by adequate supply of heat, radiation, pressure or by the presence of a suitable catalyst. The term curing is interchangeable with the term crosslinking, which is vital to understand this work, and is explored further, and with more detail, in chapter 3.

The polymerisation mechanism for thermoset materials is step-growth, since both resin and hardener exist as monomers prior to the curing process, and they start bonding with each other slowly forming longer polymer chains.

Since the covalent bonds are permanent, these materials have greater resistance to temperature increase than thermoplastics, however this also means that they cannot be recast into different shapes after being cured, and also cannot be recycled. However, they have typically have greater omni-directional strength than thermoplastics, given the nature of the 3D network, but are also more brittle and less resistant to impact.

2.4 Polymers on graphitic surfaces

The properties of the composite materials are dependent on how well the carbon fibre filler particles are dispersed in the polymer matrix and on the overall adhesion between them and the polymer matrix.

2.4.1 Properties of carbon fibre composites

Early studies utilising carbon nanotubes in reinforced Polyvinyl acetate-based composites showed a doubling of Young's modulus when compared with the base polymer, for weight concentrations of carbon filler particles equal or above 60%. Better results were seen above the polymer glass transition temperature, which were consistent with the lack of dispersion of the fibres within the polymer matrix, resulting from melt intercalation [104].

Similar results were also observed for polysterene-based composites for very low weight percentages, 1%, of dispersed carbon nanotubes [95]. In addition, propagation of cracks, viewed by Transmission Electron Microscope (TEM), showed some nanotubes sliding out of the polymer matrix. This indicates that adhesion between the carbon nanotubes and the polymer matrix is not constant and varies for each individual nanotube [95, 100].

Hardness, a measure of resistance to deformation, has also been shown to increase in reinforced composite materials when compared with the bare polymer. Polyethylene-based reinforced composites have shown not only to increase their Young's and strength modulus but have also been shown to increase their hardness by three times the value of the base polymer. The resulting composite has a toughness, defined as the ability that a material has to absorb energy and deform without fractures occurring, in the same range as kevlar, which is five times stronger than steel. [98].

While properties such as Young's modulus, strength modulus, and hardness tend to improve in composite materials, when compared with their base polymer, they are still system dependent. Different combinations of carbon fibre types and polymer materials yield composites with various degrees of these properties [27, 68, 91, 112, 118], as shown in diagram presented in Figure 2.5.

A review published in 2019 by Li *et al.* [68] showcases several different combinations of carbon fibre and polymer materials. They consider carbon black (CB), carbon nanotubes (CNT) and graphene reinforced polymers and distinguish between thermoplastic and thermoset polymers, and give specific insight into epoxy resins which are

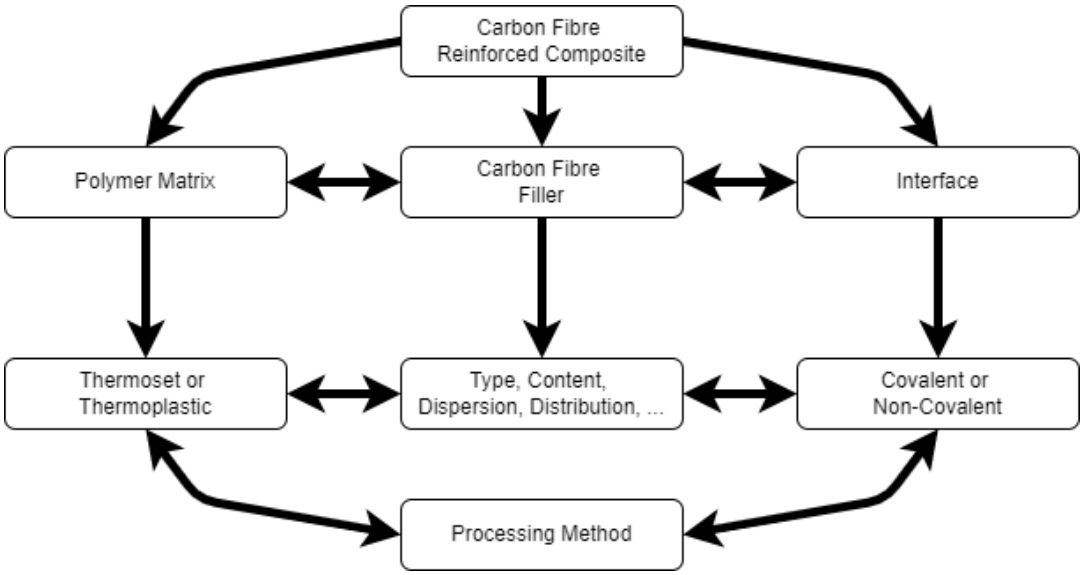

Figure 2.5: Diagram showing all the considerations necessary when processing carbon fibre reinforced composites. Adapted from [68].

the most abundant thermoset polymers utilised in the world.

They conclude that CB-reinforced composites achieve only moderate increases mechanical properties, lower than 100% when compared with the base polymer, due to high percolation. however, CNT-reinforced composites have vastly superior mechanical properties than their base polymers, by outperforming them on 950%, because of the lower percolation rates. However filler aggregation is still present and remains an issue. Grapehene fails to produce any significant results when compared with CNT, because of the inherent difficulty in separating the graphene sheets from graphite [68].

A previous review published in 2009 by Spitalsky *et al.* [112] has also highlighted the difference that manufacture methods present in the mechanical properties of carbon fibre reinforced composites, which is also shown in Figure 2.5. In particular, the layering of woven carbon fibre fabric with polymer matrix layers produces materials with high carbon fibre molecular weight and with Young's and strength modulus values of $11\mathrm{G\,Pa}$ and $325\mathrm{M\,Pa}$ respectively [129], which are one order of magnitude above the bare polymer. but, more relevantly, they also showed that forming covalent bonds between the carbon fibres and the polymer matrix enhanced these properties

further [112].

Processing methods that rely on *in-situ* polymerisation were also shown to have even better mechanical properties, due to the fact that dispersion of carbon nanotubes in the polymer matrix occurs to a greater extent. However, covalently bonding the carbon fibres to the polymer matrix produced the same enhancement effect [112]. The impact of the processing methods on the mechanical properties of carbon fibre reinforced composites has been further validated in recent years [13, 68, 118, 137].

The superb mechanical properties of carbon fibre reinforced materials are not their only desireable feature. It was briefly discussed in section 2.2 that carbon fibres also have some desirable electrical and thermal properties. Polymer materials, by nature, are not good electrical conductors and certain types, such as thermoplastics, cannot withstand very high temperatures. However, by embedding polymers with carbon fibres, these properties are shown to be improved.

2.4.2 Manufacture

Most composites are processed by preparing a mixture of carbon fibre or carbon nanotubes and polymer in adequate solvent and then by evaporating the solvent so that only a composite film remains. This process facilitates the deaggregation of the carbon nanotubes, ensuring adequate mixing within the polymer matrix [27, 92]. The nature of the polymer material also confines the choice of method. Common examples of manufacture methods include *in-situ* polymerisation and melt intercalation [112].

The method involving *in-situ* polymerisation relies on dispersing and mixing carbon fibres in a mixture of monomers, and curing the material when fully mixed [112]. In this way, dispersion and mixing is almost absolute, and polymer growth occurs with the fibres in place. The polymer matrix forms and hardens around the dispersed carbon fibres (or carbon nanotubes), and the resulting structure allows for an easy way for stress to be transferred between the carbon fibres and the polymer matrix. However, this method is restricted to polymers which can polymerise with the carbon fibres dispersed, being mostly thermosets. Such materials need to be cast to their final shape during manufacture, since thermoset polymers cannot be melted and recast [99].

Melt intercalation, contrary to *in-situ* polymerisation, is mostly restricted to thermoplastics, which unlike thermosets, can be melted at high temperatures and reshaped [51]. It consists of melting the polymer and mixing in the carbon fibres, at high temperatures. The increased temperatures facilitate the dispersion and mixing of the carbon fibres, while nor permanently affecting the molecular structure of the polymer molecules. The main drawback of this method is that dispersion is limited, given the large average molecular size of the polymer matrix, and it can result in poorer adhesion between the carbon fibres and the polymer matrix. However, it allows for the manufacture of composite parts which can be easily reshaped or recycled [112].

2.4.3 Improving surface adhesion

The lack of affinity between the carbon fibre surfaces and the polymer matrices can lead to critical failure via debonding of the polymer matrix from the carbon fibre surfaces [45, 90]. Previously in this section the relevance that the manufacture process imparts on the adhesion between both components was also discussed in relation with the debonding process. Improving surface adhesion has become a highly relevant topic of research in recent years, in the search for better carbon fibre reinforced composites [15, 54, 55, 57, 73, 87, 120]. .

Debonding between carbon nanotubes and polymer matrix occurs when the interface, the region of space populated by polymer molecules immediately adjacent to the surface, between both fails under shear stress. The properties of the matrix at the interface also affect the properties of the composite materials, with verified instances of materials withstanding greater shear stresses than expected [18]. This phenomena is known to be polymer-specific, despite this much debate surrounding the nature of the polymer structure at the interface still exists [18, 27]. This phenomena is depicted in Figure 2.6, showing how it can lead to critical failure [15, 54, 55, 57, 73, 87, 120].

It has also be stated in section 2.2 that the surface of carbon fibres (or carbon nanotubes) is rough, uneven, and often contains defects or impurities. These traits are know to affect surface-matrix adhesion, and recent research has been focused in the direction of mitigating this effect.

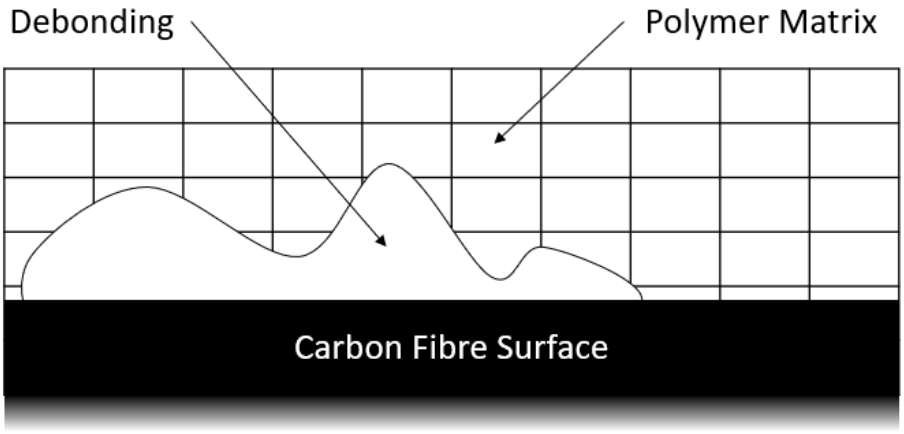

Figure 2.6: Schematic representation of debonding between carbon fibre surface and polymer matrix due to lack of adhesion.

Surface functionalisation of carbon nanotubes consists on grafting molecules to the bare carbon fibre surfaces with desirable functional groups in order to change the chemistry of the surface, promoting better adhesion with the polymer matrix, as shown in Figure 2.7. It has proven to be an effective mean of improving the interfacial bonding between the carbon surface and the polymer matrix. Nanotubes tend to aggregate, limiting their exposed area to the polymer matrix, however by grafting functional groups, such as carboxilic acids, to their surface, this effect is mitigated [27].

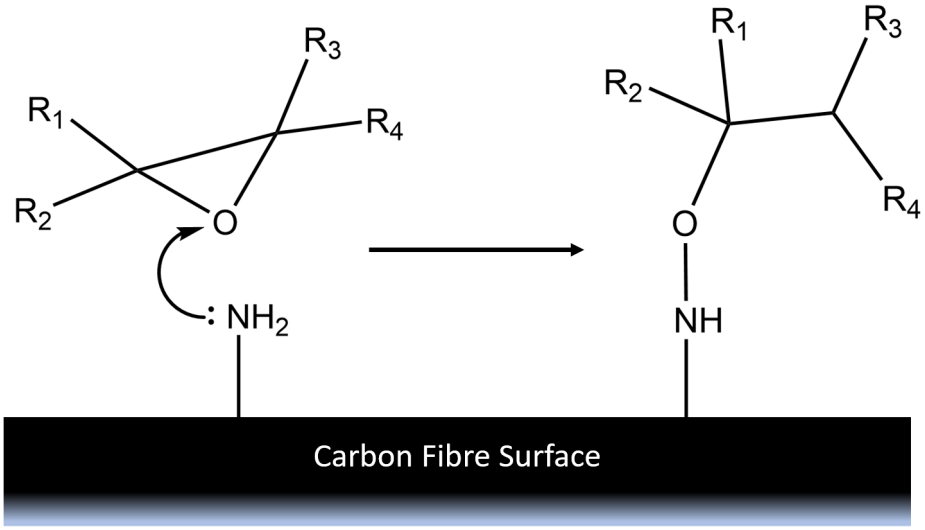

Figure 2.7: Schematic representation of an amine molecule grafted to a carbon fibre surface and forming a covalent bond with an epoxy monomer.

Nanotube dispersion in the polymer matrix has been shown to directly correlate with the strength of the surface-matrix adhesion, and by grafting select functional groups to the surface of the carbon fibres (or nanotubes), their ability to disperse in the polymer matrix is increased. In addition, the physical bonds between fibre and polymer facilitate stress transfer in the interface region from one phase to the other [27].

Surface grafted molecules are bonded to the carbon surface and can bond with polymers in the matrix upon curing [112]. The process of forming covalent bonds between carbon fibres and polymer matrix can be adjusted to accommodate polymers that require different processing methods. Thermoplastic polymers can be mixed with the carbon nanotubes, which can then bond with the surface grafted molecules; Thermoset polymers can undergo *in-situ* polymerisation and bond with the surface grafted molecules during the process. Both processing techniques come with the advantages and disadvantages already discussed.

Hendersen *et al.*proposed, in 2019, a methodology for increasing the hydrophobicity of the surface of carbon fibres without compromising on mehcanial properties. At the same time, this process was shown to increase adhesion between surface and polymer matrix between 59% and 216% [12]. The process mainly involved the functionalisation of unsized carbon fibres with several amine and fluerene-based functional groups, and surface chemistry was verified using TEM imagining. Improvements on the interfacial shear strength were also reflected by increases in tensile strength and Young's modulus of the composite when compared with the bare carbon fibres [12].

In the same year, Sharma *et al.*experimented with adding amine-functionalised carbon nanotubes in conjunction with bare carbon nanotubes to epoxy mixtures. They utilised an equal ratio of both nanotube types in various weight percentages relative to total material weight. Araldite LY-556 epoxy resin was used in all their experiments, and a weight percentage of 0.5% was determined to be optimal for increasing tensile strength by 52.8%, and a weight percentage of 1% for increasing flexural strength by 52.45%. The use of functionalised fibres showed to outperform bare fibres [107].

While surface grafting provides a way to improving adhesion, it is still limited by the quality of the carbon fibre and by the defects present in its surface. Fibres sizing, on the

other hand, consists on dipping the carbon fibres on compounds with high tendency to simultaneously adhere to in and to the chosen polymer matrix. Molecules of selected compounds will fill the ”holes” and imperfections on the carbon fibre surfaces making it smoother. In addition, this changes the chemistry of the carbon fibre surface to be more receptive to adhere with the polymer matrix [72].

Surface grafting has since been a stable method to improve the adhesion between different phases of carbon fibre reinforced composites, however the quality of the adhesion is still dependent on the quality of the carbon fibres used and their surface roughness. Sizing the surface of carbon fibres offers a method for minimising the roughness of the carbon fibre surfaces by ”covering” its defects.

2.4.4 Epoxy-based carbon fibre reinforced composites

It was briefly mentioned in subsection 2.4.1 that epoxy-based composite materials are amongst the most commonly utilised carbon fibre reinforced composites in the world. This is partly because of the versatility of epoxy resins and applicability in a wide range of uses, in addition to their relatively low cost and processing requirements [46]. Epoxy resins are bi-molecular mixtures, which are made of epoxy and a hardener molecules. Epoxy molecules are characterised by having an epoxy (or epoxide) group, as shown in Figure 2.8, which is characterised by an oxygen atom bonded with two separate carbon atoms in a triangular structure. The triangular structure imposes high strain on the molecule and is easily broken via nucleophilic from suitable hardener molecules, such as amines.

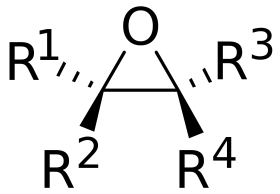

Figure 2.8: Molecular structure of an epoxide group.

When the conditions are adequate for curing, the hardener molecules bond with the epoxy molecules, via nucleophilic attack, to grow a polymer network. The only

requirement for this reaction is the choice a suitable epoxy/hardener pair, and the high variety of possible combinations is what makes epoxy reins such versatile materials.

The nature of this reaction also makes them prime candidates for the manufacture of composite materials via *in-situ* polymerisation [112]. Fracture toughness, which is the ability the ability of the material to inhibit further growth of existing cracks, of unreinforced epoxy resins can be increased up to a factor of 1.31 by reinforcing it with carbon fibres [13]. Also, smaller carbon fibres are shown to yield better improvements in toughness than larger fibres [128].

The modification of the carbon fibre surface can be achieved by reductive electrochemical deposition to graft molecules with functional groups such as amines, carboxilic acids and amides. An epoxy-based polymer matrix, made of EPON-862 and DETDA, with bare carbon fibres was used as a control. Functionalised surfaces displayed increased tensile strength and Young's modulus when compared with the unfunctionalised composite. Out of the three tested functional groups, amines were shown to produce the greatest increase in interfacial shear strength, followed by amides and carboxylic acids [103]. Surface chemistry can be tailored to the required specifications of the composite materials.

In addition, and similar to most other reinforced carbon fibre composites, more evenly dispersed carbon fibres (or nanotubes) yield materials with better mechanical properties and higher impact and fracture resistance. In addition, small weight percentages of carbon fibre fillers, of around 1%, are sufficient to greatly improve the properties of epoxy composites [68, 128].

Dispersion of carbon nanotubes in an epoxy matrix has also been shown to specifically result in an improvement to stiffness as well as an increase of the maximum supported load. Despite this, this improvement peaked when the percentage of carbon nanotubes was at 2% in weight. While these results are material specific, they point towards the existence of an upper limit on the percentage of carbon nanotubes required to improve the mechanical properties of epoxy-based carbon fibre reinforced composite materials [118].

While an extensive amount of research has been done on the properties of al-

ready cured composites, not much emphasis has been given to the liquid structure of pre-polymer mixtures before crosslinking, particularly for thermosets such as epoxy-based systems which are so widespread. The hypothesis for this work is based on the assumption that the liquid structure of a pre-polymerised thermoset presents itself differently depending on the proximity to a graphitic surface. This heterogenous liquid arrangement can cause the structure of the crosslinked network to inherit the structure of the liquid mixture, thus affecting the properties of the composite material, by limiting crosslinking. In addition, given the small scale that the interface region represents in a composite material, simulations provide a useful tool that is capable of giving insight into molecular behaviour in that region.

Over the years, several researchers have investigated the adhesion between the surface of carbon fibres and polymer matrices with recourse to computational simulation methods [17, 31, 32, 47, 49, 58, 64, 66, 122, 135, 136] Simulations provide a way to investigate the very small interface region between the carbon fibre surfaces and the polymer matrices, which are inaccessible to most experimental methods. Simulation methods are covered in more detail in chapter 3.

It was already discussed in section 2.2 that graphene serves only as an idealised representation for the surface of carbon fibres. And while experimental studies are capable of measuring improvements on mechanical properties of composite materials, these are macroscopic and the underlying molecular interactions remain mostly obscure.

Having a way to determine these interactions, even with recourse to approximations, provides a unique tool to further characterise these materials in order to advance them. And, while some recent efforts have been made in the direction of simulating, in practical ways, more accurate carbon fibre surfaces [127], the default still remains the use of graphite as an approximate representation.

In this work this gap in knowledge will be studied, by means of Molecular Dynamic (MD) techniques, which are described in detail in the following chapter 3. Two different systems will be studied: the first of which consists of a fully atomistic representation of the EPON-862/DDS model system; and the second of using a generic polymer

model as a basis for the development of my own crosslinking model for simulating the formation of crosslinked networks of generic polymers.

3. Methodology

This chapter presents a brief overview of Molecular Dynamics (MD), highlighting its concept, origin and applications. This is followed by a description of the MD algorithms, which involve solving Newton's equations of motion for any given system.

Different types of systems, based on macroscopic quantities (temperature, pressure, energy and volume) are also discussed and their differences highlighted alongside their usefulness for different applications. Different types of thermostating and barostating methods are also discussed, which are used to maintain the aforementioned macroscopic variables within a defined range during the simulations.

Force fields are discussed in detail, addressing the different types of non-bonded and bonded interactions, including force fields with application on soft matter systems. The distinction between full atomistic forces fields from generic force fields is also made, including their definitions for non-bonding and bonding interactions.

Periodic boundary conditions and system equilibration are also discussed, as techniques for overcoming finite size effects.

Lastly, an introduction is made to the topic on reactivity in MD simulations, which is further developed in chapter 5 of this work.

3.1 Overview of molecular dynamics

Classical Molecular Dynamics (MD) gives us an efficient and cost-effective method to study the properties of molecular and other non-bonded systems, such as suspensions. It is of particular use to help characterise and describe systems, which are otherwise, difficult to explore by experimental methods, such as protein structures and interphase regions.

MD is a method for simulating the movement and interaction of atomic and molecular species. Atoms and molecules move and interact during a predetermined time period, providing insight into system behaviour and its equilibration. This last concept of equilibration is closely linked with that of potential energy landscape, which is de-

scription of all possible molecular conformations and arrangements in terms of their potential energy. Equilibration, hence, refers to the process of minimising the potential energy of given molecular structures in their respective energy landscapes. Results from an MD simulation are presented as trajectories, which consist on position coordinates, for all particles in a system, over a series of timesteps.

The high complexity of atomic and molecular systems makes it so that numerical methods are more often used, as opposed to analytical methods, to determine how a system progresses over time, for a system starting from an initial configuration. In particular, Newton's equation of motion [80], shown in equations 3.1 and 3.2, can be numerically solved for all particles in a system, where their respective energies and forces, with respect to each other, are calculated with basis on their defined atomic potentials.

$$\overrightarrow{F}(\overrightarrow{r_i}) = -\nabla U(\overrightarrow{r_i}) \tag{3.1}$$

$$\overrightarrow{F}(\overrightarrow{r_i}) = m_i a_i = m_i \frac{d^2(\overrightarrow{r_i}(t))}{dt} \tag{3.2}$$

In equation 3.1 the force $\overrightarrow{F}(\overrightarrow{r_i})$ of a random particle i is described as a function the potential energy U and movement r_i of the same random particle. However, the force of that same particle, according to Newton as per equation 3.2, can also be given by the mass, m_i, times the acceleration, a_i, of that same given random particle i. In addition, t represents the current timestep for the simulation. This makes it possible to establish a relationship between the movement, and coordinates, of a particle and its mass and acceleration. Regarding choice of timestep, this is often done with the aim of it being small enough to capture all of the smallest behaviours of the system, which often relate to the vibrations of covalent bonds involving hydrogen atoms, but also big enough as to not heavily constraint computational requirements.

An MD simulation progresses in an iterative way, as shown in Figure 3.1. An initial starting configuration is setup by establishing coordinates for every particle in the

system and a set of force field parameters to guide their interactions, this constitutes the initial conditions. All the forces based on the initial geometry of the system are calculated and each individual particle moves according to those forces advancing the simulation by a single timestep. New forces from the updated geometric are calculated and particles move again. This is done until the maximum time limit imposed has been reached.

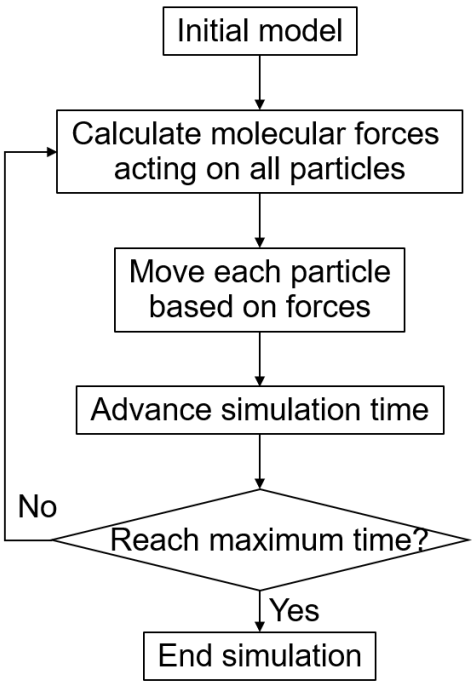

Figure 3.1: Typical algorithm for an MD simulation.

MD can be used to provide insight into the microscopic properties of a system by studying individual atomic and molecular movements, however it is also of note that most MD systems move towards some form of equilibrium. When at an equilibrium state, it is also possible to extract information concerning its thermodynamic properties, at a macroscopic level, by time-averaging quantities such as temperature, volume and density.

3.2 Solving Newton's equations of motion

MD simulations make several approximations in order to increase performance. One highly relevant approximation that MD simulations make is the use of the Born-Oppenheimer approximation. This assumes that the movements of nuclei and electrons in the same molecule are independent from each other [24]. This simplification allows for an MD simulation to consider only the positions of nuclei and disregard the electron contribution towards the calculus of potential energy. Excluding electron movement greatly simplifies the system, making MD simulations less time consuming and more feasible. The lack of electron contributions is mitigated by the use of quasi-empiric parameters to describe the several relevant atomic and molecular interactions. Other common and noteworthy approximations done in MD simulations are that all collisions are perfectly elastic and that atomic charges remain unchanged [29, 125].

Particle positions at each timestep are calculated by means of an integrator, which solves Newton's equations of motion for each timestep during an MD simulations. This requires, however, that initial velocities be specified for the system. This is often done by generating a set of random velocities based a distribution such as a Gaussian or uniform distribution, with a target temperature in mind [94].

Some common integrators, for context, are Runge-Kutta (with Euler's method) [14, 34], leapfrog integration [22] and the velocity-Verlet algorithm [83, 117]. These differ in accuracy and performance and the choice of integrator is done based on these two factors: an increase in accuracy leads to slower simulations while the opposite also holds true.

Out of these integrators, simulations performed in this work utilised the Velocity-Verlet algorithm. The standard Verlet algorithm assumes that two third-order Taylor expansions are made from equation 3.2 [83, 117]. Considering the generic function, $y(t)$, presented previously in equation **??**, its Taylor expansion yields equation 3.3 [124].

$$y(t+h) = y(t) + hy'(t) + \frac{1}{2}h^2y''(t) + \frac{1}{6}h^3y'''(t) + O(h^4) \tag{3.3}$$

And by replacing h for $-h$ and subtracting the resulting expression from equation 3.3 one obtains an approximate expression for the first derivative in equation 3.4:

$$y'(t) = \frac{y(t+h) - y(t-h)}{2h} + O(h^2) \tag{3.4}$$

And the second derivative in equation 3.5:

$$y'(t) = \frac{y(t+h) - 2y(t) + y(t-h)}{h^2} + O(h^2) \tag{3.5}$$

The same process can be done on equation 3.2 to yield equation 3.6, which the Verlet difference equation:

$$r_i(t+h) = -r_i(t-h) + 2r_i(t) + \frac{h^2}{m_i}F_i(t) + O(h^4) \tag{3.6}$$

Which is time-reversible, like the original Newton's equations for motion. This means that by reversing the time on a system that has evolved according to this equation, it can retake its earlier forms exactly.

The velocity of particles, under the Verlet algorithm, can then be calculated by using the difference between values at two timesteps, as per equation 3.7:

$$v_i(t) = \frac{r_i(t+h) - r_i(t-h)}{2h} \tag{3.7}$$

However, at the start of any simulation, two separate sets of velocities are non-existent, so initial velocities, based on temperature and pressure values, can be guessed in order for the algorithm to initialise [83, 117].

The major drawback of the Verlet algorithm is in associated error which is of fourth-order compared with the first-order error from the Runge-Kutta algorithm. However, the standard Verlet algorithm can be further developed in order to minimize this difference.

This is done by dividing the step size, h, on equation 3.7, meaning that velocities are calcualted every half-timestep and subsequently used to calculate particle positions at every timestep. This method is known as the velocity-Verlet method and improves upon the original Verlet algorithm by reducing the error order from four to two, while keeping the same computational efficiency.

3.3 Molecular ensembles

The size, time length, and time scales of a simulation are limited due to available computing resources, however they also need to be large and long enough to provide meaningful insight to real systems. In MD, a molecular ensemble is a tool to constrain and limit a simulation to account for the available computational power as well as to match it to experimental conditions. Initial system configurations need to have adequate number of particles (N) contained, since a large amount can increase the computational requirements. Volume (V), temperature (T), pressure (P) and energy can be kept constant or within a controlled range to simulate different types of experimental setups at different conditions.

Typically, molecular simulations are performed with no change to the number of particles (N) and at either fixed volume (V), pressure (P) or energy (E). By keeping the number of particles, volume and energy constant, a microcanonical ensemble (NVE) is achieved and translates into a simulation that models an adiabatic process in an a isolated system where kinetic and potential energy is interchangeable within the system but no outside transfer occurs [74, 88].

In a canonical ensemble (NVT), simulations occur at constant molarity, volume and temperature. These conditions assume that the simulation box is surrounded by a heat bath, taking the form of a thermostat, and energy exchanges occur between the system and its surroundings. Once in equilibrium the thermostat keeps compensating for energy exchange with system surroundings [25]. For exothermic and endothermic processes the thermostat is also responsible for compensating for the energy that is either released or absorbed by the simulation box.

Simulations with a constant number of particles, and at constant pressure and temperature are referred to as an isothermal–isobaric ensemble (NPT). In addition to a thermostat to control the temperature, a barostat is also required to control system pressure [28]. These conditions more closely mimic an experimental setup since in a laboratory compounds are subject to ambient or controlled temperatures as a well as atmospheric pressure. Since, volume is allowed to shift, system density is also variable unlike under NVT conditions. This makes these conditions more suitable to capture more intricate processes such as phase transitions.

3.4 Thermostats

Temperature and pressure of particles in MD simulations are controlled by a thermostat and a barostat respectively [119]. The kinetic energy of a system is related with its pressure which in turn is affect by particle velocity that is dependent on temperature. It is the function of the thermostat to equilibrate temperature to its user-specified values, during the simulation runtime. Common thermostats are the Berendsen [21], Nosé–Hoover [52, 84, 85] or Langevin [37, 48, 102] thermostats.

The Berendsen thermostat assumes the shape of a heat bath that envelopes and is loosely coupled to the simulation box. It then performs a re-scale of particle velocity to negate fluctuations in the kinetic energy of the system that would lead to a temperature increase. The major issue with this thermostat is that it deviates from the canonical ensemble due to the suppression of the kinetic energy caused by re-scaling velocities. The flying ice cube problem is also quite common when using this thermostat and consists on the entire simulation box having an unidirectional velocity. Since this thermostat relies on velocity rescaling to equilibrate temperature this effect is not detected by it.

The Nosé–Hoover thermostat is based on the same principle as the Berendsen thermostat, however the heat bath now becomes part of the system. This thermostat takes the form of a single imaginary particle that is coupled with the system. This particle is given a mass and a velocity, such as any other particle in the system, how-

ever the values of those can be tweaked to increase or decrease how strongly the imaginary particle is coupled wit the system. Energy exchanges between the system and the imaginary particle take place, and are controlled by how strongly both entities are coupled. The system can ”leak” energy to the imaginary particle which results in a lowering of the temperature and reductio of kinetic energy. Similarly, the opposite can also be done by allowing the imaginary particle to supply the system with energy, increasing its temperature and kinetic energy.

The idea behind Langevin dynamics and its thermostating is that it assumes that the atoms are being simulated inside a sea of comparatively much smaller imaginary particles that simultaneously cause friction with the atoms and will occasionally collide with them. The Langevin thermostat changes the equations of motion at every time step to accommodate these two factors: first it adds a dampening factor to the momentum of each atom to mimic the friction with the imaginary particle sea and a Gaussian random number generator is responsible for simulating the occasional collisions between the sea of particle and the much larger atoms giving them more momentum. The combination of these two factors yields a canonical ensemble.

Simulation design

Simulations in this work use the velocity-Verlet algorithm for solving Newton’s equations of motion. This choice is based on the notion that its associated error is similar to that of the leapfrog algorithm, and is only within one order of magnitude from the Runge-Kutta algorithm. It is also the more efficient of the three algorithms, and it also allows for time-reversibility, unlike Runge-Kutta, which keeps it on par with Newton’s equations of motion.

In this work, both the NVT and NPT ensembles are used but for different purposes. The NVT ensemble is used to mix and equilibrate the system because the fixed volume of a (generally) larger box allows for particles to move more freely and decorrelate from their initial positions and structures. The NPT ensemble is used in our production simulations since it mimics more closely experimental conditions of the processes we are studying. This ensemble allows for density to equilibrate based on specific temperature and pressure ranges much like one would find in a laboratory.

For temperature control, the Nosé–Hoover thermostat was utilized given its faster implementation versus Langevin dynamics. In addition, it is capable of maintaining a canonical ensemble, unlike the Berendsen thermostat, yielding more reliable predictions for macroscopic thermodynamic properties.

It is highly unlikely that initial configurations for any system are already at equilibrium with particles having close overlap with each other. Typically, particle de-overlap is done under NVT conditions where particles have ample space to move around in an attempt to minimize energy. Once de-overlap takes place, system can be changed to NPT where it will compress or expand based on temperature and pressure conditions.

Initially, a rapid change in density will occur which will gradually slow down as the systems reaches its equilibrium density. Density, can thus, be used as a measure for system equilibration, as it remains stable after the system reaches its equilibrium. Other quantities can also be used to determine system equilibration by means of auto-correlation functions. Seeing how fast the end-to-end distance decorrelates from initial values also gives an estimate for system equilibration.

Similarly, energy will also tend to decrease as the system evolves towards equilibrium, with lowest average energy values occurring after system equilibration. This equilibration process is important, because only after it takes place can system statistics that are representative of reality be measured.

3.5 Periodic boundary conditions

Periodic boundary conditions constitute a set of conditions that allow for the creation of an approximately infinitely large system, by replicating a small subset of the system itself, in the form of a unit cell [29, 119, 125]. When a specific particle crosses a defined periodic boundary of the unit cell it is contained in, it reappears on the opposite side from where it crossed as depicted in Figure 3.2 for a 2-dimensional space. Typically, in MD simulations this principle is applied to a 3-dimensional space and particles are able to move, exiting and re-entering the simulation box. Without periodic boundary conditions in place, and given a large enough simulation box, particles at its centre

will behave differently from particles at the edge of the simulation box since the latter are affected by the box boundary, bouncing back on collision and causing artefacts in the simulation. By applying periodic boundary conditions, particle behaviour remains consistent despite the position of the particle inside the simulation box.

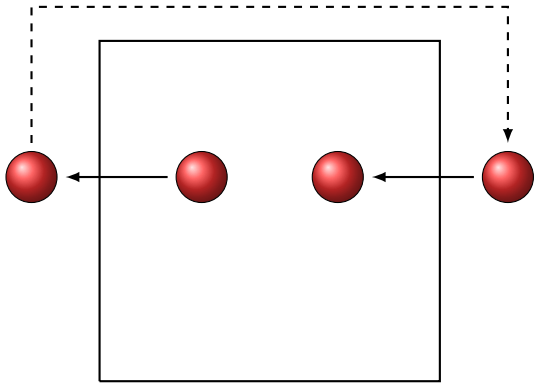

Figure 3.2: 2-dimensional representation of periodic boundary conditions.

3.6 Force fields

The potential energy of a particle is described by bond, angle and dihedral potentials as well as van der waals and Coulomb interactions. As per equation 3.1 all these terms are summed to yield the corresponding force of a given particle at a specific timestep during simulation. Hence, these terms need to be pre-specified for Newton's equations to be solved. the collection of pre-determined parameters, involving bonded and non-bonded interactions, and functional forms that guide molecular behaviour is known as the force field [29, 119, 125].

3.6.1 Bonded interactions

Bonded interactions describe the bond stretching, angle and torsion potentials. Bonds are usually modelled as springs that obey the harmonic potential (equation 3.8) [75]:

$$U_{harmonic} = K_{ij}\ (r_{ij} - r_{0,ij})^2 \tag{3.8}$$

where K_{ij} is the bond strength and $r_{0,ij}$ is the equilibrium distance for atoms *i* and *j*

and r_{ij} the actual distance between *i* and *j*.

Similarly to bonds, the angle between three atoms is defined most often by an harmonic expression (equation 3.9) [75]:

$$U_{harmonic} = K_{ijk}\ (\Theta_{ijk} - \Theta_{0,ijk})^2 \tag{3.9}$$

where K_{ijk} and $\Theta_{0,ijk}$ are the angle strength and the angle respectively and Θ_{ijk} is the angle between atoms *i*, *j* and *k*.

The dihedrals are interactions between four atoms. There are many expressions used and one of the most common expressions is the ”harmonic” (equation 3.10) [75]:

$$U_{harmonic} = K_{ijkl}\ [1 + d\ cos(n\Phi_{ijkl})] \tag{3.10}$$

that takes into account only the strength of any particular torsion, as K_{ijkl}, because the parameter *d* can only be either positive or negative one in order to switch the sign of the cosine. Φ_{ijkl} is the dihedral between atoms *i*, *j*, *k* and *l*.

3.6.2 Non-bonded interactions

Non-bonded interactions relate to all interactions between atoms that are not bonded to each other and can be divided into two types of forces: electrostatics and van der Waals [29, 119, 125].

The electrostatic interactions are calculated via Coulomb’s law, depicted here in equation 3.11, that takes into account the charge, q, of any given pair of atoms, i and j, and the distance, *r*, between them [29].

$$U_{coulomb} = \frac{q_i q_j}{4\pi\epsilon_0 r} \tag{3.11}$$

Where the values for the atomic charges are calculated from quantum calculations.

The Lennard-Jones potential (LJ; equation 5.1) is the oldest and most commonly used potential for describing van der waals interactions is shown in Figure 3.3 [82].

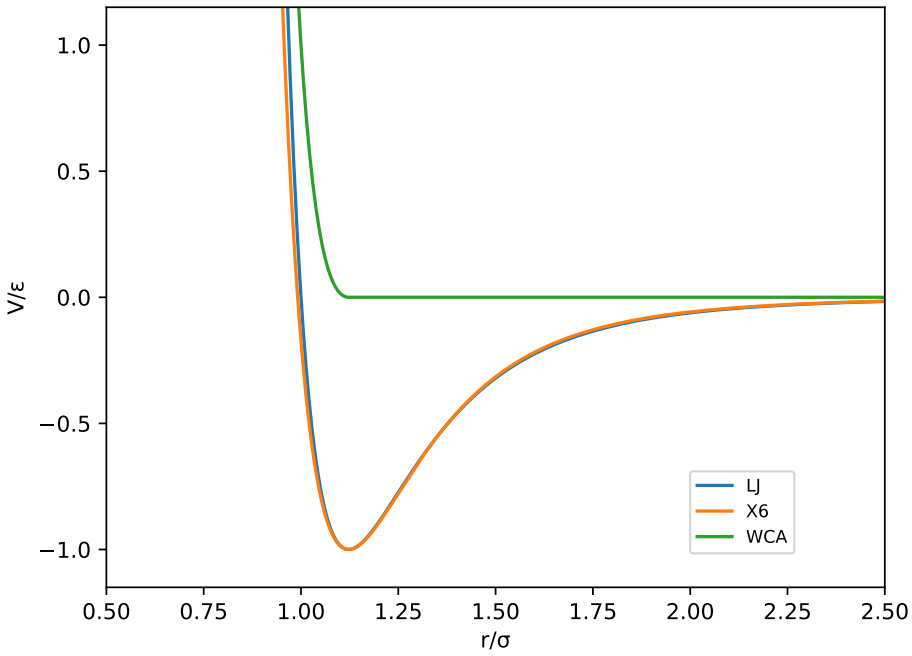

Figure 3.3: Different non-bonded van der waals potentials for $\epsilon = \sigma = 1$ with arbitrary units of distance and energy.

$$U_{LJ} = 4\epsilon\left[\left(\frac{\sigma}{r}\right)^{12} - \left(\frac{\sigma}{r}\right)^{6}\right] \tag{3.12}$$

where σ represents the distance at which the potential is zero and ϵ its equilibrium energy.

The Buckingham potential, also known as the exponential-6 (X6) potential, contains four parameters (A, B, C and α) instead of just the two parameters utilized in the Lennard-Jones potential. These parameters can be related to σ and ϵ LJ values to produce a curve that resembles the original Lennard-Jones near equilibrium [69, 70].

$$\begin{aligned} E_{\mathrm{X6}} &= \epsilon\left[\frac{6}{6-\alpha}\exp\alpha\left(1-\frac{r}{r_0}\right) - \frac{\alpha}{\alpha-6}\left(\frac{r_0}{r}\right)^{6}\right] \\ &= A\exp\left(-Br\right) - \frac{C}{r^6} \end{aligned} \tag{3.13}$$

Although it resembles the LJ potential near the equilibrium region when the param-

eters are derived from σ and ϵ, as one can see by the comparing the blue and yellow lines in Figure 3.3, the high energy repulsive region of the X6 potential is located at a shorter distance than the LJ, meaning that atoms can potentially get closer to each other.

3.6.3 Standard force fields for soft matter systems

It has been discussed that a force field is composed by a set of parameters that range from bonding to non-bonding and that these are used to describe how molecular systems evolve over time. These parameters are obtained from either experimental setups or *ab initio* calculations.

There are several common force fields whose parameters have been derived and are widely used and accepted throughout the scientific community. Such examples are the DREIDING [75], OPLS [59] and COMPASS [115] force fields.

OPLS, was initially parameterised from Monte Carlo simulations of pure organic liquids and other aqueous solutions being designed to be used in liquid systems hence its designation of "Optimized Potentials for Liquid Simulations" [59, 60]. Over time it has grown considerably and been expanded upon becoming a more general purpose force field akin to DREIDING [75].

The OPLS force field employs a different dihedral potential form for describing the torsions [59, 60] (equation 3.14)

$$\begin{aligned} U_{OPLS} =& \frac{1}{2} K_{1,ijkl} \left[1 + cos(\Phi_{ijkl})\right] \\ &+ \frac{1}{2} K_{2,ijkl} \left[1 - cos(2\Phi_{ijkl})\right] \\ &+ \frac{1}{2} K_{3,ijkl} \left[1 + cos(3\Phi_{ijkl})\right] \end{aligned} \tag{3.14}$$

that consists on a sum of three "harmonic" terms, the first and last of which have positive *d* and the second one negative *d*. Other than that, the values for the energy constants define which of the three terms is more relevant in order to describe any particular interaction with the possibility of any of them being zero and negating their

term entirely.

When choosing a force field one needs to take into account the type of systems it was designed to work with. Not only that, but some force fields are proprietary, such as COMPASS which was designed to model condensed phases and only to be used with Material Studio [115]. For this reason COMPASS was not utilised in this work. Force fields such as DREIDING [75] are general purpose and can, in theory, be utilised with any given system, however in the case of DREIDING, it lack parameterisation for partial atomic charges, meaning that these need to be calculated prior by methods such as quantum mechanics. Because of this, wit was used, in this work, only for the purposes of validation, where partial atomic charges were available from the literature. While OPLS started as a force field specifically designed for use in liquid organic systems, it has since evolved over time to provide an entire suite of parameters, meaning that its utilisation is much more straightforward than DREIDING.

3.7 Reactivity in MD simulations

The last section in this chapter briefly addresses reactivity in MD simulations, which is a topic further explored in chapter 5. A chemical reaction is a process in which electrons causing the forming or breakage of chemical bonds between atoms or molecules. The Morse potential in an asymmetric potential, utilised in quantum mechanics, to describe bond behaviour between particles, and can be described by equation 3.15:

$$\mathrm{V'(r) = D - e(1 - e^{-a(r-r_e)})^2} \tag{3.15}$$

(3.16)

where r is the distance between atoms, $\mathrm{r_e}$ is the equilibrium distance and $\mathrm{D_e}$ is the well depth that determines how strong the bond is. As both atoms close in on each other, there is a high repulsion barrier that pushes them apart and if they are pulled apart the bond eventually breaks when dissociation energy is reached. However, an energy barrier needs to be surmounted in order for this to happen.

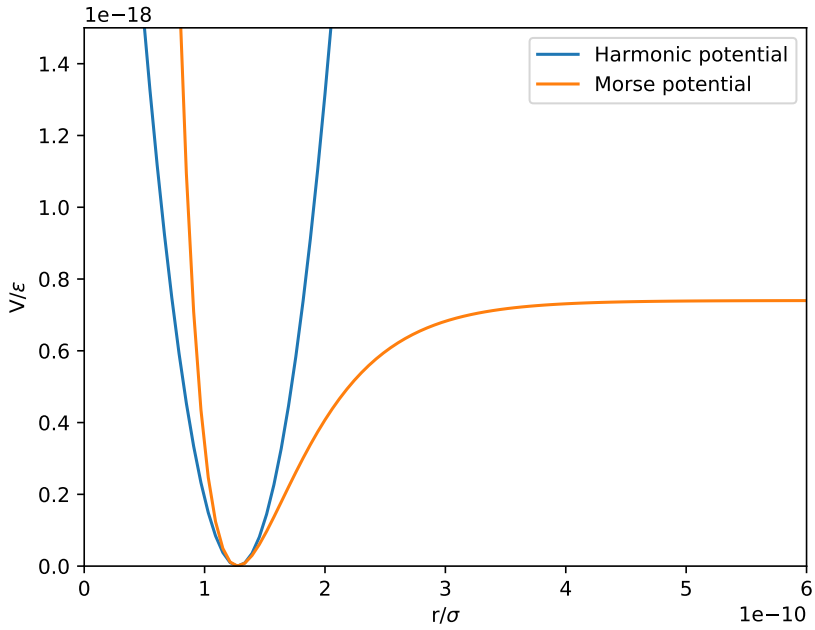

Figure 3.4: Comparison between harmonic and Morse potentials.

It was stated before, in this work, that, in traditional MD, bonds are modelled as springs using an harmonic potential. The comparison between the harmonic and Morse potentials is presented in Figure 3.4, and shows that the dissociation energy barrier present in the Morse potential is absent from the harmonic potential. This implies that new bonds cannot be created, nor existing ones broken in traditional MD simulations. This aspect of MD poses a challenge when simulating systems such as crosslinked polymers, or polymer adsorption, since they are processes that require new bonds to be created.

Reactivity in MD has been addressed in one of two ways: by creating hybrid methods (QM/MM) that combine both MD and quantum mechanic (QM) techniques; and by designing specific force fields or force field parameters which are capable of modelling chemical reactions [33, 41, 61, 71, 79, 89, 121, 123, 134]. The latter of these two approaches is further separated into two sub-classes of methods: empiric methods; and proximity methods. Empiric methods involve designing and creating force field parameters that are capable of reproducing chemical bonding, while proximity methods

involve artificially creating bonds between two close particles.

Both these approaches are less computationally demanding than hybrid methods, and proximity methods have the added benefits of not requiring specifically developed force fields, and can be used with standard existing force fields.

4. Effect of a carbon fibre surface on epoxy resin mixtures

This chapter investigates how carbon fibres affect the liquid structure of an epoxy mixture. Two different systems were studied, both made of the two different combination of the three molecules presented in Figure 4.1.

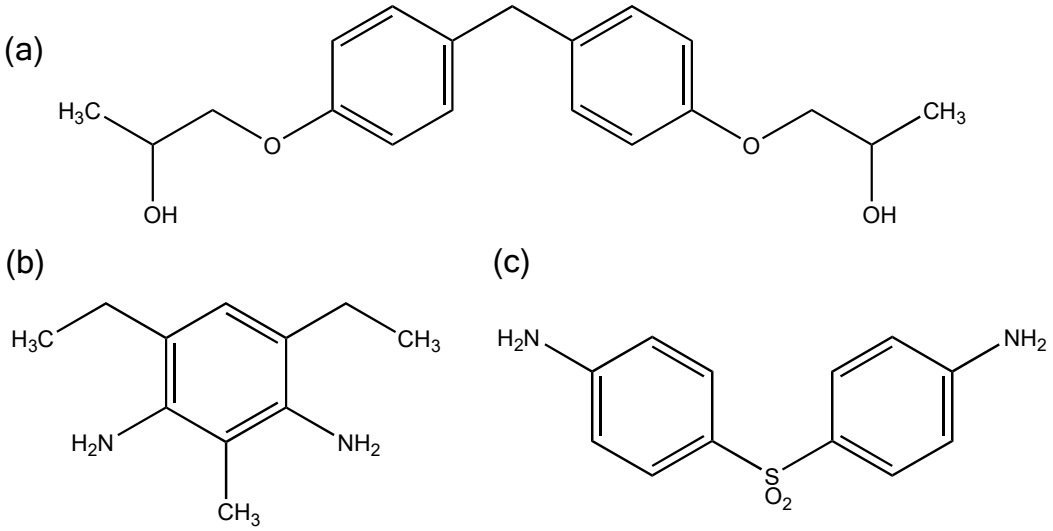

Figure 4.1: Molecular structures of (a) Activated EPON-862 (b) DETDA (c) DDS

In this chapter I will first validate a force field for use with the EPON-862/DDS (Diglycidyl Ether of Bisphenol F/4,4'-Diaminodiphenylsulfone) liquid mixture by also using the EPON-862/DETDA (Diglycidyl Ether of Bisphenol F/Diethyltoluenediamine) as a means of validation, and then proceed to use it to study liquid structure of this system in bulk and in the presence of a carbon fibre surface, to determine how the surface affects liquid structure at the interface region, and how it propagates to the rest of the system.

First, some important background information about fibre-reinforced composites and the utilisation of epoxy-model systems for their research is provided. This is followed by my own work, describing and testing six force field variants and providing

relevant simulation details. Next, bulk systems are investigated to establish a baseline, and then finally a carbon fibre surface is added, and its effect on liquid structure is studied.

4.1 Introduction

Fibre-reinforced composites are used in a wide variety of industries, including renewables, aerospace and automotive, that take advantage of their light weight, high strength, and durability. Carbon fibre composites are often made of a thermoset polymer matrix, such as epoxy, combined with carbon fibres. The mechanical strength of the composite crucially depends on the adhesion between the polymer matrix and the fibre [105]. The epoxy network is formed by mixing epoxy resin with a curing agent, called a hardener, and heating the mixture at high temperature to initiate crosslinking between the resin and hardener. To make fibre-reinforced composites, fibres are dispersed in the resin-hardener precursor liquid mixture prior to curing. The structure of the precursor liquid near the fibre is likely to be different than the bulk liquid mixture, and these structural changes may affect the subsequent polymer network, and thus the overall composite properties. However, the structure of the polymer matrix near the fibre interface is not well understood and is difficult to characterise experimentally. Classical molecular dynamics (MD) simulations can provide insight into the liquid and polymer structure and dynamics near the interface.

While there have been many simulations studying the properties of polymeric systems at solid surfaces [17, 58, 135, 136], only a few studies have considered the structure of the precursor liquid mixtures and subsequent network formation near interfaces. A study by Farah *et al.* [40] used a reactive MD method with a coarse grained (CG) model of a binary liquid mixture to study network formation in the presence of a surface [40]. When the two monomers had different surface interactions they observed an enrichment of one monomer at the surface, which led to an interphase region with compositional differences up to 4 nm from the surface. A similar interphase width of 5 nm was found by increasing the number of bonds per linker molecule from two to

four [39]. While this CG model provides physical insight into the curing process, it cannot predict the specific chemical behaviour of an epoxy-hardener system, which has complex monomers with different shapes, sizes, and surface interactions. For this, atomistic models are required.

Several authors have utilised atomistic MD simulations have been used to investigate crosslinking in epoxy-based systems, mainly focusing on EPON-862 with DETDA and DGEBA hardeners [31, 32, 47, 49, 64, 66, 122]. Crosslinking methodologies were developed for bulk EPON-862/DETDA systems and properties of the crosslinked systems, such as density, thermal expansion coefficients, glass transition temperature, and elastic constants, were found to be in good agreement trends set by experiments [64, 66, 122]. Figure 4.1a and 4.1b depicts the structure of activated EPON-862 (terminal epoxy groups are open into alcohol and alkyl groups) and DETDA respectively.

Varshney *et al.* [122] have managed to create a crosslinked polymer network based on the EPON-862 and DETDA molecules using the consistent valence force field (CVFF). They considered their reactive sites as the epoxy rings on the EPON-862 molecules and the amines on the DETDA molecules, and focused mainly at establishing an adequate crosslinking procedure for this system. They found that their favoured approach to model building produced a good match between predicted and experimental properties, as density, volume shrinkage and the coefficients of thermal expansion agreed with the literature [123].

Li *et al.* [64, 66] in their work proposed a method to simulate the crosslinking of thermoset polymers using the aforementioned EPON-862/DETDA as a model system for epoxy thermosets. Their method took into account the possibility that partial atomic charges can change during reaction, and explored how different processing conditions affect the final structure and thermal properties of the thermoset. Density, glass transition temperature, coefficient of thermal expansion, and elastic constants were all in good agreement with literature. Only the density was slightly lower than experimental, and this was attributed to the fact that the smaller timescales of simulation force faster reaction rates. In addition, they also showed that differentiating between the reaction

of primary and secondary amines showed no impact in the crosslinked network, and did not manage to achieve above 80% conversion. They performed their simulations using the DREIDING force field.

Gavrilov *et al.* [47] developed their own CG model using the EPON-828 (a similar molecule to EPON-862) and DETDA molecules as reference. They proceeded to use dissipative particle dynamics (DPD) to simulate a crosslinking reaction between both intervening molecules. They then reversed-mapped the system back to its original state, by performing a process akin to a reverse coarse-graining, and ran a standard MD simulation in order to study the properties of crosslinked network. With this approach they hoped to speed up the equilibration time of their simulation and focus on the study of the resulting topology. Their focus was mainly in studying how their own parameters for the CG model affect the properties instead of performing an in-depth comparison with the literature.

While so far I have discussed studies where the authors have mainly focused on developing methodologies for the creation of crosslinked networks for model epoxy systems, Hadden *et al.* [49] differs since they focused on studying the effect that a surface has on a crosslinked network. They reported that perturbations of the crosslinked density were found up to 10 Å from the nearest surface point. Results were in agreement with literature and their own transmission electron microscope (TEM) images. Internal stress in the crosslinked network was also found to be greater at the interface than in the centre of the film. Their simulations were performed using the OPLS force field.

Similarly to Gavrilov, Walsh *et al.* [31, 32] have also focused on studying the thermo-mechanical properties of their crosslinked epoxy network near a functionalised carbon fibre surface. Their own protocol for forming the crosslinked network was developed. It focused mainly on studying physical interaction between the crosslinked network and the functionalised fibre while also performing fibre pull-out tests to extract information about the interfacial shear stress (IFS), which was found to agree with experimentally calculated interfacial shear strength (IFSS) for the same systems. In addition, they have reported that physical bonding between the epoxy or the crosslink-

ers with the functionalised groups in the fibres is not required for a large increase in IFS.

To summarize all these studies, presence of an interface region was shown to be independent of system conversion (i.e. fractional conversion or crosslink density) on simulated EPON-862/DETDA. Conversion was also shown to affect epoxy polymer properties at the interface, such as mass density, residual stress, and molecular potential energy [49] with effects on thermo-mechanical properties [50]. In addition, the appearance of an interface region in crosslinking simulations relates to system size with materials properties (network structure) fluctuating, while thermal properties remain mostly unaffected (specific volume, coefficient of thermal expansion and glass transition temperature) [47].

Correlations between predicted interfacial shear strength of functionalised surfaces and epoxy polymers were found to be in agreement with experiments for an all-atom EPON-862/DETDA system, providing a framework to apply to future materials. These indicate that adhesion between fibre and polymer increases for functionalised fibres, and is dependent on the grafted functional groups [31, 32]. This model has subsequently been applied to study water ingress in epoxy composites [126].

While simulations have been valuable in shaping a better understanding of network formation and how it translates to composite properties, interactions at the interfacial region have been restricted to the relatively small DETDA and DGEBA hardener molecules. Since composite properties are known to depend on the interfacial region, it is important to understand the molecular structure and composition of the interface region. In this study, I investigate the properties of the precursor mixture of EPON-862 with the more complex hardener 4,4-diaminodiphenyl sulfone (DDS), as can be seen in Figure 4.1. Like DETDA, DDS also contains two amine groups capable of forming tertiary amines upon crosslinking, however it is a larger molecule containing two benzene groups connected by a sulfone. I first investigate several force field models by benchmarking properties for the EPON-862/DETDA system, and then selected a force field to investigate the properties of the EPON-862/DDS liquid mixture. Finally, I investigate how a graphite surface perturbs the liquid properties, paving the way for

future studies of how the surface affects network formation in this system.

4.2 Methodology

4.2.1 Force field models

A total of six force field variants were used to perform my simulations on EPON-862: DREIDING/LJ, DREIDING/X6, DREIDING/LJ/Q, DREIDING/X6/Q, OPLS-AA and OPLS-UA. All force fields were tested extensively on EPON-862 before a final candidate was also tested on DETDA and DDS.

The final step of validation consisted on running a single equivalent simulation using the OPLS-UA force field on a pure DETDA system to predict its density in the same way as EPON-862 and DDS. Afterwards, a mixture of EPON-962/DETDA was simulated with OPLS-UA and radial distribution function (RDF) data compared with available literature to get an indirect mean of validating the structure of EPON-862/DDS system, for which no information was available.

I then defend my final choice of force field to use in further simulations with either the EPON-862/DDS or EPON-862/DETDA mixture in addition to a graphene surface.

In section 4.3.1, it is presented a comparison of different force fields for pure EPON-862 and DETDA liquids. The OPLS-UA force field is then selected to study the EPON-862/DDS mixture, and to investigate how a graphite surface influences the liquid mixture properties.

The EPON-862/DETDA system was simulated using several variations of the OPLS [59] and DREIDING [76] force fields. The OPLS-AA force field is a fully atomistic model that treats all atoms explicitly, whereas the OPLS-UA force field treats the alkyl and aryl hydrogen atoms and their bonded carbons as single united atoms. The OPLS-AA and OPLS-UA force fields use the harmonic potential to describe the bond stretch between two atoms, and the angle bend between three atoms. Dihedrals are described using the first three terms of a Fourier expansion. OPLA-AA and OPLS-UA parameters were taken from Jorgensen *et al.* [59]. Non-bonded interactions are described by the Lennard-Jones (LJ) potential, and electrostatics by Coulomb interactions using Ewald

summation. Parameters are reported in the Appendix.

The DREIDING force field describes bonds and angles using harmonic potentials for the bond stretch and angle bend. Dihedrals are described by the first term of a Fourier expansion. Non-bonded van der Waals interactions are described by the LJ potential, and electrostatics, when charges are included, are treated by Coulomb potential using Ewald summation. I have denoted the original DREIDING force field as DREIDING/LJ. DREIDING parameters for EPON-862 and DETDA were taken from Mayo *et al.* [76].

A variation of the DREIDING force field, that replaces the LJ potential with the Buckingham (X6) potential as described in the Appendix. I have denoted this version of the DREIDING force field as DREIDING/X6. Parameters for this potential form are in the Appendix, and were converted from the original Mayo *et al.* parameters [76] as denoted by Lim [70].

DREIDING partial atomic charges for EPON-862 and DETDA were taken from Demir *et al.* [32] as calculated with the Charge Equilibration (QEq) method. I have tested both variations of the DREIDING potential above with charges, and these are denoted DREIDING/LJ/Q and DREIDING/X6/Q. In either case, electrostatic interactions are described with the aforementioned Coulomb potential with a cutoff at 8 Å.

The graphite surface was modelled with five graphene layers. The graphene layers were parametrised using uncharged carbon atoms connected across periodic boundaries in the x and y directions. The thickness of the five layers prevents non-bonded interactions of the liquid from leaking across the surface to periodic images, in the z direction, of the system. Simulation box size averages at 80 Å in the z direction. The chosen force field to model the layers was GraFF [108]. The functional forms for bonded interactions under GraFF are the same as in OPLS-AA and OPLS-UA, and non-bonded var der Waals interactions are described by the LJ potential. Force field parameters for the graphite surface were taken from Sinclair *et al.* [108] with arithmetic mixing rules applied for OPLS compatibility, and are reported in the Appendix. Carbon atoms in the central layer were kept fixed.

4.2.2 System setup

All MD simulations were performed using the LAMMPS software [94]. Periodic boundary conditions were applied in the x, y and z directions for all simulations.

Bulk

To obtain an initial structure for the molecules, individual molecules were simulated in vacuum for 100 picoseconds to minimise their energy. Structures resulting from these simulations were kept for comparison with bulk simulations. These molecular structures were used to set up the three types of systems studied: namely pure liquids, liquid mixtures and liquid mixtures, between two graphene slabs.

For pure liquid simulations a monomer was replicated 64 times in a cubic simulation cell of dimensions 48$\times$48$\times$48 Å^3 forming a lattice. A similar procedure was used to set up the bulk mixtures. EPON-862 is mixed with a hardener molecule in a 2:1 ratio. A simulation cell containing two EPON-862 and one hardener molecule (DETDA or DDS) was replicated 128 (4$\times$4$\times$8) times inside a cubic box of dimensions 70$\times$70$\times$70 Å^3, to give a system of 256 EPON-862 molecules and 128 DDS or DETDA molecules. The structure was then annealed, increasing temperature from 300 K to 1000 K over 50 ps, then keeping it constant for an additional 40 ps, and finally reducing the temperature from 1000 K to 300 K for another 50 ps.

Initial pre-equilibration densities of EPON-862, DDS and DETDA pure liquids are 0.30 g cm^{-3}, 0.24 g cm^{-3} and 0.17 g cm^{-3} respectively. These volumes provide enough free space in the simulation boxes to allow for molecular displacement to take place ensuring proper mixing. Pre-equilibration densities for for EPON/DDS and EPON/DETDA mixtures were 0.55 g cm^{-3} and 0.50 g cm^{-3}, respectively, also ensuring that proper mixing can take place.

Surface

For the slab simulations, the procedure was similar to that for the bulk mixtures, with the molecules replicated inside a rectangular box of dimensions 49$\times$51$\times$120 Å^3, with

the graphite surface perpendicular to the z-axis as show in Figure 4.2.

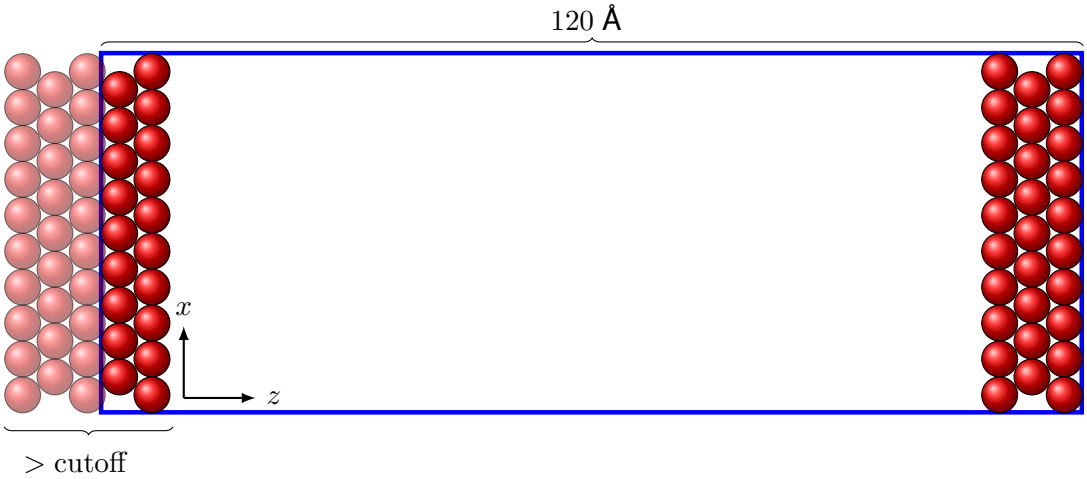

Figure 4.2: ”Empty” simulation box with graphene layers

The surface itself consists of five stacked graphene layers made of a series of repeating hexagons formed by the bonded carbon atoms as, shown in Figure 4.3, with the equilibrium distance between atoms being of 1.42 Å and the angles of 120°. This figure also depicts the initial stage of constructing each graphene layer. The unit cell, represented by the two red carbons was replicated and shifted in all Cartesian directions to form the surface.

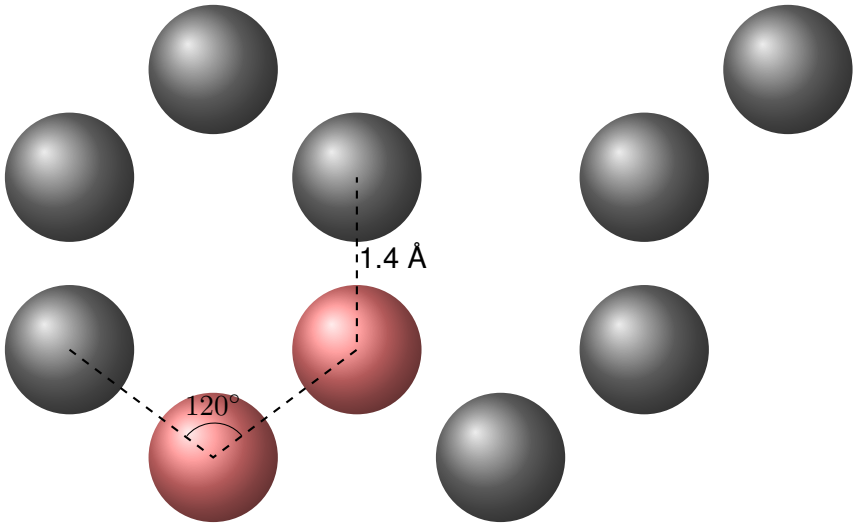

Figure 4.3: Graphene surface unit cell (red) and replication.

Replicating this unit cell yields the structure shown in Figure 4.4. In this figure, the red and blue layers are AB stacked, which is in agreement with the most stable conformation for graphene layers. This is due to the repulsion forces between the carbon atoms of different layers being at their minimum, since half the carbons in each layer align with the centre of the rings in neighbouring layers.

All layers were parallel with the xy plane and covered the entire area of the plane. Increasing surface size in the xy plane generates a larger simulation box, while increasing the number of stacked graphene layers increases surface thickness. The central graphene layer is treated as a rigid body, and unable to be deformed by the interactions of the neighbouring layers. Terminal carbons at the edge of each layers are made to connect the periodic images of the opposing carbon atoms in the same layer creating an infinite surface for my simulations [35, 36]. This method avoids having to fill the edge carbons with hydrogens which would require defining more non-bonding interactions, including hydrogen bonds, and the surfaces would have to be maintained in place by artificial forces. Box size was kept fixed in the x and y dimensions. The same mixing procedure followed for pure liquids and liquid mixtures is also performed between 500 K and 1000 K to aid in force field validation.

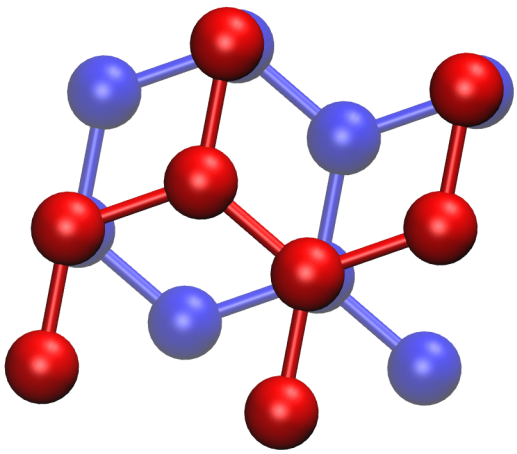

Figure 4.4: Overlap between two graphene sheets showcasing the initial AB stacking between sheets.

4.2.3 Simulation methodology and equilibration

MD simulations were performed using the LAMMPS software [94]. For the bulk simulations, periodic boundary conditions (PBC) were applied in the x, y and z directions. For the slab simulations periodic boundary conditions were also applied in all directions with the surface thickness being greater than the range of both Coulomb and van der Waals interactions.

After mixing under NVT conditions, single molecule simulations ran for an additional 1 ns to get structural parameters. For pure liquids, simulations were done at 300 K. These consisted on 14 ns under NPT conditions using Nose-Hoover thermostat and barostat for temperature and pressure control. An analysis of density found this procedure to be sufficient for equilibration, as it stabilised with time, and retrieval of system statistics, as shown in the Appendix. Mixture simulations followed an identical procedure for temperatures of 500 K.

For slab simulations, the production simulation time was 100 ns, under NPT conditions, to equilibrate and extract statistics. The inner layer of the surface, perpendicular to the z axis at its origin, was fixed in space during the entirety of the simulation. The remainder of the molecules in the system, including the other graphene layers, were prone the thermostat and barostat creating an uneven surface. Pressure control was anisotropic, with the change in size of the simulation cell along each direction being independent from one another. Size variation of the xy plane is minimal and limited by the presence of surface bonds across the PBC, and the size along the z direction shifting to accommodate change in liquid density.

4.3 Results and Discussion

In subsection 4.3.1, I present a comparison of different force fields for pure EPON-862 and DETDA liquids. In addition, I also examine liquid differences of liquid structure achieved by better performing force fields: DREIDING/X6/Q and OPLS-UA. The OPLS-UA force field is selected to study the EPON-862/DDS mixture in subsections 4.3.2, and 4.3.3 I investigate how a graphite surface influences the liquid mixture prop-

erties.

4.3.1 Force field validation

The density of pure EPON-862 simulated at 300 K for all six force fields is presented in Table 4.1, together with experimental densities available from manufacturer specifications [4, 5] and previous simulation results [32, 64, 66, 122], taken at atmospheric pressure, and between 273 and 300 K. This narrow range of temperatures is considered insufficient to significantly affect results. The force fields give a range of densities, under atmospheric pressure at 300 K, and all underestimate the manufacturers' specifications, with DREIDING/X6/Q given the closest agreement, followed by the Consistent Valence Force Field (CVFF), OPLS-UA, DREIDING/X6, OPSL-AA, DREIDING/LJ/Q, and then DREIDING/LJ.

Table 4.1: Average density, ρ, at 300 K (with $\pm$ values the standard deviation), for liquid EPON-862 using different force fields. $\Delta\rho$ is the percent difference in density from the average manufacturers' density of 1.183 g cm^{-3} [4, 5].

Method/force field	ρ (g cm^{-3})	$\Delta\rho$ (%)	Reference
EPIKOTE-862$^{\mathrm{TM}}$	1.180	-0.3	[4]
EPON-862$^{\mathrm{TM}}$	1.186	+0.3	[5]
CVFF	1.120	-5.3	[122]
DREIDING/X6/Q	1.120	-5.3	[64, 66]
DREIDING/X6/Q	1.132$\pm$0.005	-4.3	[32]
DREIDING/X6/Q	1.127$\pm$0.009	-4.7	Present
DREIDING/X6	1.082$\pm$0.010	-8.5	Present
OPLS-UA	1.100$\pm$0.010	-7.0	Present
OPLS-AA	1.061$\pm$0.008	-10.3	Present
DREIDING/LJ/Q	0.986$\pm$0.008	-16.7	Present
DREIDING/LJ	0.947$\pm$0.010	-19.9	Present

The two implementations of DREIDING/X6/Q in the literature give different densities, which result from different partial charges and a different scaling parameter used to translate from LJ to Buckingham non-bonded potentials [70]. Strachan *et al.* used electronegative equalization-based charge assignment (ECA) which benefits from dynamically updating charges over simulation time [67] while Walsh *et al.* kept

their charges fixed [32]. Our present work used DREIDING/X6/Q with the same scaling parameter as Li *et al.* [64, 66] and the partial charges reported in Demir *et al.* [32] (see Appendix), and gives similar densities to these previous simulations. CVFF gives good results for EPON-862, however, it lacks all the parameters necessary for DDS, and thus was not considered here. OPLS-UA and DREIDING/X6 have slightly lower, but comparable, densities to those obtained using DREIDING/X6/Q. OPLS-AA and the DREIDING/LJ force fields underestimate manufacturer values by between 10-20%, and thus have been excluded from further consideration. As OPLS-UA is a widely available force field, and has the most accurate density apart from CVFF and DREIDING/X6/Q, I have further compared the performance of OPLS-UA and DREIDING/X6/Q for DETDA and DDS.

The density of pure DETDA using OPLA-UA is shown in Table 4.2 alongside DREIDING/X6/Q, and experimental values at room temperature [2, 32]. Similarly to EPON-862, OPLS-UA underestimates the experimental value by approximately 8% while DREIDING/X6/Q underestimates it by 4%. It is challenging to compare the densities for DDS, as at room temperature DDS is a powdered solid with densities between 1.270 g cm^{-3} and 1.430 g cm^{-3} [1, 3, 7, 131]. Our simulations using OPLS-UA yielded a liquid DDS density of 1.370$\pm$0.013 g cm^{-3}at 300 K. To further check the OPLS-UA performance, an EPON-862/DETDA mixture was simulated using DREIDING/X6/Q and OPLS-UA. The radial distribution functions for both force fields were in good agreement with previous literature [32] (see Appendix).

Table 4.2: Average density, ρ, at 300 K ($\pm$ values are the standard deviations), for liquid DETDA using different force fields. $\Delta\rho$ is the percent difference in density from the average manufacturers' density 1.022 g cm^{-3}.

Method/force field	ρ (g cm^{-3})	$\Delta\rho$ (%)	Reference
ETHACURE$^{\mathrm{TM}}$ DETDA	1.022	-	[2]
Experimental	1.022	-	[32]
DREIDING/X6/Q	0.982$\pm$0.007	-3.9	[32]
OPLS-UA	0.939$\pm$0.014	-8.1	Present

I have shown that OPLS-UA gives comparable densities to the DREIDING/X6/Q force field for EPON-862 and DETDA. In addition, OPLS-UA is 3-4 times faster than

DREIDING/X6/Q, and 2-3 times faster than DREIDING/X6. I also foresee it to be a more convenient model to simulate crosslinking reactions due to its nature as a coarse-grained model.

To further access the capabilities of OPLS-UA, the liquid structure achieved by using either DREIDING/X6/Q or OPLS-UA on an EPON-862/DETDA system was analysed by means of RDFs, and compared with literature.

Figure 4.5a shows the RDFs, depicted as $g(r)$, calculated with DREIDING/X6/Q. The CE-CE curve shows two peaks, the first at 6 Å and the second at 12 Å which are consistent with parallel alignment of the EPON-862 molecules. The CD-CD curve has one high peak at 8 Å and the CD-CE curve shares a similar shape to the CE-CE curve, but is much smoother. The similarities between results and those of Walsh *et al.* [32] indicate that DREIDING/X6/Q is well parametrised and serves as a good comparison for OPLS-UA.

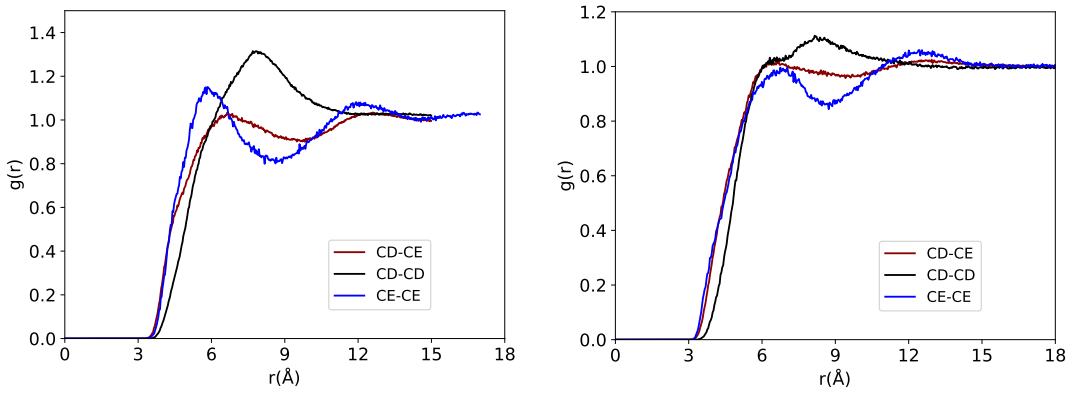

Figure 4.5: a) DREIDING/X6/Q RDFs from the EPON/DETDA mixture at 500 K. b) OPLS-UA RDFs from the EPON/DETDA mixture at 500 K.

The RDFs under OPLS-UA are in figure 4.5b. The positions of the peaks are near-identical to those in figure 4.5a, with the height of the CE-CE peaks being the biggest difference between the two force fields. This result was not unexpected, since EPON-862 is a more rigid molecule when characterised by DREIDING/X6/Q than by OPLS-UA and, highly prone to changes due to force field parameters. However, qualitatively, the structure yielded by OPLS-UA is in good agreement with that of DREIDING/X6/Q,

meaning that both force fields seems to model liquid structures in similar ways. In addition, density obtained with OPLS-UA is of 0.938±0.014 g cm^{-3} when compared to 0.988±0.005 g cm^{-3} obtained by Walsh *et al.* [32] showing the good agreement between both force fields.

With both density and structure of EPON-862/DETDA mixture yielded by OPLS being in agreement with the literature, I find OPSL-UA a suitable force field in the modelling of epoxy-based systems. Therefore, OPLS-UA was chosen for the study of EPON-862 and DDS mixtures.

4.3.2 EPON-862/DDS liquid mixture

In this subsection I present the properties of the liquid mixture of EPON-862 and DDS at a typical curing temperature of 500 K. The mixture contains EPON-862 and DDS molecules in a 2:1 ratio. The density of the liquid mixture is 1.15±0.07 g cm^{-3} at 300 K and 1.01±0.02 g cm^{-3} at 500 K. For ideal liquids I would expect the EPON-862/DDS mixture to have a density of 1.18±0.011 g cm^{-3} and 1.02±0.021 g cm^{-3} at 300 K and 500 K, respectively, which are close to my mixture densities.

RDFs for the pure EPON-862 and DDS liquids and the EPON-862/DDS mixture at 500 K are shown in Figure 4.6. The RDFs were calculated using the central carbon atom in the dimethyl group connecting both aromatic rings in EPON-862, and the sulfur atom of DDS (see molecular structures in Figure 4.1a and 4.1c, respectively).

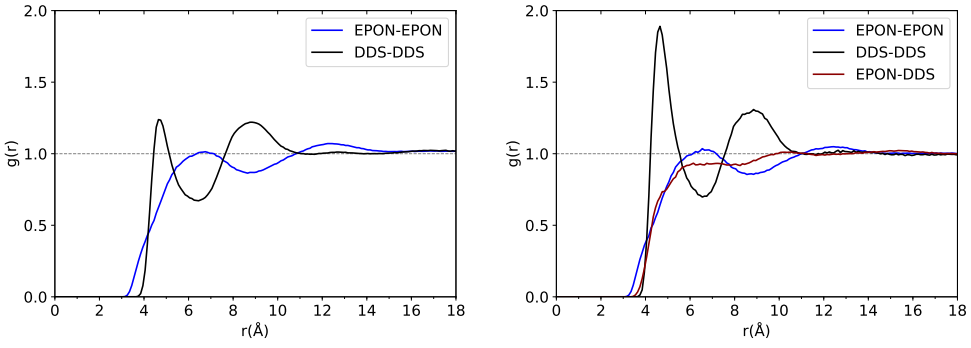

(a) (b)

Figure 4.6: RDFs from (a) the pure EPON-862 and DDS liquids at 500 K, and (b) the EPON/DDS mixture.

In Figure 4.6a, EPON-862 shows a broad peak at 6 Å and a suggestion of a second peak at 12 Å. To understand these peaks I compare EPON-862 with the structure of bisphenol-A-polycarbonate (BPA-PC) which has a similar molecular structure. Although BPA-PC is a polymer melt, rather than a molecular liquid, I expect similarities in the short range order. A molecular dynamics simulation study of BPA-PC using a 4:1 coarse-grained model [8] and experimental observations [132] gave similar RDFs to my observed EPON-862 RDF. In terms of molecular arrangement, these peaks correspond to the EPON-862 molecules being oriented with two neighbouring EPON-862 molecules attempting to form a square, while a second neighbour adopts the same conformation as the first molecule, similar to the structure described for the similar molecule diphenylmethane in its crystal state [19].

The pure liquid RDF for DDS, also shown in Figure 4.6a, shows two distinct peaks at 4.4 Å and 8.4 Å. The shift of the peaks to the left, compared to EPON-862 can be explained by the higher density of DDS. Similarly to EPON-862 and diphenylmethane the DDS molecules tend to orient themselves in a diamond shape. Although DDS also has two phenyl rings similar to EPON-862, the sulfone group joining the two rings makes DDS much more rigid, giving sharper peaks.

In the mixture RDF, shown in Figure 4.6b, both EPON-862 and DDS have similar RDF peak positions as for the pure liquids, although the height of the first DDS peak, at 4.4 Å is greatly increased. The difference in height between the first and second DDS peaks suggests that DDS molecules tend to pair with each other and that these pairs are interspaced with EPON-862 molecules or other DDS molecules. Despite the preference for DDS molecules to pair, the RDFs seem to indicate that the mixture is well mixed. This is further confirmed by the EPON-DDS RDF which is quite structureless.

This was followed by a more detailed analysis that was performed by comparing several RDFs from specific atoms or atom groups of both EPON-862 and DDS when they are pure liquids, versus when they are both in a mixture. These show that molecular structure remains mostly unchanged in mixture with the exception being that EPON's central and end carbons from different molecules tend to be pushed farther apart in the mixture when compared with pure liquid.

These RDFs are based on groups of atoms of interest that were identified for both the EPON-862 and DDS molecules, and consisted of grouping the hydrogen atoms with their bonded carbon atoms. RDFs between these groups were calculated for both molecules as pure liquids and as part of a mixture. Groups of interest for EPON-862 are the dyphenil alkyl group (C), the end aklyl groups (CE) and the ether connected aromatic carbons (CO). For DDS, the two groups on interest are the central sulfur (S) and the amine connected aromatic carbons (CN).

Figure 4.7 shows the RDFs calculated between these groups for both pure liquid and mixture for EPON-862. All pairs of graphs are very similar indicating that the molecular structure of EPON-862 does not change drastically when in a mixture. The sharper peaks for the C-CE, C-CO and CO-CO interactions are due to the intramolecular interactions of the functional groups.

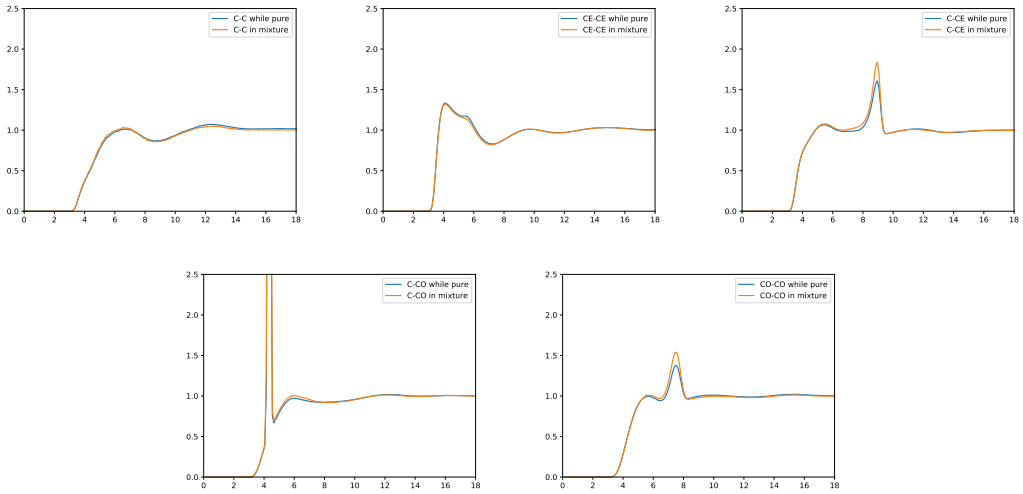

Figure 4.7: Comparison RDFs for pure EPON-862 and EPON-862 in mixture.

DDS shows a similar scenario than that of EPON-862, with the three RDFs shown in Figure 4.8 being very similar between liquid and mixture. However, it is noticeable that DDS in mixture has overall higher peaks at shorter ranges of interaction. This is an indicator that DDS molecules tend to cluster when in mixture.

I now look at the dynamics in the liquid mixture compares to the dynamics in the pure liquids. The mean square displacements (MSDs) for the pure liquids and mixture

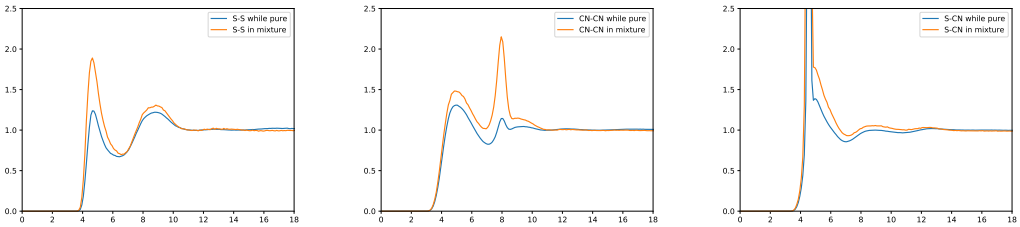

Figure 4.8: Comparison RDFs for pure DDS and DDS in mixture.

are shown in Figure 4.9.

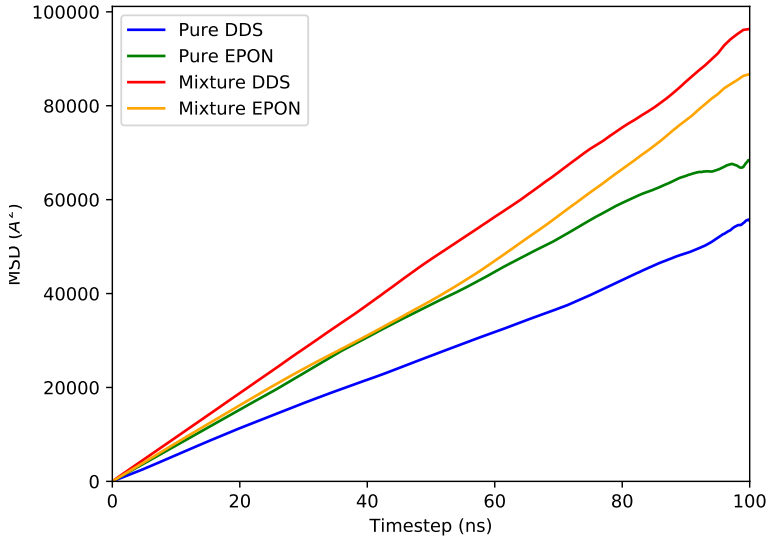

Figure 4.9: MSDs from the EPON/DDS mixture and the pure EPON-862 and DDS liquids at 500 K.

The dynamics of DDS molecules in the pure DDS liquid is slower than the dynamics of EPON-862 molecules in the pure EPON-862 liquid. Diffusion coefficients were calculated, using the first 30 ns, to be 7.64×10^{-9} $m^2\,s^{-1}$ and 5.63×10^{-9} $m^2\,s^{-1}$ for pure EPON-862 and DDS, respectively. This range was chosen so that the calculated diffusion coefficients for all systems had an R^2 of 0.99. In addition, approximate simulation cell size is 57 $Å^3$, so this range ensures that for every system, molecules were allowed to move over at least twice the length of the simulation cell ensuring that MSD data is relative to a liquid and that the system is not locked into any specific struc-

tural arrangement. These values are consistent with the densities of both pure liquids at 500 K, with EPON-862, having the lowest density of the two, displaying a higher diffusion coefficient.

Interestingly, the diffusion of both components in the liquid mixture is faster than in the pure liquids, and the diffusion coefficients increase to 8.15$\times 10^{-9}$ m^2 s^{-1} and 9.37$\times 10^{-9}$ m^2 s^{-1} for EPON and DDS, respectively. Over the selected 0-30 ns range EPON-862 shows similar displacement in pure liquid as it does in mixture. The difference in density between pure EPON-862 and mixture, at 500 K, ranges between 2-10 % making both systems very similar in terms of densities. Considering their densities, similarity between diffusion coefficients of EPON-862 in both systems is to be expected, with variations also being caused by the presence of DDS in mixture.

The diffusion coefficients of DDS show greater disparity between pure liquid and mixture. Unlike for EPON-862, the density of pure DDS is significantly higher than that of the mixture, ranging between 14-24 %. DDS is at a lower density in the mixture, where it displays its higher diffusion coefficient. In particular, the DDS molecules diffuse fastest in the mixture, which could be explained by the lower density of the mixture, and that the DDS molecules are more rigid and smaller than the EPON molecules.

4.3.3 EPON/DDS mixtures at model carbon fibre surface

An EPON-862 and DDS mixture with a 2:1 molar ratio was set up in the presence of a graphene surface and simulated at 500 K using NPT conditions with anisotropic pressure control.

Figure 4.10a shows the monomer density variation for the whole mixture as well as for EPON-862 and DDS molecules. Density was calculated within bins with width of 0.1$\times$box size, using the molecular centres of mass contained in each bin as well as bin volume. As is typical for liquid mixtures, the density at the interface oscillates before becoming bulk-like after around 10-15 Å. 15 Å marks the ”separation” between interface and centre regions of the simulation. The density in the centre region, encompassing the region 15 Å away from each surface, is 1.01$\pm$0.001 g cm^{-3}, which

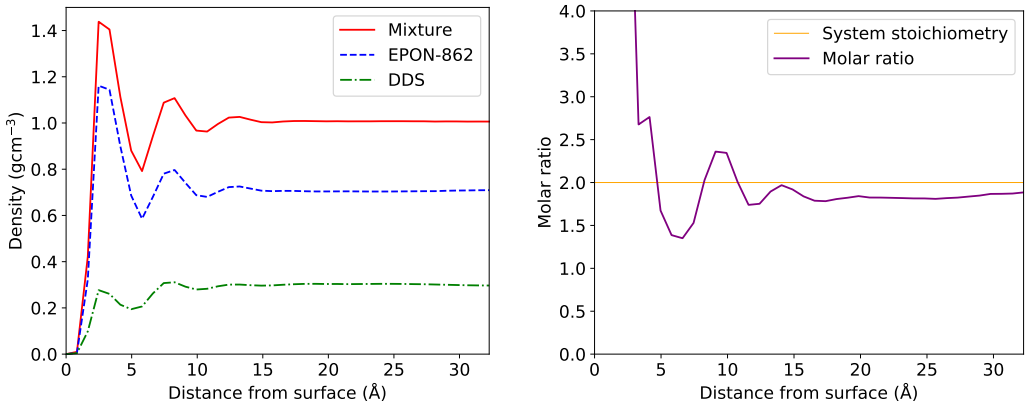

(a) (b)

Figure 4.10: Symmetrised profile of the density (a) and molar ratio (b).

is identical to that of the bulk mixture, of 1.01$\pm$0.002 g cm^{-3} at 500 K. The individual components of the mixture show different behaviour near the surface with EPON-862 having a much higher density than DDS near the surface.

Figure 4.10b shows how the molar ratio of EPON-862 to DDS varies with distance from the surface. As previously mentioned, the average molar ratio in the liquid is 2:1, however, at the interface, there is significant variation corresponding to an excess of EPON-862. The binning procedure, using bins with width of 0.1$\times$box size, makes it that the bin closest to the surface only contains EPON-862, hence the large spike near the interface. Figure 4.10b is cropped to better visualise the difference in molar ratio at the interface. The accumulation of EPON-862 near the surface leads to a change in the stoichiometry that is likely to influence the formation of the network structure during curing. For example, the accumulation of EPON-862 at the interface may lead to unreacted EPON-862 molecules, particularly if crosslinking is diffusion-limited, and therefore a weak interface region. The excess of EPON-862 at the interface also results in a lack of EPON-862 in the centre region of the simulation cell.

The molecular orientation at the interface may also affect crosslinking near the surface, for example, by resulting in directional bonding at the surface, or by limiting the ability of molecules to bond due structural constraints. To investigate this, the bond orientation parameter, P_2, was calculated for ring-to-ring and ring-to-surface orientations.

P_2 is defined as

$$P_2 = \frac{3}{2}\langle \cos^2\theta \rangle - \frac{1}{2} \tag{4.1}$$

where θ is the angle between a normal to the plane of the ring and the normal to the surface, as schematically shown in Figure 4.11. A value of P_2=1 indicates that the

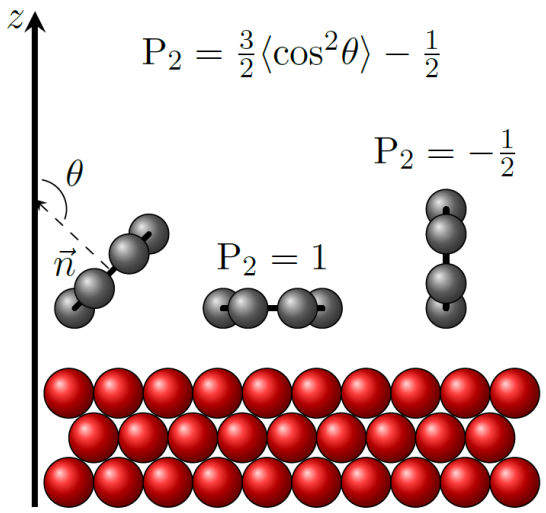

Figure 4.11: Visual representation of P_2 parameter respect to the surface.

rings are parallel to the surface and P_2=-0.5 indicates a perpendicular orientation of a ring with respect to the surface. An ensemble average of $< P_2 >$=0 indicates random orientation of the rings with respect to the surface.

The ensemble averaged P_2 profiles for ring-surface orientation for EPON and DDS are shown in Figure 4.12a. I see that close to the surface (up to 15 Å) P_2 is positive, showing that rings tend to be oriented parallel (with the ring normal perpendicular) to the surface. In the centre region P_2 tends to zero indicating that there is no preferred orientation.

I have also assessed whether this alignment of the rings near the surface affects their molecular conformations by calculating the P2 values between the two rings within a molecule. As before, average values of P_2 equal to 1, -0.5 and 0 indicate that the rings are parallel to each other, perpendicular to each other, or randomly orientated, respectively. The orientation of the aromatic rings within molecules as a function of distance from the surface is shown in Figure 4.12b.

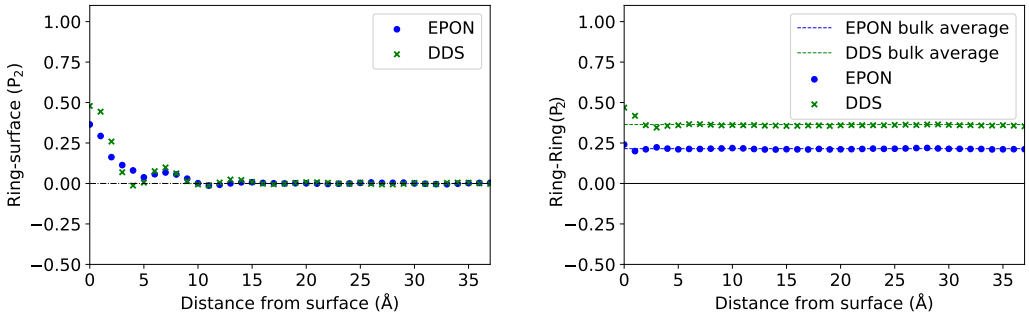

(a) (b)

Figure 4.12: Symmetrised profiles of ring-surface (a) and ring-to-ring orientations (b).

The P_2 values from the bulk mixture simulations are 0.215±0.032 and 0.364±0.042 for EPON-862 and DDS, respectively. In the centre region, 15 Å away from either surface, EPON-862 has a P_2 value of 0.216±0.002 whereas DDS has a P_2 value of 0.360±0.003. Both these values are similar to their bulk counterparts indicating that molecular conformation is not affected by the surface outside the interface region. The effect of the surface is short range, and further increases the P_2 of DDS, indicating a slight 'opening' of the molecule, whereas the effect on EPON-862 is very small.

As previously mentioned, diffusion plays a role in the crosslinking process, and the interfacial region is often observed to have slower diffusion in polymeric systems [77] So far, it is noticeable that the surfaces disrupts molecular behaviour at the interface region with molecules at the centre region behaving similarly to bulk mixture. One should note that the centre region has an approximate size of 60×50×33 Å^3, being smaller than the simulation cell of the bulk simulation with 57×57×57 Å^3. I isolated this region and measured the individual molecular displacement when molecules entered this region at any point during simulation and stopped measuring it as soon they left. If a specific molecule re-entered the centre region, its displacement was measured again, starting from that moment. This process generated multiple small trajectories and a few larger ones given that most molecules in the system entered and exited the centre region multiple times. All trajectories were averaged, with initial values being heavily averaged compared to later values, given the higher amount of smaller trajectories, to produce one singular mean displacement graph for both EPON-862 and

DDS. This is present in Figure 4.13 alongside the single-origin scaled bulk MSD curves for reference for the first 10 ns of simulation. It is visible that after approximately 4 ns, the MSD curves from the centre region (and interface region) start showing increased levels of noise.

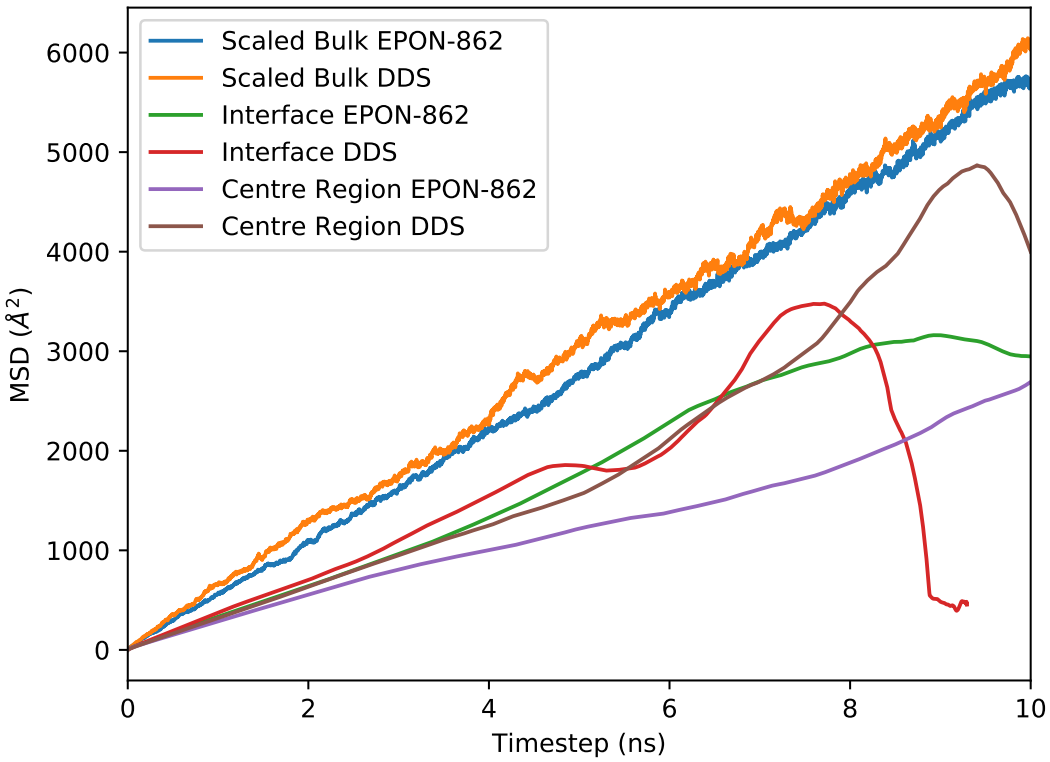

Figure 4.13: 2D averaged mean squared displacement for EPON-862 and DDS at the centre region of the surface simulation.

The nature of this averaging process makes it that the initial stages of the MSD are more representative of the system than the later ones. For the purposes of this analysis I considered only data collected until 4 ns averaged over multiple trajectories. By design, diffusion in surface simulations is essentially 2D, hence the MSDs are calculated as the summation of $\langle \mathrm{x}^2 \rangle + \langle \mathrm{y}^2 \rangle$ for molecules in both the interface and centre regions.

At the interface, 2D diffusion coefficients are 3.21×10^{-9} $\mathrm{m}^2\,\mathrm{s}^{-1}$ for EPON-862 and 3.75×10^{-9} $\mathrm{m}^2\,\mathrm{s}^{-1}$ for DDS considering diffusion only in the xy plane. In the same way, at the centre region 2D diffusion coefficients for EPON-862 and DDS are of

2.54$\times$10^{-9} m^2 s^{-1}, and 3.13$\times$10^{-9} m^2 s^{-1} respectively. These results are not intuitive since I would expect diffusion at the interface to be slower than in the centre region. Figure 4.13 also shows the scaled bulk MSD and I would expect the diffusion on the centre region to be similar. Diffusion coefficients were also calculated for the entire surface system without distinction between interface and centre regions: EPON-862 has a diffusion coefficient of 2.98$\times$10^{-9} m^2 s^{-1} and DDS of 3.43$\times$10^{-9} m^2 s^{-1}. The fact that little to no difference between diffusion in the interface and centre regions is seen, coupled with the fact that diffusion is slower in the centre region of surface system than in the bulk, point towards the necessity of a larger simulation cell with greater spacing between layers to adequately study diffusive effects.

4.4 Conclusions

The interactions between fibre and polymer at the interface region of composite material are key in understanding its properties. MD simulations can provide insight into how a surface affects the structure of precursor monomers. However, studies have been using the same force field as an investigation standard on epoxy based model systems. In this work, I have tested several force field variants of DREIDING, and OPLS and found the later being more convenient and versatile, while yielding satisfactory results for EPON-862/DETDA system.

Our results on the well-established EPON-862/DETDA model system show that OPLS-UA has only marginally worse predictive accuracy than the standard charged version of DREIDING coupled with the Buckhingam potential, while having out-of-the-box parametrisation for atomic charges and better performance. In addition, RDF analysis shows that the structural differences between both force fields are not significant.

Our simulations on EPON-862/DDS show the clear presence of a distinct interface region adjacent to the carbon fibre-like surface that differs from the centre region. Density, molecular orientation, and molecular conformation in the centre region all match values found in bulk, while these same values differ in the interface region.

At the interface, density is higher and shows some evidence of layering, however this increase is almost exclusively due to the preferential adsorption of EPON-862 molecules. In the centre region DDS is the excess molecule, although this is considered an artefact of the finite system size that I simulate. Similar to density, the surface has a short range effect on molecular orientation with both EPON-862 and DDS molecules preferring their rings to have a more parallel alignment next to the surface while in the centre region their orientations are random. Molecular conformation also seems to be affected with molecules near the surface preferring a more stretched conformation, but this effect is small when compared with molecular orientation.

While the surface seems to have only a short range effect on structure, displacement is greatly affected even for molecules at a longer range, and larger simulation cells are required to study this effect in detail. However, the excess of EPON-862 at the surface, coupled with a slower overall diffusion, can result in unreacted molecules remaining after the curing process, thus weakening materials properties. Such insight into the interface region of pre-cured composites is valuable for the research and development of new materials.

5. Developing a crosslinking model

This chapter aim is to develop a crosslinking model capable of creating realistic networks, of generic polymers, from liquid starting configurations.

The model system starts with a liquid that undergoes crosslinking to form a polymer network. The liquid is represented with a Lennard-Jones (LJ) model. I present the model and its properties, namely extent of reaction and polymer length distribution, for a monotype system, establishing a basis for the model ustilisation. I then apply and validate the model for use on a binary system.

Firstly, the LJ liquid and the kremer-Grest (KG) models are presented and described, since they form the foundation for this work. Then, the underlying theory behind polymer and thermoset growth is presented and discussed. Lastly, background information about the available methods for performing reactive MD is provided, and some studies are highlighted showing their application.

This is followed by my own work where I describe the basic force field and system setup parameters for my simulations. Afterwards, I test my LJ liquid system at constant pressure, and then use it as the starting point to perform crosslinking simulations on a monotype systems before progressing to binary systems. I construct and make use of a mathematical model to guide final decision making for choice of parameters. I end by establishing a baseline bulk crosslinked system to be used as a comparison in the next chapter.

5.1 Introduction

In this chapter, I want to develop a crosslinking model capable of creating realistic networks, of generic polymers, from liquid starting configurations.

Generic ”bead-spring” type systems have been around since the dawn of MD simulations. The LJ liquid system results from the cumulative development of these types of models, and is capable of accurately simulating a generic liquid whose properties can provide insight into the behaviour of other, more chemical significant, liquids.

Similarly, generic polymer models have been targets of extensive research, and provide a way to extract qualitative data on polymer behaviour that is, otherwise, impossible to get from standard MD simulations given their current time and size constraints. The Kremer-Grest (KG) model has long since been the standard model to study, and research these types of systems, however it was developed for systems of non-reactive polymers.

Both these models were originally developed to work at constant volume, and have been extensively used independently from each other. I plan adapt them to work at constant pressure, and bridge the gap between them to develop a model capable of starting from an LJ liquid configuration to achieve a crosslinked polymer network.

In addition, I also plan on tuning the model so that the properties of the crossslinked network are in agreement with expected results based on Flory's polymer growth theory for linear polymers, and with expected results from an industrial curing process.

5.1.1 Lennard-Jones liquid

The Lennard-Jones potential is a well established potential form utilised, from the very first MD simulations, to model van der Waals interactions between particles, either atoms or molecules [11, 78, 97, 133]. In this work, it has been described in detail section 3.6.2. Regardless, for convenience, the more common form of this potential is also shown here:

$$\mathrm{U_{LJ}} = 4\epsilon\left[\left(\frac{\sigma}{r}\right)^{12} - \left(\frac{\sigma}{r}\right)^{6}\right] \tag{5.1}$$

where σ and ϵ are the distance and energy parameters, respectively. This potential has been used to model non-bonding interactions of simple fluids, which are commonly addressed as LJ liquids or fluids, and is the basis for the development of most modern force fields with application on complex systems [113, 114].

In contrast with the complex models they serve as a basis for, LJ liquids are common model systems that are composed of hard spheres, which represent individual molecules (or monomers), and that interact and move according to the LJ potential

[11, 78, 97, 133]. These systems have been object of intensive studies, and have been used to test theories and implementation of new methodologies, since their simple nature allows for the fast production of qualitative data [113].

As a simple monomer system, the LJ liquid has had its thermo and physical properties well studied and documented, over several different studies, for a range of different simulation conditions [6, 110, 113]. In particular, the radial distribution function (RDF) provides great insight into liquid structure, and a simple frame of reference to validate my own simulations.

Typically, for an LJ liquid, its RDF will vary depending on density and temperature conditions of the simulation, however there is a strong prevalence for them to display at least two evident peaks at 1.122σ and 2.244σ [6, 81, 109]. Other peaks tend to be more visible at higher densities and lower temperatures, and appear at subsequent intervals of 1.122σ following the second peak [6, 109].

5.1.2 Kremer-Grest model

The Kremer-Grest model is the research standard model for studying the properties of generic polymer models using MD simulations [38, 62]. Similarly to the LJ liquid, it is a simple model because it approximates all atoms and/or molecules as hard spheres, sacrificing chemical resolution for performance. However, it excels at generating qualitative information from very simple MD simulations, and this can be used to provide insight into how polymer behaviour changes depending on conditions.

Under the KG model, all particles, both bonded and non-bonded, interact with each via the Weeks-Chandler-Anderson (WCA) potential [130], which is a purely repulsive, and shifted form of the LJ potential, and is defined by:

$$\mathrm{U_{WCA}} = \begin{cases} 4\epsilon\left[\left(\frac{\sigma}{r}\right)^{12} - \left(\frac{\sigma}{r}\right)^{6}\right] + \epsilon, & \text{if } r \geq r_c \\ 0, & \text{if } r < r_c \end{cases} \tag{5.2}$$

Where σ and ϵ hold their standard meanings from the LJ equation, and r_c depicts the point at which the energy, according to this potential, becomes zero.

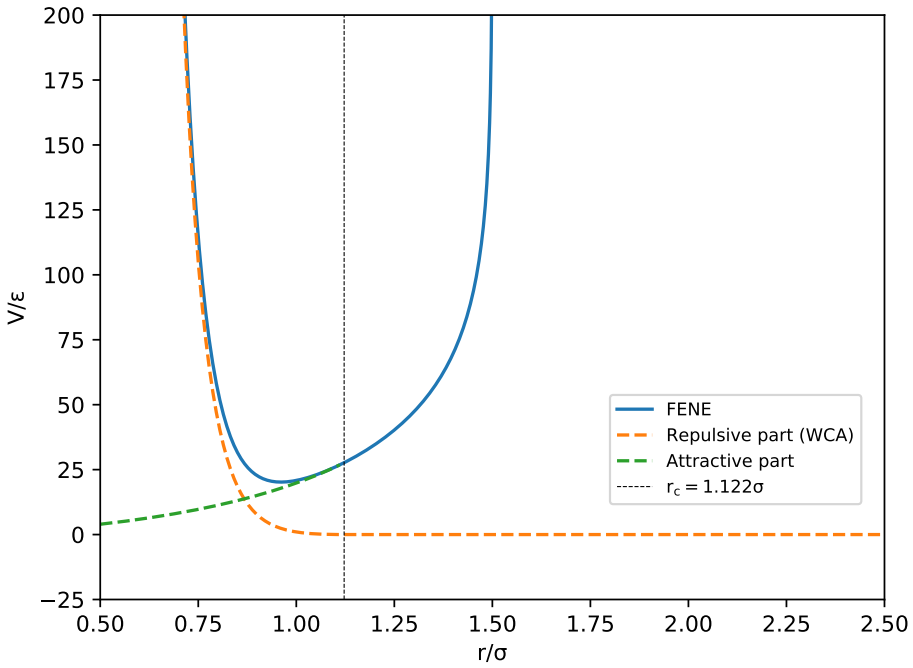

Figure 5.1: Decomposition of the FENE potential into its repulsive and attractive parts.

Bonded interactions are modelled by the finite extensible non-linear elastic (FENE) potential, shown in Figure 5.1 and defined in equation 5.4:

$$\mathrm{U_{FENE}} = -\frac{1}{2} K_{ij}\, r_{0,ij}^2 ln\Big[1 - \Big(\frac{r}{r_{0,ij}}\Big)^2\Big] \tag{5.3}$$

where K_{ij} is the force constant, $r_{0,ij}$ the maximum extensibility of the bond, r_{ij} the distance between the bonded particles i and j. The FENE potential takes the shape of a logarithmic function, hence it displays an asymptotic behaviour which prevents bonds from stretching infinitely. This maximum (or finite) extensibility is also the reason the FENE potential is named as such.

These two potentials used together form the basis of the KG model. Two bonded particles, i and j, are subject to both these potentials forms simultaneously, as defined by:

$$\mathrm{U_{KG}} = -\frac{1}{2} K_{ij}\, r_{0,ij}^2 ln\Big[1 - \Big(\frac{r}{r_{0,ij}}\Big)^2\Big] + 4\epsilon\Big[\Big(\frac{\sigma}{r}\Big)^{12} - \Big(\frac{\sigma}{r}\Big)^{6}\Big] + \epsilon \tag{5.4}$$

where the FENE term forms the attractive part of the potential and the WCA term represents the excluded volume for any given particle.

Under the KG model, typically, equilibrium distance of bonded particles is smaller than of non-bonded particles. This means that particles in the same polymer molecule tend to be closer to each other than with particles belonging to other polymer molecules, increasing the ability that a single polymer molecule has to displace within a polymer melt.

In addition, the purely repulsive nature of the WCA potential and, its use to model all non-bonded interactions in the KG model makes it so that simulations performed using this model are usually done at constant volume. However, several authors have successfully simulated generic polymer systems at constant pressure using KG with the WCA potential.

5.1.3 Polymerisation growth

Typically, molecules in thermoset materials bond with each other following a step-growth polymerisation mechanism. In this mechanism, bi-functional or multifunctional monomers bond with each other to form dimers, trimers and other small oligomers which in turn bond together to form increasingly larger polymer chains. This type of polymerisation also does not require initiator molecules to be present. This nature of step-growth polymerisation means that high extents of reaction are required for a system to yield higher polymer weights since molecular weight increases slowly at the beginning of reaction and increases exponentially as the reaction progresses. A schematic representation of step-growth polymerisation can be found in Figure 5.2.

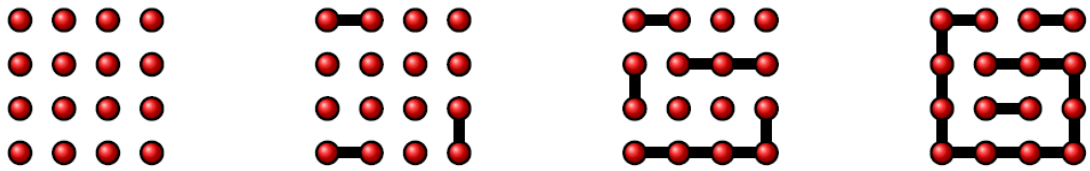

Figure 5.2: Schematic representation of step-growth polymerisation mechanism. From left to right: Evolution of of reaction over time.

The simplest simulated system that can undergo step-growth polymerisation con-

sists of a single bi-functional monomer type where every single monomer can bond to each other to grow linear polymers. Before polymerisation, such a system is akin to a Lennard-Jones liquid, which is a system characterized by spherical particles that interact with each other via only the LJ potential. As the system cross-links, its molecular weight distribution can often be predicted by the Flory-Schulz distribution when the assumption is made that each individual particle has an equal chance of reacting, regardless of the size of the polymer it belongs to. This assumption is called the Flory's equal reactivity principle, and it also states that the probability that a given monomer has reacted is proportional to the extent of reaction, p, which is the portion of all reacted monomers of the same type. The probability that a polymer is composed of X monomers, P_X, is given by:

$$P_X = (1-p)p^{X-1} \tag{5.5}$$

where $(1-p)$ represents the probability of finding an unreacted monomer, and p^{X-1} the probability of $X-1$ reactions have occurred. P_X is also equal to the mole fraction, given by n_X, of X-mers at any given time during reaction. Knowing that the mole fraction is given by the ratio between the total number X-mers, N_X, and the total number of polymers of all sizes, N, the total number of X-mers can be written as:

$$N_X = N(1-p)p^{X-1} \tag{5.6}$$

The total number of polymers of all sizes relates to the initial number of monomers, N_0, by:

$$N = N_0(1-p) \tag{5.7}$$

Substituting equation 5.7 into equation 5.6 yields:

$$N_X = N_0(1-p)^2p^{X-1} \tag{5.8}$$

which is the mole fraction distribution. Based on this simple equation it is possible

to predict the number distribution of polymer sizes based on the initial number of monomers in reaction and the final extent of reaction achieved. Using the relationship between weight fraction, W_X, and mole fraction:

$$W_X = X\frac{N_X}{N_0} \tag{5.9}$$

it is possible to calculate the weight fraction distribution for a specific reaction:

$$W_X = X(1-p)^2 p^{X-1} \tag{5.10}$$

which is also know as the Flory-Schulz distribution. This theoretical work, and the form of this distribution implies that shorter polymer lengths are favoured for lower extent of reaction values, and that this trend starts to reverse for higher extent of reactions where longer polymers start to become more common. This trend is common to both the number fraction and weight fraction distributions, as can be seen in Figure **??**. This is also the expected behaviour from thermoset polymers that follow a step-growth polymerisation mechanism.

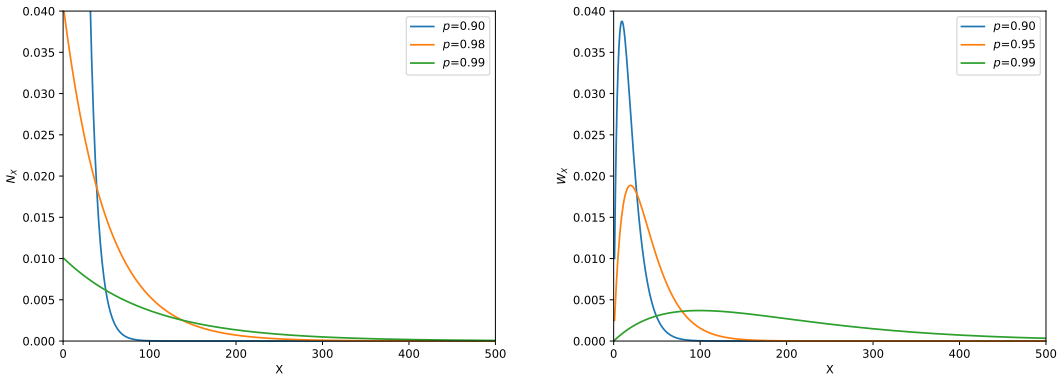

(a) (b)

Figure 5.3: Influence of extent of reaction (p) in (a) number fraction distribution and (b) weight fraction distribution.

Knowing how to predict the number and weight distributions based on results from specific crosslinking simulations provides a useful tool for model for model validation. As mentioned in section 5.1, the application of most generic models to tackle crosslink-

ing reactions has been limited, mostly, to simulations performed under constant volume which does not account for volume shrinkage. The few studies available that simulate systems at constant pressure provide little insight into the selected pressure values. In this chapter, I use a generic model to simulate a standard LJ liquid and establish a baseline. I also validate a set of conditions to simulate an identical system under constant pressure. I then use these results to simulate a crosslinking reaction, using the KG model as basis, of linear polymer chains to account for volume shrinkage and use polymer theory as a validation tool for my results. Lastly, I utilise all the information gathered to develop a KG based model to study crosslinking at the interface region.

5.1.4 Crosslinking

Several approaches have been developed and utilised over the years to simulate chemical reactions with classical MD simulations [33, 41, 61, 71, 79, 89, 121, 123, 134]. Despite the challenge it poses, modelling chemical reactions using classical MD is still of great interest, and other classes of methods have been developed and implemented over the years with the aim of modelling chemical reactions using MD. These can be divided into two separate classes: the first of these classes is based on developing force fields specifically designed to account for chemical reactivity, by using functional forms to describe bonds between atoms and molecules that, unlike the symmetric harmonic potential, allow for bond breakage and creation. These methods attempt to take into account realistic depictions of chemical reactions and are hence designed as ”empirical reactive force fields”; the second class of methods disregards any consideration for any realistic depiction of chemical reactions. Instead, an artificial bond is made between two compatible atoms or molecules if they are within a pre-determined spherical range of each other. Methods in this class are solely based on distance between particles, as shown in Figure 5.4, and are called ”reaction cutoff distance methods”.

Some empirical reactive force fields, such as the Adiabatic Reactive Molecular Dynamics Technique (ARMD) by Meuwly *et al.*[79], are based on standard force fields,

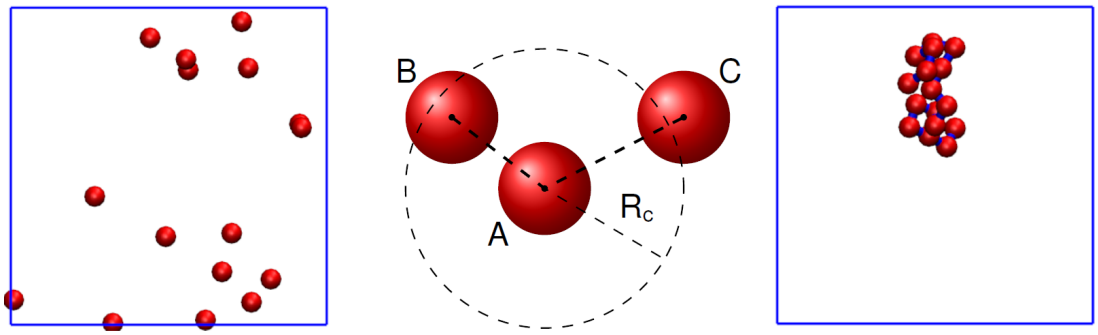

Figure 5.4: Schematic representation of reaction cutoff distance methods. On the left it is represented an LJ liquid containing free roaming monomers, and on the right it is shown the polymer molecule formed by the free moving monomers after bonding. The diagram in the centre indicates the sphere of influence, of radius R_C, of particle A which selects particle B as a bonding partner while excluding particle C.

and add modifications that involve trading the harmonic bonding potential for another potential form, while others like the Reactive Force Field (ReaxFF) by VanDuin *et al.*[121], are based on bond-order parameters and are completely novel force fields with their own parametrisation. What all of these approaches have in common is that a continuous transition region is considered when the reactants move towards the products (or vice-versa), and the use of switching functions based on hyperbolic tangent functions is common to describe that transition. The use of switching functions based on hyperbolic tangents has long be common in QM methods [23].

The ReaxFF force field is currently the flagship empirical reactive force field method of choice for modern MD simulations. In it, the potential energy is described by:

$$V = V_b + V_{angle} + V_{torsion} + V_{LJ} + V_{Coulomb} + V_{penalty} + V_{conjugation} + V_{undercoordination} + V_{overcoordination} \quad (5.11)$$

where V_{angle}, $V_{torsion}$, V_{LJ} and $V_{Coulomb}$ are the typical contributions from angles, dihedrals, van der Waals and Coulomb forces also found in standard force fields. The last four terms are exclusive to ReaxFF force field and relate to the reactivity allowed by the force field. The first term, also exclusive to ReaxFF, takes into account the dis-

sociation energy and bond order between two specific atoms. The latter of these two parameters is dependent on the distance between the two atoms, and is different for single, double, and triple bonds.

ReaxFF was originally developed for hydrocarbons and has since been updated to contain other atomic species[61]. The way ReaxFF treats bonded pairs and dissociation energy makes it so that only atom type is required for each atomic species, and interaction between different species is dependent almost exclusively on their dissociation energy and bond order parameters making it, in theory, simpler to update.

These methods rely on heavy parametrisation, either via force field modification or development, hence if a specific atom of molecule type is not contemplated in their parameter space they cannot be used. Because of this, they also have limited application in highly coarse-grained systems until such parameterisation is done.

Methods based on reaction cutoff distance can be used with an already established force field, meaning that no extra parametrisation is necessary. This makes their use more straightforward than that of empirical reactive force fields methods. Another important consideration is that they can be used not only with material specific force fields, such as DREIDING and OPLS, but also with coarse-grained and generic potentials.

Varshney *et al.*[123], Wu *et al.*[134], and Walsh *et al.*[33] have used reaction cutoff distance methods in combination standard force fields in simulating fully atomistic systems.[31, 33, 123, 134]

The work of Varshney *et al.*was briefly discussed in the previous chapter regarding their investigation of the EPON-862/DETDA system. However, their approach towards generating the crosslinked network was not mentioned then, but becomes relevant in the context of this chapter. Their approach was to setup four separate crosslinking algorithms: the first assuming equal reactivity of both the primary and secondary amines; the second assumed that the primary amine has the higher reactivity of both; the third forced the full reaction of a randomly selected nitrogen atom before allowing another to react; the fourth and last followed the equal reactivity principle and allowed for the simultaneous reaction of all reactive pairs. The motivation behind each of these

approaches was to determine which was able to achieve an equilibrated crosslinked network with the lowest energy structure. They have found that their fourth and last approach yielded the best results, and best agreed with the literature when looking at density, volume shrinkage, and thermal expansion [123].

Wu *et al.*[134] have developed their polymerisation methodology based on a system comprised of the resin diglycidyl ether bisphenol A (DGEBA) coupled with isophorone diamine (IPD) acting as a cross-linker. They have used both COMPASS [116] and DREIDING as their force fields for this study, with partial atomic charges calculated using the charge equilibration (Qeq) method. They have also removed all the hydrogens from the active functional groups, leaving only the reactive carbons and nitrogens. A total of 16 DGEBA and eight IPD molecules were packed in a cubic periodic simulation box at a density of 1.131 $\mathrm{g\,cm^{-3}}$. They utilised a relaxation procedure comprised of energy minimization, followed by annealing in-between crosslinking iterations to minimize the change of trapping the structure in a local minimum. They have found good agreement with experimental properties with the COMPASS force field comparing more favourably than DREIDING, attesting to the importance of force field choice to describe a realistic system [134].

Walsh *et al.*[33] have focused their efforts into creating a reproducible protocol for the creation of equilibrated crosslinked networks using an EPON-862 and DETDA system identical to the one I have also used in the previous chapter. Mainly, they have provided details on calculating partial atomic charges as well as validating a liquid precursor mixture and generating the three-dimensional network. Their model uses the DREIDING force field with the Buckingham potential to describe non-bonded interactions. The conjunction of this potential with charges calculated using the Qeq method have produced a liquid precursor mixture whose properties better match experimental results. Thermo-mechanical properties of the cross-linked network were also found to be in agreement with the literature further validating their method [33].

Outside of material specific force fields, reaction cutoff distance methods have also been applied with generic models such as as the Kremer-Grest (KG) model [62] or the reflected Week-Chandler-Anderson (WCA) potential [130], initially developed for

simulating non-reactive polymers.

Perez *et al.*[89] and Liu *et al.*[71] have used the KG model with a reaction cut-off distance method to perform the polymerisation of linear chains in bulk, and chain growth of surface grafted polymer chains, respectively. Both of these studies have used initiator molecules to start the reaction, with Perez *et al.*having theirs dispersed in bulk while Liu *et al.*had theirs at the surface. While Perez *et al.*provide details on the ensemble used for their simulations, and state that they ran at constant pressure, they provide no insight into the selection of this value. Liu *et al.*on the other hand kept system density constant, as per the work of Soddemann *et al.*[110].

The reflected WCA potential mirrors the typical WCA at its minimum, forming a quasi-harmonic potential which is then used to describe bonded interactions. This potential has been employed by Akkermans *et al.*[9] to achieve irreversible bonding between particles in bulk. The idea behind this method is that when two particles bond, they become trapped in the reflection of the WCA potential causing a seamless transitions between non-bonded and bonded states. However, the purely repulsive nature of the WCA potential demands that simulations be done at constant volume.

I know from the works of Varshney *et al.*[123], Wu *et al.*[134], and Walsh *et al.* [33] that volume shrinkage occurs when a thermoset system undergoes crosslinking, and the same is to be expected from generic models, especially when they utilise the KG model since equilibrium bond distance is typically shorter than non-bonded interactions in this model. Hence, I deem it necessary to run simulations at constant pressure instead of constant volume to better capture the crosslinking behaviour, like it was done by Perez *et al.*. However, it also find it important to find and validate a realistic pressure value that can capture the same patterns as already established by constant volume models which are standard for models such as KG and reflected WCA.

5.2 Methodology details

5.2.1 Force field parameters

For all simulations, mass, σ, ϵ and the Boltzmann constant ($\mathrm{k_B}$) were set to one. All other units and quantities are specified as multiples of these fundamental quantities. Similarly to the last chapter, all simulations were performed using the LAMMPS software [94], and periodic boundary conditions were applied in all directions.

For the LJ systems, the parameters as described by Soddemann *et al.*[110] were used, and cross-referenced them with NIST parameters [6] in order to setup my own LJ liquid simulation. Particles interact only via the LJ potential, and both σ and ϵ are equal to one.

When crosslinking takes place (initially as simple polmerisation and then as several polymer chains bonding with each other), the FENE potential is used to describe bonded interactions which replace non-bonded interactions between affected particles. Parameters for equation 5.4, describing the FENE potential, are as described by the original authors [62], and are of $\mathrm{K_{ij}}$=30, $\mathrm{r_{0,ij}}$=1.5 and σ=ϵ=1. Note that selecting different values of σ and ϵ for the FENE potential does not affect the fundamental quantities mentioned at the beginning of this section.

5.2.2 System setup

For the LJ liquid simulation at constant volume, a cubic simulation box was populated with 2000 randomly placed particles at a density of 0.844 $\rho\sigma^3$, targeting a typical LJ liquid [6]. For the same system, at constant pressure, a value of 2.569 $\rho\sigma^3$ was used for the pressure, as this value prevents the density from greatly fluctuating from that expected from an LJ liquid. For both these simulations, temperature was always kT/ϵ=1.0, and a 0.005 τ timestep was used, as is standard for LJ liquids [6]. Both simulations ran for a total of 100,000 timesteps making up for 500 τ.

Crosslinking simulations were performed in batches to improve statistics. A total of 100 different starting configurations were constructed, by inserting 2000 particles

randomly inside a a cubic box at a density of 0.844 $\rho\sigma^3$. Particles have the same parametrisation as in the LJ liquid. Time between crosslinking iterations was of 1000 timesteps, and a total of 500 iterations were performed per simulation making each simulation 500,000 timesteps, or 2500 τ long. The reaction probability was initially set to 100% unless specified otherwise and is independent on molecular size, in agreement with Flory's equal reactivity principle. The minimum distance required for a bond to be formed is equal to 1.122 σ, which is the equilibrium distance for the LJ potential with the specified σ and ϵ values.

In addition, initially, surface-monomer interactions were equal for all particles. However, particles were then classified with two distinct labels and surface-monomer interactions were made different for each monomer species to study the effects of asymmetric surface-monomer interactions in the resulting crosslinked network.

5.3 Results and Discussion

5.3.1 Lennard-Jones liquid

Addressing the structure of the liquid, the radial distribution function (RDF) is shown in Figure 5.5, and depicts a sharp peak around 1.122 σ, which corresponds to the equilibrium distance between LJ particles according to parametrisation, followed by a second peak located at 2.244 σ. Both the positions and heights of these peaks are in agreement with the literature for similar temeprature and density conditions [109].

This RDF provides me with a measure of confidence in the way my system is set up, hence it is used further as the basis for the development of my method for crosslinking simulations. Next, pressure was averaged over the simulation runtime, and was found to be 2.569 $\pm$0.133 $\rho\sigma^3$. The importance of simulating a system based on LJ liquid for crosslinking has been discussed previously, so this pressure value was kept and utilised for an almost identical simulation at constant pressure, instead of constant volume.

I calculated the RDF from this second simulation, keeping pressure constant at 2.569 $\pm$, and extracted the average density 0.844$\pm$0.004 ρ. Both the RDF, shown in

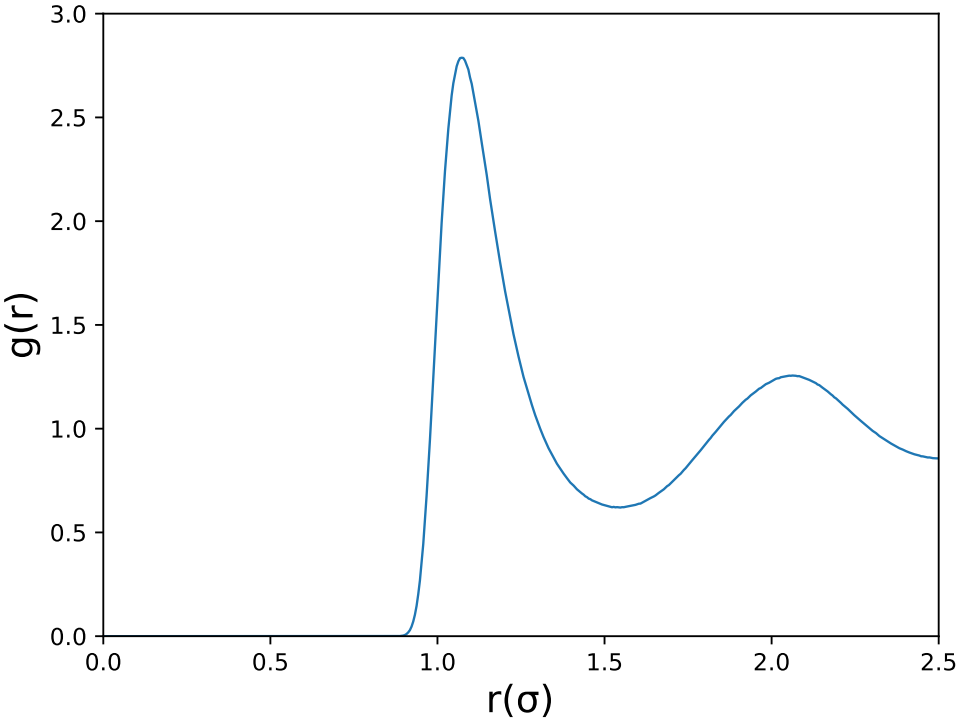

Figure 5.5: Radial distribution function obtained from the LJ liquid system.

Figure 5.6, and the average density of the system point towards this simple change to be sufficient to further develop a model for the crosslinking of generic polymer models.

However, I further validated this assumption by cross-referencing these results with the NIST LJ liquid. NIST provides an extensive characterisation of a simulated LJ liquid at kT/ϵ=1.0, for different densities. These start at 0.001 $\rho\sigma^3$ and go up to 1.0$\rho\sigma^3$, with several data points having been collected from the range between 0.001 $\rho\sigma^3$ and 0.1 $\rho\sigma^3$, and thereafter at 0.1 $\rho\sigma^3$ increments. Part of data showcased pertains to the average pressures for each density.

Our system, at a constant pressure of 2.569 $\rho\sigma^3$, displayed an average density of 0.844$\pm$0.004 ρ, and none of these values are referred to in NIST. Data from NIST was cleaned, and the region of interest, between 0.5 $\rho\sigma^3$ and 1.0 $\rho\sigma^3$, was fitted with an exponential function.

Taking the pressure value into account, the density should have been approximately 0.829 $\rho\sigma^3$, which is slightly under simulation density, even when taking its stan-

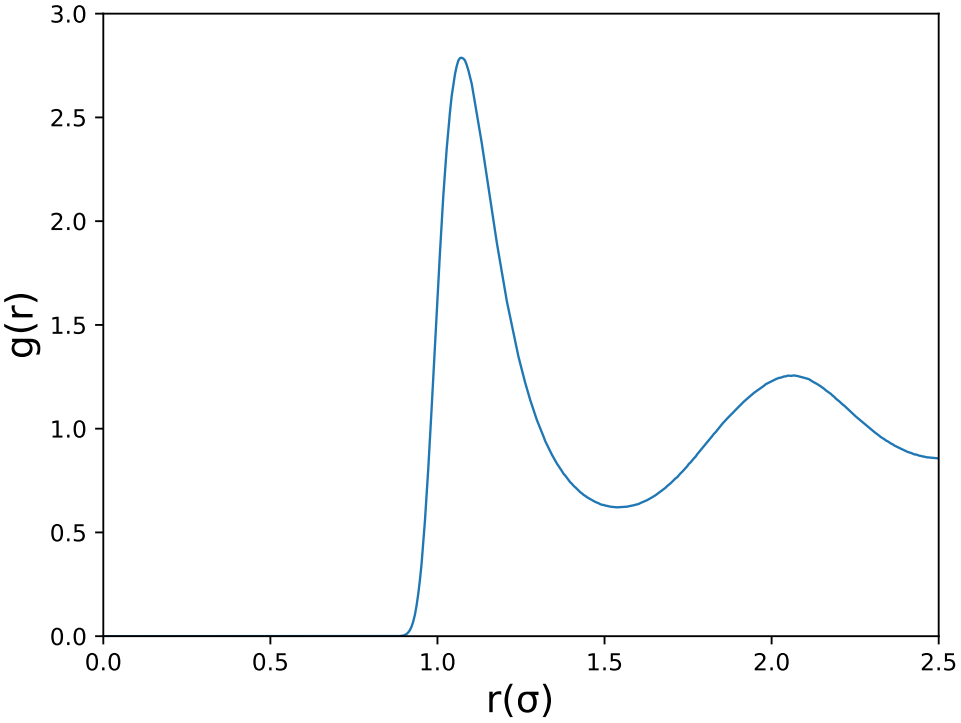

Figure 5.6: Radial distribution function obtained from my modified LJ liquid system at constant pressure.

dard deviation into account. Based on this analysis, at constant pressure, one should expect the achieved density to be slightly greater than that of a LJ liquid at constant volume. However, I consider that the density from a LJ liquid at constant pressure is still within a reasonable range. The importance of having a simulation cell capable of adjusting to the volume shrinkage caused by crosslinking supersedes this slight deviation.

5.3.2 Crosslinking on a monotype system

The first system simulated consisted of a single monomer type, where each monomer particle was allowed to bond to another of its kind up to a maximum of two times. The default crosslinking range of 1.122 σ was utilised, and reaction probability was set to 100%. Results from this batch of simulations are condensed in Figures 5.7a and 5.7b, which show the evolution of the extent of reaction over time, and the final polymer

length distribution of the system, respectively.

The extent of reaction increases rapidly at the beginning of the reaction and quickly stabilizes around its final value of 0.985±0.001 at the end of the simulation. This behaviour is caused by the fact that, at the start, a wide availability of free bonding sites exist, but as these react and become unavailable the reaction slows down, consistently with a step-growth polymerisation mechanism.

The final polymer length distribution of the reaction depicts two important aspects of the system: the first is that the vast majority of formed polymer molecules are cyclical, having bonded back with themselves; the second is that the final distribution is not consistent with the expected number distribution according to Flory based on system size and extent of reaction. In addition, it also appears the majority of the polymers formed contain only a small number of monomers, with most having less than 10 units. The cyclical nature of these smaller polymers prevents them from reacting further to increase in size.

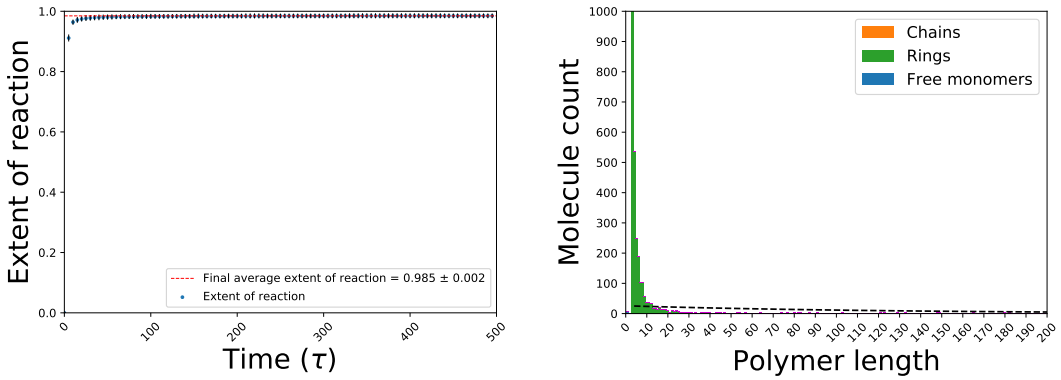

(a) (b)

Figure 5.7: Results for a monotype system. a) Evolution of the extent of reaction over time. b) Polymer length distribution. The black dashed line is the the corresponding number distribution.

The crosslinking algorithm, as implemented in LAMMPS, takes only into account the proximity between two potential bonding particles, the available number of bonding sites in each particle, and their relative distances to create a new bond. Since reaction probability is set to 100%, there is nothing preventing new bonds from forming if

all discussed parameters allow it. Monomers are finding, and bonding with potential, bonding partners at the very start of reaction very close to the initial system configuration.

Our major concern with this model as it stands is the prevalence of smaller cyclical structures, presented in Figure 5.8. Considering the highly simplified coarse-grained nature of this model, each particle could be made to represent an entire molecule, and small cyclical polymer chains are unlikely to happen, given the high energy required to force these structures to occur. That, coupled with the non-overlap of the number distribution curve, tells me that this model is not appropriate to study further crosslinking reactions.

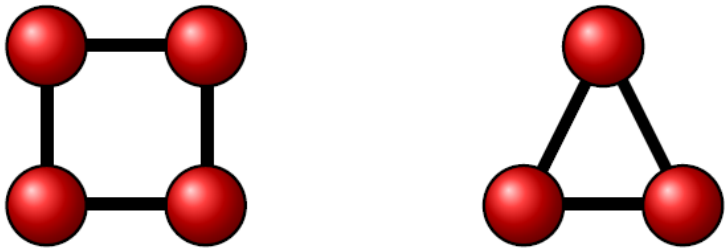

Figure 5.8: Diagram representation of small cyclic crosslinked polymers.

As stated, these small structures are derived from the fast reaction rate imposed by the crosslinking algorithm, and seen by the steep increase of the extent of reaction in the early stages of simulation. The two types of small cyclic polymer structures that most concern me are the triangles and squares presented in Figure 5.8, since these have can have very tight angles.

To prevent the formation of these structures, I postulated that an angle constraint could be used, in addition to the distance cutoff criterium already imposed by the default LAMMPS algorithm, to limit or even suppress the formation of these structures. The schematic in Figure 5.9 shows the theoretical implementation of this additional constraint. In the scenario of two neighbouring dimers wanting to form two simultaneous bonds locking themselves in a squared structure the hypothetical angles between them would also be evaluated. If they failed to fall inside a pre-determined allowed range, then the bond would be forbidden.

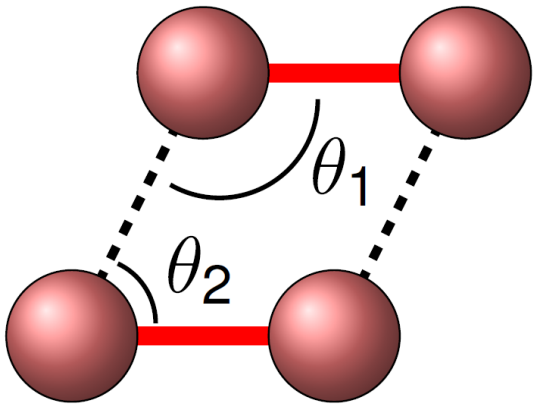

Figure 5.9: Diagram representation of small cyclic crosslinked polymers.

Much like with the reaction cutoff parameter, where both atoms inverting in a potential reaction need to mutually select each other as bonding partners, the same must happen for the angles. Looking at Figure 5.9 again, if the allowed angle is greater than 90° and smaller than 180°, then the particle forming the θ_1 angle allows the bond to be formed because it falls inside that interval, however θ_2 falls outside this interval so the particle forming that angle declines the bond. Both particles need to mutually meet the angle criteria in order for the bond to be formed.

A series of small simulations were performed to implement this modification to the crosslinking algorithm, and to validate my modifications. This was also done to ensure that my modifications did not affect the way that the default algorithm worked in LAMMPS.

Running the same simulation, from the same starting configuration, as before with this added angle constraint of parameter greater 90°, and smaller than 180° produces little differences in the extent of reaction which follows a similar trend after the addition of this parameter and, is show in Figure 5.10a. However, a higher extent of reaction was achieved. Despite that, not much information can be inferred from this change from looking at the final polymer length distribution, shown in Figure 5.10b, which is significantly different from the previous simulation without the angle constraint parameter.

Comparing the polymer length distributions yielded by using the standard LAMMPS

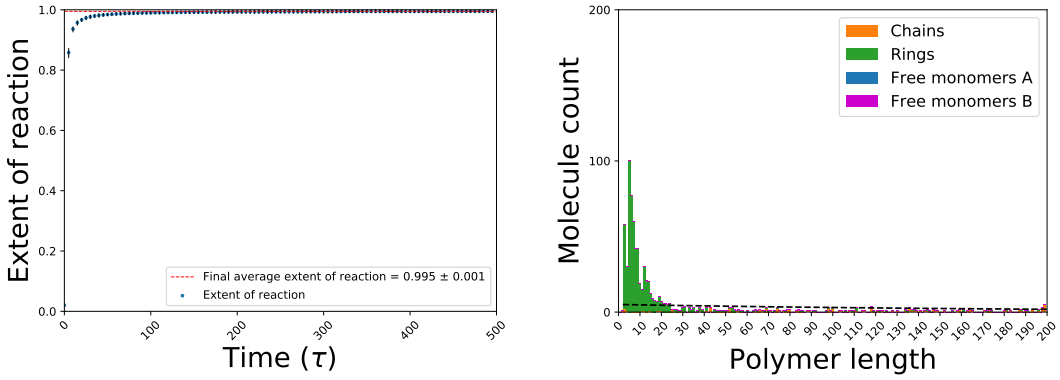

(a) (b)

Figure 5.10: Results for a monotype system with a crosslinking angle constraint. a) Evolution of the extent of reaction over time. b) Polymer length distribution. The black dashed line is the corresponding number distribution.

crosslinking algorithm and my own modified algorithm, shown in Figures 5.7b and 5.10b, respectively, two conclusions can be drawn: the first is that the distribution using my own algorithm is more spread out and produces a significantly lower amount of smaller cyclic polymers, mainly square-shaped polymers, than the original algorithm; the second is that despite this reduction in small cyclic polymers the distribution yielded by my algorithm still does not agree with the expected Flory's number distribution based on system size and extent of reaction.

I recognize that the improvements achieved by the addition of an angle parameter in a monotype system are minimal in terms of improving the expected polymer length distribution, and yield no significant change regarding the evolution of the extent of reaction with time. However, most chemical systems that undergo crosslinking contain at least two different reactive species that can bond with each other. In this scenario, the formation of triangular structures is prevented by the intercaleted nature of the formed polymers, hence minimizing the formation of squared polymers is more relevant, and my model achieved in greatly reducing their formation by five to six times. Further testing and application of this algorithm is detailed in the next section.

5.3.3 Crosslinking on a binary system

So far I have dedicated ourselves to testing both the original LAMMPS crosslinking algorithm and my own modified algorithm on characterising a monotype generic polymer system. However, as stated previously, most thermoset systems are made of, at least, two different species. The only difference between this binary system and the previous monotype system is that half of the particles represent one chemical species and the other half represents another. However, LJ interactions between particles of different species and particles of the same species is identical. The only constraint added is that a particle from one species must bond with a partner from a different one.

Running a batch of simulations for this system, with an angle constraint parameter greater than 90^{o} and smaller than 180^{o} yields the graphs in Figures 5.11a and 5.11b showing the evolution of the extent of reaction over time and the final polymer length distribution. The extent of reaction follows a similar trend to that seen for the monotype systems, and is still consistent with step-growth polymerisation. Total extent of reaction at the end of the simulation was 99.5%, which is high when compared to the expected 95/96% achieved in experiments. The polymer length number distribution on the other hand appears to have been affected by the change from monotype to binary system.

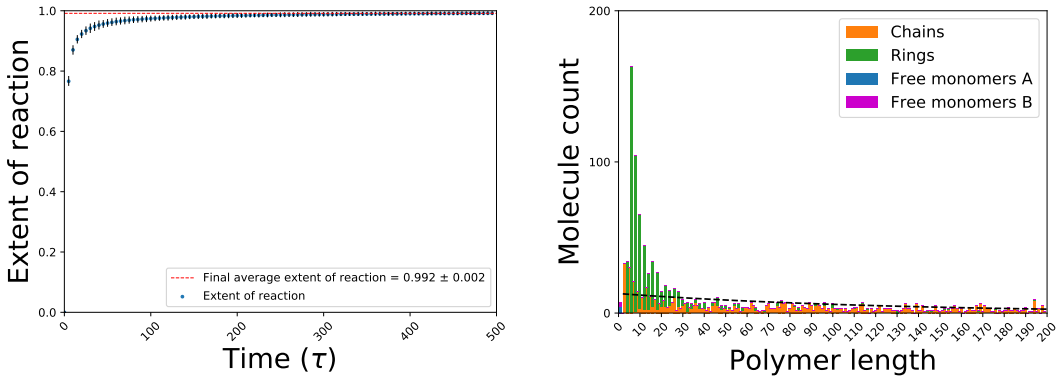

(a) (b)

Figure 5.11: Results for a binary system with a crosslinking angle constraint. a) Evolution of the extent of reaction over time. b) Polymer length distribution. The black dashed line is the corresponding number distribution.

The cyclic polymers still exist, showing that their formation was not fully suppressed by the addition of the angle constraint parameter added to the crosslinking algorithm. However, they have been severely reduced, and are limited to polymer molecules containing an even number of monomers. This is because polymers with an odd number of monomers have the same species of monomer as their chain ends, which cannot bond with each other.

The reason why there is an excess of even-numbered polymers of small length (less than 50 monomer units) is because once these bond with themselves, they remain incapable of further reaction thereafter, so they get stuck at whichever length they self-bonded. Unlike these, odd-numbered polymers can react further, provided that they can find a compatible polymer, or a monomer molecule to bond with, so smaller polymers were lead to bond, forming larger polymer molecules as the reaction progressed.

The other relevant aspect shown by the distribution plot is the overlap between Flory's predicted number distribution and the actual number distribution achieved at the end of simulation by the system. Both these distributions do not overlap fully and it seems that the smaller cyclic polymers are the cause of the discrepancy between them, since the predicted number distribution overlaps better if the cyclic structures are excluded. This is not an unreasonable result, since Flory does make the assumption, in his model, that cyclic polymerisation does not occur.

In order to better understand this behaviour, and the reason MD simulations deviated from expected number length distributions, a simple mathematical model was built based on the rate equations for polymerisation according to a step-growth reaction mechanism. This model assumed perfect mixing, where all monomers are equally likely to be next to each other. A proportion of neighbour monomers are able to react if they are un-bonded or are a polymer chain end. This proportion is akin to a reaction probability, $prob$, and is kept constant for simplicity. The reaction between an i-mer and a j-mer is given by:

$$k_{ij} = prob \times 2\frac{N_i}{N_t} \times 2\frac{N_j}{N_t} \tag{5.12}$$

Where N_t is the total starting number of monomers and N_i and N_j are the starting number of monomers of species i and j respectively. Each monomer is able to form two bonds, hence they are considered equal and this equation can be used for both. The rate for creation is then written as:

$$R(i+j) = R(i+j) + k_{ij} \tag{5.13}$$

And the rate for removal as:

$$R(i) = R(i) - k_{ij} \tag{5.14}$$

Since both monomers can react twice, unlike chain ends which can only react once more, this term is doubled for free monomers. Maximum chain size is limited to 200 monomers, and cyclical polymers are not contemplated. A total of 100 steps are performed, allowing polymer chains to grow according to the rate of creation, and reacted monomers are counted out via the rate of removal. The extent of reaction is calculated at every step and used to calculate the corresponding Flory's number distribution curve.

Setting the reaction probability, $prob$, at 0.1 yields the results shown in Figure 5.12a while setting it five times lower at 0.02 yields the plot in Figure 5.12b. Figure 5.12a shows that produced polymer distribution roughly overlaps with Flory's number distribution, however, it also shows the spikes I saw in my own simulations. With a lower reaction probability, these spikes disappear, and the curve becomes much smoother, and overlaps with Flory's number distribution much better. Results from this model suggest that reaction probability plays a major role in the observed polymer length distribution.

In 5.2, it was mentioned that reaction probability when two potential bonding partners met was always defaulted to 100%. At the time, the choice of this parameter was simple and based on total simulation time with reduced probabilities leading to more time-consuming simulations.

However, based on this new data, this value must be revised. While the reaction

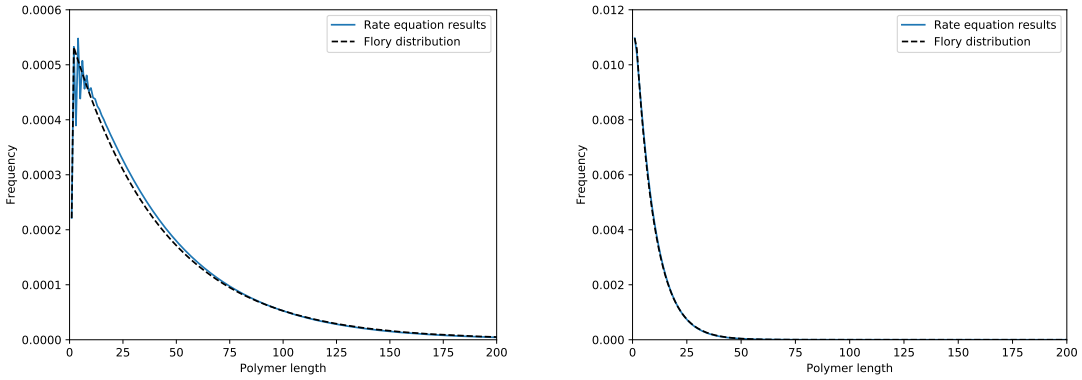

(a) (b)

Figure 5.12: Polymer size distribution according to the mathematical model with a reaction probability of (a) 0.1 and (b) 0.02

probability parameter in LAMMPS is not directly comparable to the reaction probability of my mathematical model, they serve the same end goal which is to slow down the reaction. Another batch of simulations was performed on a binary liquid, with identical parametrisation to the previous simulation with the exception of the extent of reaction, which was set to 50%. In this case, whenever two compatible particles decided to form a new bond, its formation was subject to a ”coin toss” which ultimately decided if it would form or not.

Results from this simulation batch are presented in Figures **??**. The extent of reaction has a similar trend and its value value is of 99.0%, which is near-identical to the extent of reaction with a bonding probability of 100%. Similarly, the number distribution for polymer lengths are very similar. This suggests that reducing the bonding probability by half causes very little change in the way the crosslinking happens.

However, further reducing the bonding probability to 10% causes significant changes in both the extent of reaction and the polymer length distribution, as shown by figure 5.14b. Addressing the extent of reaction first, with this bonding probability it stabilised at 95.4%. This value is significantly lower than previous simulations, with an increased bonding probability, performed on a binary system, and is much closer to what would be expected from experiments for the crosslinking of thermoset polymers. The polymer length number distribution is also very different and not only does it agree

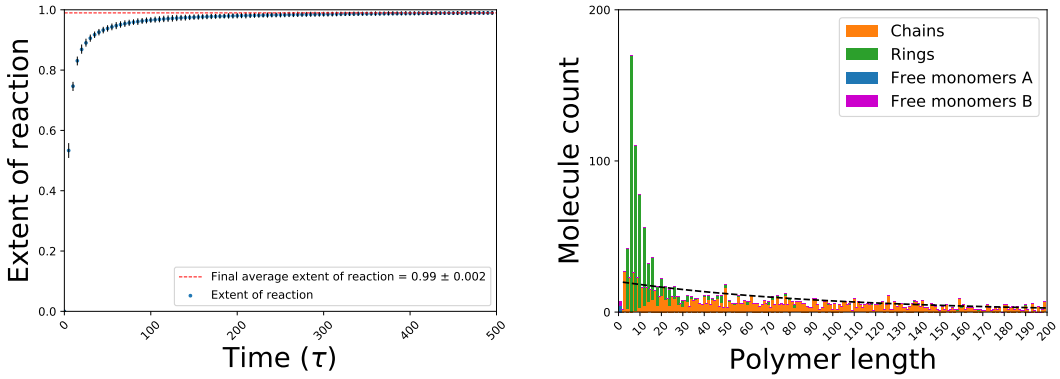

(a) (b)

Figure 5.13: Results for a binary system with a crosslinking angle constraint and reaction probability of 50%. a) Evolution of the extent of reaction over time. b) Polymer length distribution. The black dashed line is the corresponding number distribution.

almost perfectly with the expected distribution based on Flory, but also does not display the spiked behaviour that was present in previous simulations. In addition, this also creates a link between the bonding probability existent in LAMMPS and the reaction probability in my own model.

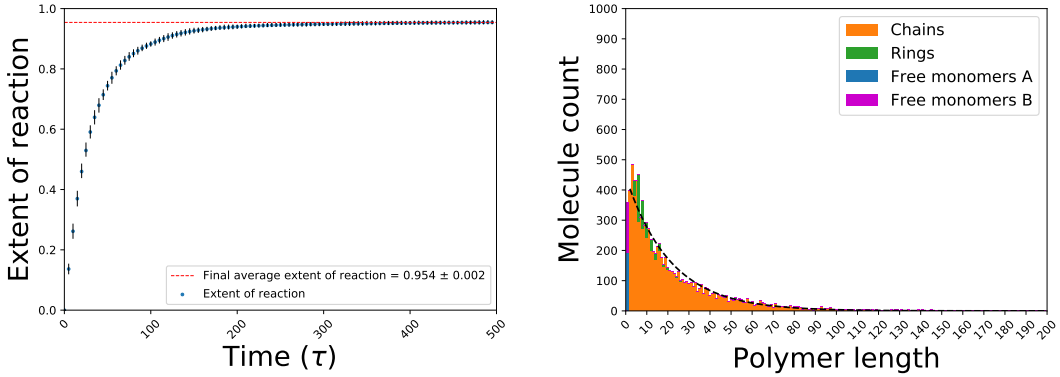

(a) (b)

Figure 5.14: Results for a binary system with a crosslinking angle constraint and reaction probability of 10%. a) Evolution of the extent of reaction over time. b) Polymer length distribution. The black dashed line is the corresponding number distribution.

With this final result, I are confident that my model is adequate to simulate the crosslinking of generic linear polymers at a surface to study its effect on the crosslinked network in the next chapter. This final batch of simulations also serves as a baseline

for comparison of any perturbations caused by the surface.

5.4 Conclusion

Several attempts were made to simulate reactive systems using MD simulations. These are classified into two groups: ”empirical reactive force fields” and ”reaction cutoff distance methods”. The latter has been successfully used in the study of polymerisation using generic polymer models. In this chapter, I have shown how the modified the default algorithm for the ”reaction cutoff distance method”, as implemented in LAMMPS to add an additional constraint based on angle amplitude, and used it to establish a baseline crosslinked system mimicking a step-growth mechanism.

Our results show that an LJ liquid system is simulatable at constant pressure, and is only slightly different from one at constant volume in terms of the relationship between pressure and density. In addition, my results using the default LAMMPS crosslinking algorithm on a monotype system based on an LJ liquid at constant pressure, show that it is unable to create a realistic crosslinked network, and generates a large amount of small cyclic polymer molecules. These molecules, especially ones containing three and four monomer units, display very tight angles which would be unrealistic if the system was back-mapped to full atomistic resolution.

Application of my own modified crosslinking algorithm to enforce the angular amplitude between potential bonding partners as an added criterium for crosslinking improved the resulting network for a monotype system. Despite the significant reduction in the formation of small cyclic polymer molecules, a large amount still remained. A decision was made to move to a binary system which is more representative of reality.

For the binary system, a much more significant reduction of small cyclic polymers took place. However, a clear differentiation between between the size of even-numbered and odd-numbered polymers, particularly for polymers of smaller size (less than 50 monomer units) was seen. This behaviour was partially explained by the AB reaction scheme enforced by the simulation, and also by the use of a mathematical model which highlighted that the reaction probability played a role in reducing this gap

in behaviour.

Reducing the bonding probability on the crosslinking algorithm down to 10% produced a crosslinked network with an extent of reaction of 95.4%, which is comparable to experiments. In addition, the evolution of the extent of reaction over time is consistent with a step-growth polymerisation mechanism. The final crosslinked network, in terms of its polymer length distribution, was shown to agree with predictions for this system based on Flory's number distribution.

Thus, I have established an adequate algorithm to model the crosslinking reaction of generic thermoset polymers. I also have established a baseline system which will be used in the next chapter to study the effects of a surface on polymer crosslinking.

6. Surface effect on polymer network formation

As discussed in Chapter 2, for composite materials, the strength of the interactions between the surface and the polymer matrix, referred to as adhesion, plays a major role in the ability of a composite to resist failure.

In this chapter, I utilise the crosslinking model that I developed and described in Chapter 5 to study the effects caused by the presence of a surface on crosslinked polymer networks.

Firstly, two different crosslinked networks will be subject to comparison: the crosslinked network achieved for a bulk system in Chapter 5, and the crosslinked network of an analogous system with a surface. This is followed by an analysis of the pre-polymerised liquid, where finite effects become evident, and system size is rescaled for the continuation of this work. This will also involve determining the effects that the surface has on liquid density prior to crosslinking.

The effects of surface interactions will also be studied by making one of the particle types more strongly attracted to the surface than the other. The structure of the resulting polymer networks yielded by these simulations will be analysed.

6.1 Introduction

Before curing takes place, molecules in a pre-polymer liquid mixture diffuse and rearrange themselves according to the existing intermolecular interactions between them and the fibre surface. Molecules with greater affinity towards the fibre are expected to aggregate closer to its surface, while molecules which are less attracted towards it are displaced from the surface. This behaviour was discussed in Chapter 4, and understanding it, and its effects on crosslinked polymer networks, is one of the main objectives of this work.

The crosslinking model developed in Chapter 5 is utilised here to investigate the key qualitative differences between a crosslinked network achieved in a bulk system, compared with one achieved near a surface. In addition, the effect of having greater attraction between one molecular species and the fibre is also investigated in terms of its effects on the crosslinked polymer network.

6.2 Methodology

Simulations were performed using the LAMMPS program [94], using the modified algorithm developed for crosslinking. Lennard-Jones (LJ) units are used. The fundamental quantities of every simulation are mass, $\sigma*$, $\epsilon*$ and the Boltzmann constant ($\mathrm{k_B}$). These are all set to one, making all other quantities multiples of these fundamental values, so that I use dimensionless quantities, as per LAMMPS documentation [94].

All parameters for the LJ potential and the Kremer-Grest (KG) model are identical to the ones described in the previous chapter, and particles in the surface are made of immobile monomers. Surface particles had identical interactions to monomer particles, however they were kept immobile during simulation. While the interactions between monomers was kept unchanged, the surface potential interacted with the monomers via an LJ potential whose σ and ϵ were varied.

The model system consisted of a face centre cubic slab, made of generic particles, that occupies the entirety of the xy plane. The surface is repeated across periodic boundary conditions and the space between the surface and its image is populated with free roaming generic particles. An example system is detailed in Figure 6.1.

The size of the simulation box is 14.62$\times$14.62$\times$24.57σ^3 and a lattice constant a=1.044 was used to construct the face centre cubic slab. Surface particles were kept fixed and immobile during simulation run-time. Periodic boundary conditions were applied in all directions.

Slab thickness was sufficient to prevent cross-surface interactions between monomer or polymer molecules, being five layers thick and with an AB stacking. The central layer was located at the z=0 place, with two of the layers being translated back into

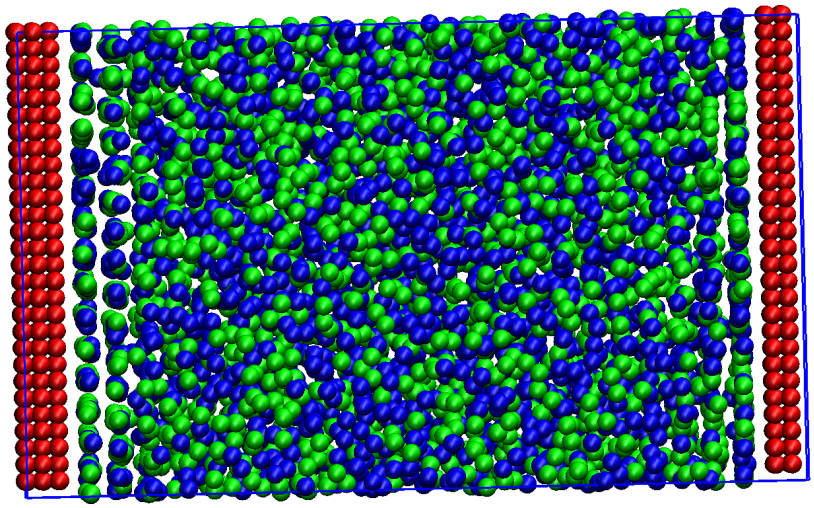

Figure 6.1: Snapshot of a confined system. Red particles spheres represent the surface atoms, while blue and green spheres represent monomer A and monomer B particles respectively.

the other side of the simulation box across periodic boundary conditions. Layers are 1.044σ apart.

Particle overlap, caused by the random placement of particles in the inter-slab space, was removed by subjecting the monomers to an NVE simulation for the duration of 10000 timesteps. During the de-overlap procedure, maximum particle displacement was limited to 0.1σ. This was followed by an NVT simulation of the same duration to mix and equilibrate the system. These steps were common to both liquid and crosslinking simulations.

Simulations for liquid simulations we performed for 500,000 timesteps at constant pressure of 2.569 $\rho\sigma^3$ However, pressure conditions were anisotropic and only the monomers were subject to pressure change in the z direction. Crosslinking simulations were performed using an identical set of conditions, however crosslinking iterations took place over 500 equally spaced iterations over the 500,000 timestep period. To obtain better statistics, each system was repeated 100 times with different starting configurations. This was done to achieve meaningful statistics from analysing the results, but also due to technical limitations as the current version of this model in LAMMPS does not support parallelisation.

6.3 Results and Discussion

6.3.1 Liquids and finite size effects

The effect of the surface on liquid mixtures was evaluated by calculating the density profiles of several systems, where one of the chemical species in the binary mixture has varying degrees of affinity with the surface. The plot in Figure 6.2a shows the density profile, which is density measured as a function of distance from the surface, for a simulation that will edescribed in detail in subsection 6.3.3. It shows that density fluctuations derived from the presence of the surface propagate trough the entire simulation box, indicating that finite size effects are present, and that the system does not reach an homogeneous density (i.e. ”flat”) far away from the surface.

The density profile in Figure 6.2b refers to a system where the amount of particles was doubled, when compared with the system that generated the density profile shown in Figure 6.2a. Surface area is identical in both system, however the increase in amount of particles reflects itself in an increase of the length of the z axis, which is approximately doubled. In addition, the dashed lines, corresponding to the individual contributions of each chemical species towards density, overlap precisely, suggesting that both systems are properly mixed.

While in both systems it is noticeable that liquid density is affected by the surface, on the larger system there are clearly depicted two different regions, in terms of density: density fluctuates at the interface region; and stabilises at the centre of the film. This initial set of two simulations indicates the size requirements for the simulation box to avoid encountering finite size effects. hence, the remaining simulations will be setup with 4000 particles, which is double the amount of particles initially considered.

6.3.2 Changing surface affinity in liquids

In the centre region, for the system shown in Figure 6.2b, the density is as expected for a LJ liquid (0.85$\pm$0.006 $\rho\sigma^3$) which is consistent with the parameterisation of the system. In the interface region, however, the density fluctuates and deviates from this

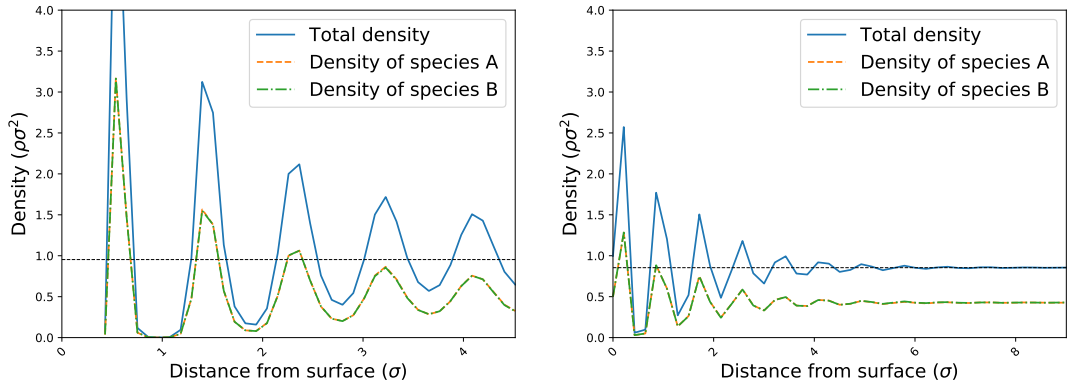

(a) (b)

Figure 6.2: Liquid density profiles. Density as a function of distance from surface with LJ interaction between surface and species A monomers for (a) a liquid precursor mixture with 2000 particles and (b) a liquid precursor mixture with 4000 particles. The dashed lines represent the average density for the selected centre region of each system. Density for the system with 2000 particles is of REVIEW and for the system with 4000 particles is of 0.85$\pm$0.006 $\rho\sigma^3$. The later closely matches expected values from literature [6].

expected value, further confirming that the surface affects liquid density. Despite this, the periodicity of the fluctuations is consistent with what is expected based on the radial distribution functions for LJ liquids [6].

The behaviour between surface and liquid was changed by increasing the value of the surface-particle A interactions to ϵ=2.0, making this interaction twice as strong as surface-particle B interactions, resulting in the almost complete density profile shown in Figure 6.3. The most noticeable occurrence is the depletion of monomer B particles from the liquid layer immediately adjacent to the surface, while monomer A particles aggregate in that region.

In addition, the opposite effect is verified in the centre region, which contains greater numbers of monomer B particles. This is due to the affinity between surface and monomer A particles being sufficient, since monomer A particles have lower energy at the surface than monomer B particles. Species A particles are able to push species B particles, that are near the surface, away from it. The displaced particles move to the centre of the film, increasing their relative density in that region.

Despite this, the density profile remains similar to the one shown previously in Fig-

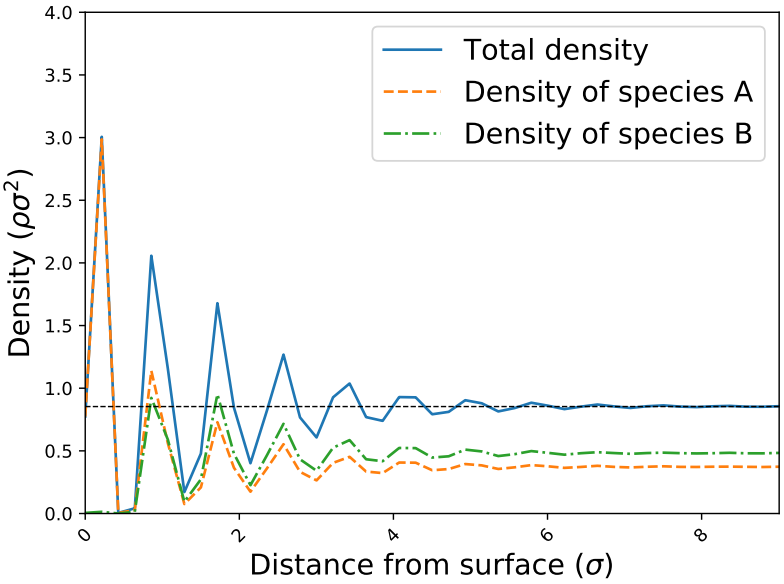

Figure 6.3: Density as a function of distance from surface with LJ interaction between surface and species A monomers for a crosslinking mixtures with 2.0ϵ.

ure 6.2b, and density in the centre of the film is also comparable (0.85$\pm$0.008 $\rho\sigma^3$) with the expected bulk density. In addition, both these profiles serve as a direct comparison with density profiles from crosslinked systems.

6.3.3 Comparison of crosslinking in bulk and confined systems

In this section, crosslinking in a bulk system is compared with a confined system. To enable a direct comparison, all particle interactions are identical for both systems, with ϵ=1.0. Both systems have equal amounts of monomer A and monomer B particles, and results are relevant for systems that share this stoichiometry.

A system containing a slab with type A and type B monomers capable of reacting with the oposite type, was setup with identical parameters to the final bulk system developed in chapter 5, and the extent of reaction for both was compared, in Figure 6.4. Given sufficient time, one would expect the extent of reaction for any crosslinking reaction to reach 1.00, however after a total of 2500τ the final value achieved for the surface system was of 0.925$\pm$0.004%, while the value for the bulk system was of 0.954$\pm$0.002%, meaning that the presence of the surface caused a decrease on the

number of bonds formed in the network.

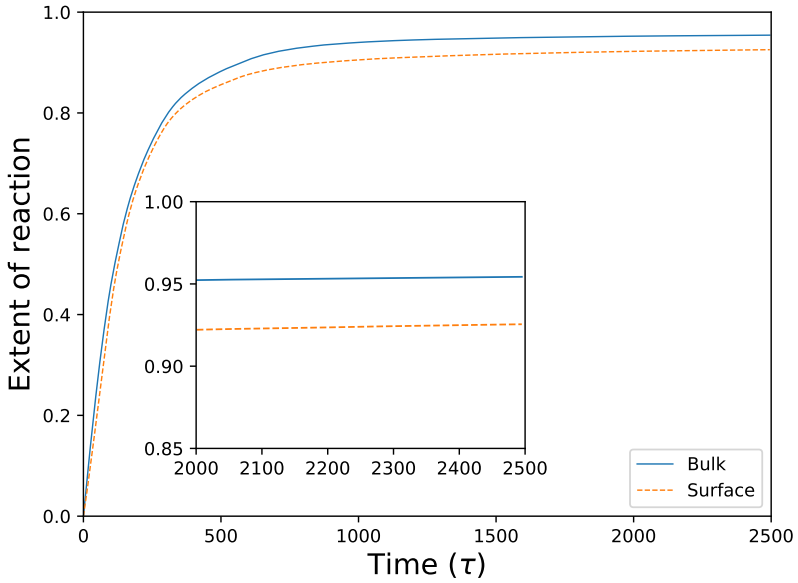

Figure 6.4: Evolution of the extent of reaction with simulation time for the bulk and surface systems. The inset plot shows more clearly that the extent of reaction has plateaued by the end of the simulations, and shows the different extent of reaction values.

From Figure 6.4 it is noticeable that crosslinking occurs slightly faster in the bulk system than in the confined system where a surface is present. The confined system has high density areas at the interface region, where particles are more tightly packed, hence molecular displacement is more limited. The closer proximity between particles in high density areas could lead to faster bonding, since potential bonding partners are closer together. However, this regions also have greater steric effects which limit particle movement, which can slow down crosslinking by preventing compatible bonding partners to encounter each other. This interplay between density and slower dynamics results in an overall slower crosslinking in the surface system.

In addition, as the system crosslinks, average polymer length increases, further limiting diffusion as larger molecules, with free reactive sites, move slower. The average polymer length, at the end of both simulations, was of 22 units to 13 units from the bulk to the surface system. These values seem counter-intuitive at first, since the bulk system achieved higher extent of reaction and higher average polymer

length at the same time. However, most particles reacted in the initial stages of reaction, as depicted by the steep curves on Figure 6.4. This seems to suggest that the absence of high density regions, in the beginning of the reaction, is the dominant factor in determining the highest possible extent of reaction achievable. As the crosslinked network grows, it becomes more and more rigid, and density increases as the network solidifies, as shown by the density profile in Figure 6.5. The density of this crosslinked network in the centre region is of $0.99 \pm 0.02 \rho\sigma^2$, which is higher than that of the pre-crosslinked liquid mixture, which is consistent with the density increase when crosslinking occurs.

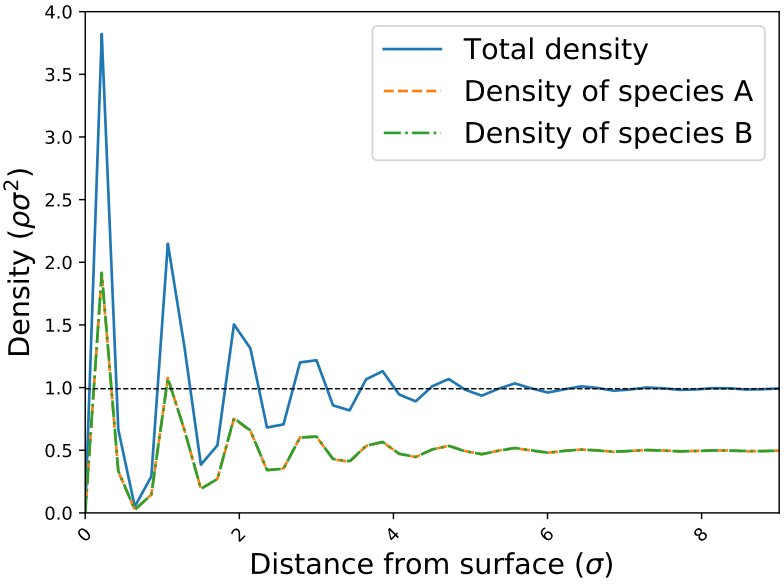

Figure 6.5: Crosslinked density profile. Density as a function of distance form the surface with all surface-liquid and liquid-liquid interactions identical, with ϵ=1.0.

Free roaming particles, which have failed to bond, have their movement impeded by the rigid network, and this effect becomes dominant in the later stages of the reaction, depicted by the plateauing of the extent of reaction, preventing further bonding.

The extent of reaction can also be related to the polymer length distribution by means of the Flory equation discussed in chapter 5, shown here again for reference:

$$N_X = N_0(1-p)^2 p^{X-1} \tag{6.1}$$

where N_X is the polymer length distribution, p is the final extent of reaction, and N_0 is the initial number of monomers in the system. The original distribution for the bulk system is presented in Figure 6.6a while the newly produced distribution for the surface system is shown in Figure 6.6b. First, Flory's predicted curve, presented by the black dashed line, for the surface system, considering its monomer count and final extent of reaction, matches the distribution obtained by the simulation, indicating that the addition of the surface to the system does not produce significant impact regarding the model developed in Chapter 5. However, the distributions differ significantly between bulk and surface systems, attesting to the impact that the addition of a surface has on the structure of the crosslinked network.

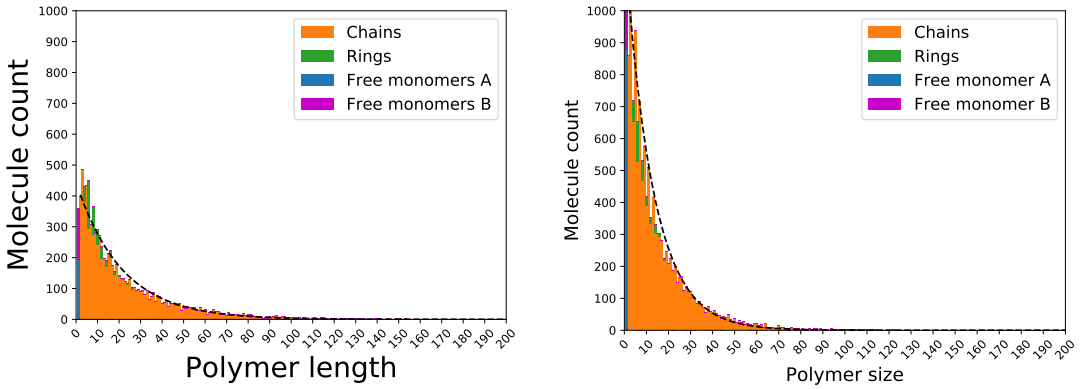

(a) (b)

Figure 6.6: Polymer length distribution for (a) bulk, and (b) surface systems at the end of simulation, totalling 2500τ. Dashed lines are the Flory predicted distributions based on simulation final extent of reaction.

6.3.4 Surface affinity in crosslinked polymers

As discussed previously in this chapter, different molecules have different degrees of molecular attraction towards other molecular species based on their chemistry, and, intuitively, this behaviour also applies to molecular surfaces. If two different monomer species, belonging to a pre-polymer mixture, have different degrees of attraction towards a specific surface, that will have an impact on the resulting polymer network, and its properties.

This effect on the crosslinked polymer network was studied, by increasing the LJ interactions between the surface and species A monomers, incrementally, while all other LJ interactions were kept unchanged. In this case the value of the surface-monomer B interactions is kept constant at 1.0ϵ while the value of the surface monomer A interactions is initially 1.0ϵ, but is increased to 2.0ϵ in 0.2ϵ increments. The outcome is a total of six simulations where the only variable changed is the surface-monomer A strength.

Time-dependency of the extent of reaction

The extent of reaction for the six simulations is plotted against time in Figure 6.7. In this figure, it is noticeable that they follow a similar behaviour. There is a steep increase in the value of the extent of reaction during the early stages of the reaction, which is followed by a monotonically decreasing gradient, at which the extent of reaction plateaus, and its increase with time becomes much slower.

In addition, a trend is also exhibited that shows that each polymer network plateaued at a different extent of reaction value depending on the attraction between surface and species A monomers. The greater the interaction between the two was, the lower the achieved extent of reaction was, in the same simulation time.

The fact that the overall shape of all the plots in Figure 6.7 is similar suggests that the type of polymerisation mechanism is unaffected by the change in particle interactions. However, there is significant difference between the final extent of reaction values achieved with the same simulation time, which points towards a different structure of the final polymer network, which is related with the inaccessibility of some bonding sides caused by stoichiometric imbalance present in the interface region.

When the interactions between surface and all particles in the system are identical, the final achieved extent of reaction is equal to 0.962 ± 0.003. A slight increase in the attraction, to 1.2ϵ, of species A monomers lowers this value to 0.959 ± 0.002. While these two values are very similar, they still fall outside each others standard deviations, which means that they are statistically different. Further increasing the attraction of species A monomers with the surface lowers the final extent of reaction value down

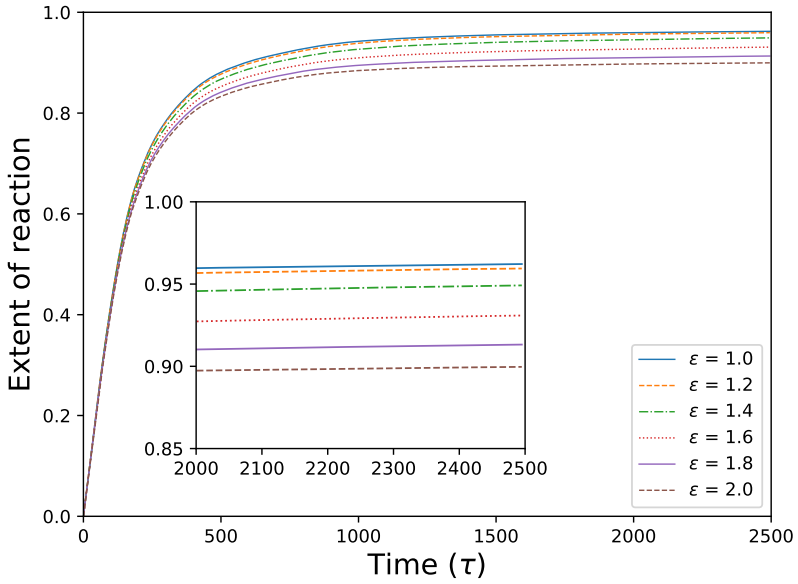

Figure 6.7: Evolution of the extent of reaction with simulation time for six different systems with varying interactions between surface particles and particles of monomer species A. The inset plot shows more clearly that the extent of reaction has stabilized by the end of the simulations and shows thee different extent of reaction values.

to 0.949$\pm$0.004, 0.931$\pm$0.005, 0.913$\pm$0.004, and 0.900$\pm$0.005, respectively, for 1.4ϵ, 1.6ϵ, 1.8ϵ, and 2.0ϵ.

The correlation between the strength of the LJ interactions and the extent of reaction is attributed to the fact that monomers with higher surface attraction will tend to adsorb to the surface, creating a layer composed of a single monomer species prior to crosslinking. This creates a region where there exists an over-abundance of a single monomer species, which deprives monomers in it of potential bonding partners, lowering the achievable extent of reaction. However, a structural analysis, performed in section 6.3.4, is required to verify this hypothesis. This can be achieved by analysing the density profiles along the z-axis of the simulation box, and quantifying the amount of each monomer species as a function of their distance to the surface.

Polymer length distribution

Considering the model developed in the previous chapter was aimed at generating a crosslinked polymer network that is comparable to Flory's theory of polymerisation for

linear polymers, it is also important to study the effect that changing the interactions between surface and one of the monomer species has on the crosslinked polymer network structure. This is done by analysing the polymer length distribution at the end of reaction.

The polymer length distributions for each of the six simulations are shown in the histograms presented in Figure 6.8. Each histogram is accompanied by their respective number distribution curve according to Flory's. All six show great agreement with the theoretical curve, meaning that changing the interactions between two monomer types in the system does not affect the ability of the developed model to generate a crosslinked polymer network in agreement with Flory's polymer theory.

The second aspect revealed by the shape of these distributions is that as the interactions between surface and species A monomers increases, so does the distribution favours the formation of polymers of smaller lengths. This is in agreement with the analysis performed on the extent of reaction for each of these simulations which showed that the achieved extent of reaction decreased as the interactions between surface and one monomer species increased.

Surface effect on density

The six plots presented in Figure 6.9 show the density profiles for all six simulations after crosslinking takes place. Despite the change in particle interactions, the density profiles of all six systems share some common similarities with each other. Looking at total density, it is very similar for all systems and, without discriminating between different monomer species, two separate regions can be identified: the interface region, which has density oscillations; and the centre of the film region, where density remains stable. The separation between these two regions is located at 5σ from the surface.

At the centre of the film, density averages at $0.99\rho\sigma^2$ across all systems, which is is in agreement with the density achieved in the previous bulk simulation, suggesting that behaviour in this region is bulk-like. At the interface, the increased density peaks are consistent with the location of layers, as expected, due to the LJ parameters, since

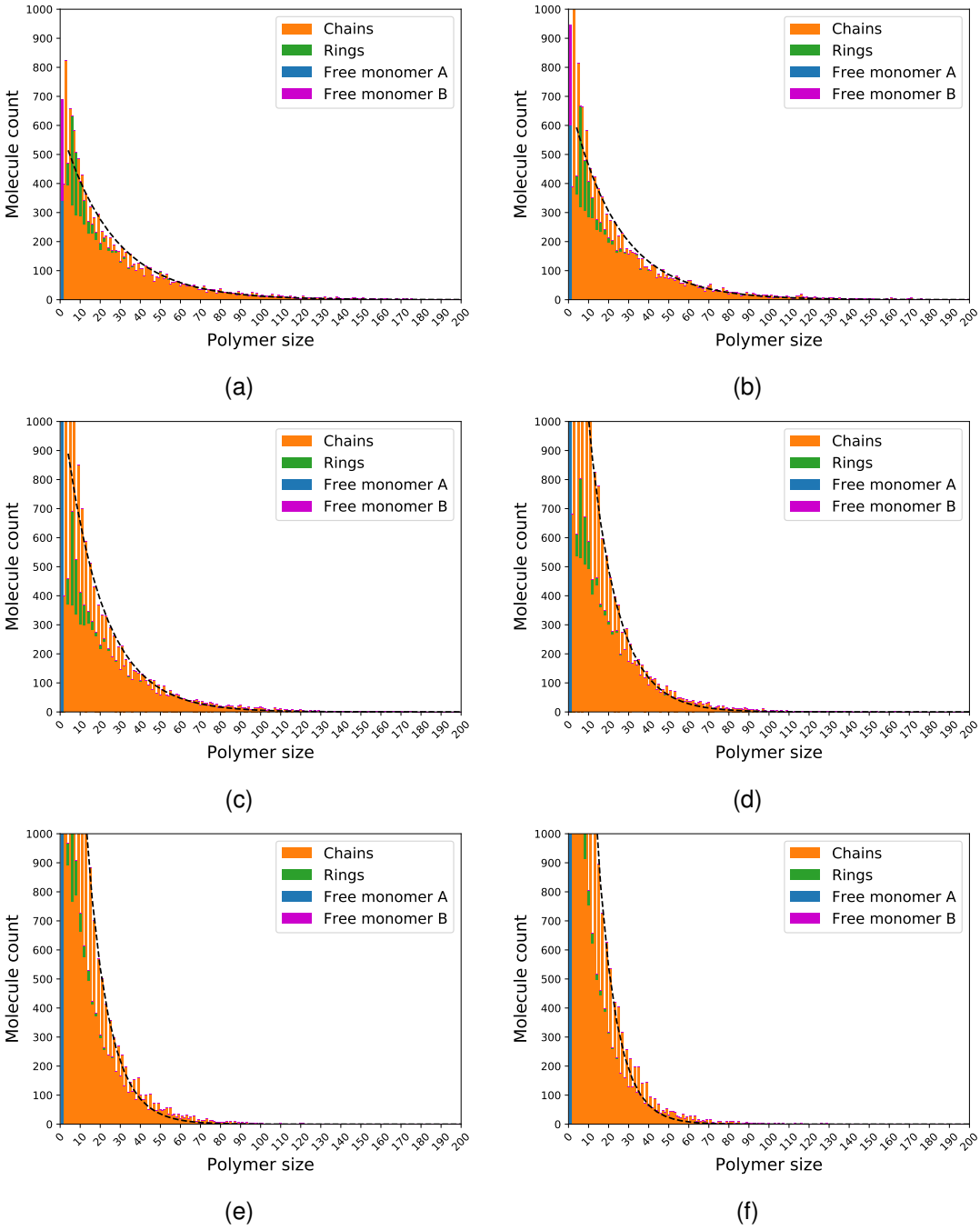

Figure 6.8: Polymer length distribution with LJ interaction between surface and species A monomers equal to (a) 1.0 ϵ; (b) 1.2 ϵ; (c) 1.4 ϵ; (d) 1.6 ϵ; (e) 1.8 ϵ: (f) 2.0 ϵ. The dashed lines are the Flory predicted distributions based on simulation final extent of reaction.

the distance between peaks roughly corresponds to LJ equilibrium distance between monomers.

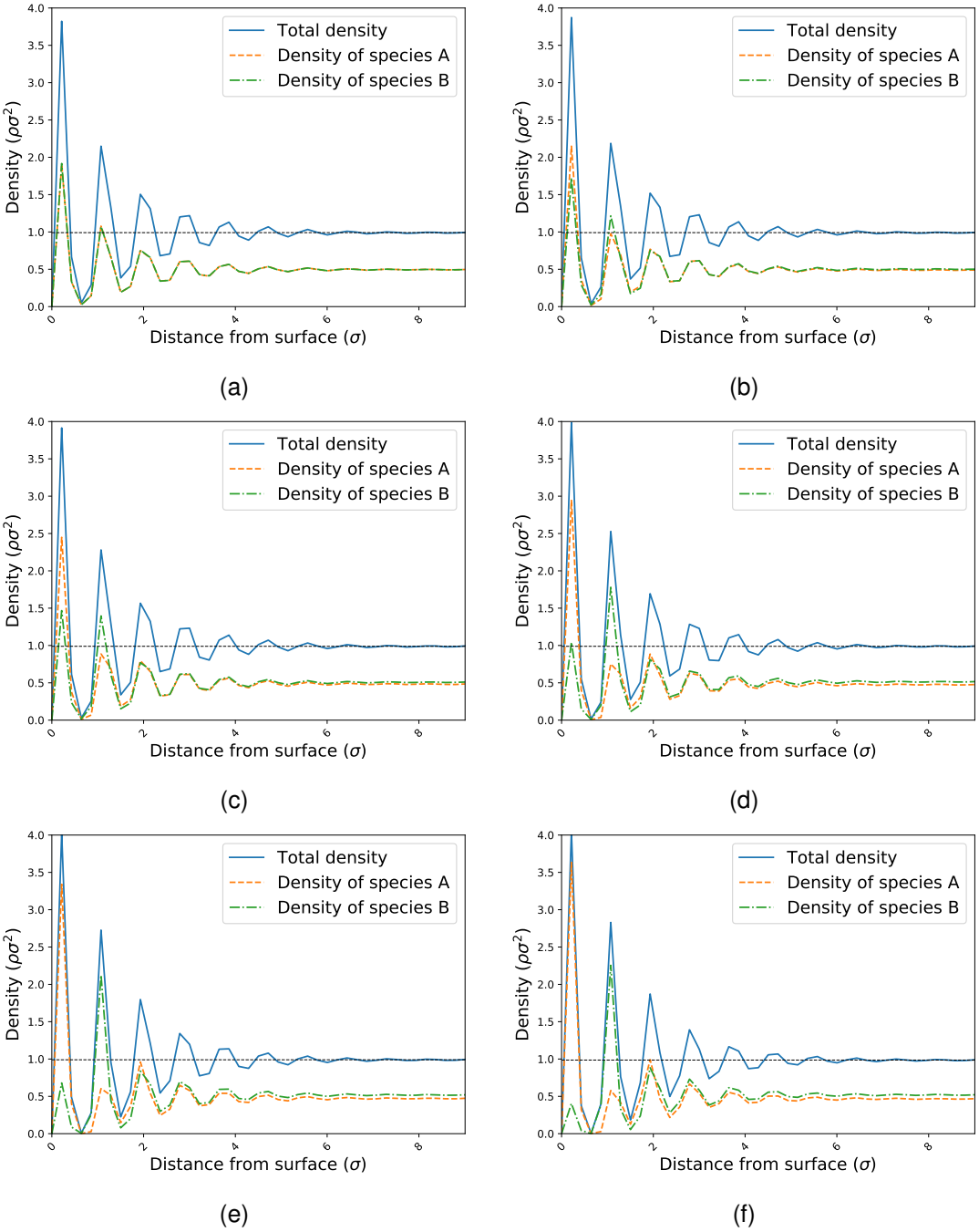

Figure 6.9: Density as a function of distance from surface with LJ interaction between surface and species A monomers equal to (a) 1.0ϵ; (b) 1.2ϵ; (c) 1.4ϵ; (d) 1.6ϵ; (e) 1.8ϵ; (f) 2.0ϵ.

The plot in Figure 6.9a relates to the first simulation, where all interactions are identical. The two dashed lines show the density contribution of each monomer species to overall density. In the case where surface interactions are equal for both monomer species, these two species maintain an even ratio between them over the entire simulation box, and independently from distance to the surface. This behaviour is expected when all LJ interactions are identical, making it so that no monomer species has a preference for adsorbing to the surface. Because of this, this system serves as a baseline for comparison with all other subsequent simulations, where those interactions differ.

In figure 6.9b, the interactions between the surface and species A monomers is made slightly stronger than the rest of the interactions. This results in a slight excess of species A monomers being adsorbed to the surface, shifting the molecular ratio between both monomer species in favour of species A, in the first layer, adjacent to the surface. This excess caused a depletion of species A monomers in other regions of the simulation box, that seems to be exclusively from the second layer.

The plots in Figures 6.9c to Figures 6.9f show that this behaviour becomes more prominent when the interactions between surface and species A monomers monomers is increased, which was to be expected. However, starting at 1.4ϵ, the excess of species A monomers at the surface causes not only a depletion of the same monomer in the second layer, but also in every other region of the simulation box, including the centre of the film, where bulk-like behaviour was exhibited. Despite this, the total density at the centre of the film remains unaffected, meaning that the presence of species B monomers compensates for this depletion.

These results point towards the fact that, if the affinity between a particular monomer species and the surface is much greater than the other monomer species in the same pre-polymer mixture, its adsorption can have an impact on the nature of a crosslinked network, that propagates far away from the surface.

I showed before that the final extent of reaction is lower when the interactions between the surface and one of the monomer species is greater than with the other. The density profiles provide insight into why that correlation exists. Since, in this model, monomer species can only bond with different monomer species, if regions exist that

are mostly composed of a single monomer species, then monomers in that region have limited bonding partners available to them.

To get even more insight into this effect, the total number of non-bonded monomers of both species in the first and second layers were quantified, relative to the total amount of non-bonded monomers. These results are presented in Table 6.1 for every simulation.

Table 6.1: Fraction of non-bonded monomers in the first, and second layers relative to the strength of the interaction between surface and species A monomers. Total number of monomers in simulations is 400,000. A value of zero implicates the full absence of a monomer particle in that region.

Simulation	Free A	1^{st} layer A	2^{nd} layer A	Free B	1^{st} layer B	2^{nd} layer B	Total
1.0 ϵ	0.09	0.01	0.01	0.09	0.01	0.01	0.18
1.2 ϵ	0.15	0.06	0.02	0.09	0	0.01	0.24
1.4 ϵ	0.38	0.28	0.03	0.15	0	0.01	0.53
1.6 ϵ	0.78	0.65	0.01	0.28	0	0.01	1.06
1.8 ϵ	1.15	1.12	0.01	0.41	0	0.01	1.56
2.0 ϵ	1.52	1.50	0.00	0.54	0	0.02	2.06

The stronger the interactions between the surface and species A monomers, the more non-bonded monomers of its type are present in the first layer, and the less of species B monomers there are. However, the excess species B monomers in the second layer are still mostly reacted, even when interactions become greater between surface and species A monomers, despite existing in over-abundance in that layer. One potential hypothesis for this behaviour is due to the abundance of bonding partners present in the first, and adjacent, layer. This would also imply that most bonds in this region would be perpendicular to the surface, with polymer molecules stretching from the surface towards the centre of the film.

Intuitively, one would expect the species B monomers in the second layer to be mostly non-bonded to balance the vast amount of non-bonded species A monomers in the first layer, however that was not the case. To understand where, relative to the surface, the non-bonded species B monomers are, I looked at the simulation where the interactions between surface and species A monomers were greater, since this behaviour was more evident. A layer-by-layer count of all non-bonded monomers was

performed, which is shown in table 6.2, and shows that most non-bonded species B monomers reside in the centre film region of the system.

These results indicate that when the two monomers of a binary pre-polymer mixture, have very distinct affinities with the surface, the extent of reaction becomes limited by the non-bonded monomers in the first layer adjacent to the surface, and the non-bonded monomers in the centre of the film, farther away from the surface. In addition, the dominant non-bonded species in these two regions is different, and is dependent on their interactions with the surface.

Table 6.2: Number of non-bonded monomers in all layers, and centre of the film, for ϵ=2.0.

Layer	Species A	Species B
1 $^{\mathrm{st}}$	6015	0
2 $^{\mathrm{nd}}$	16	64
3 $^{\mathrm{rd}}$	6	283
4 $^{\mathrm{th}}$	5	316
5 $^{\mathrm{th}}$	7	281
Centre	20	1201
Total	6069	2145

Bond orientation

I postulated earlier that, at the interface region, the dominant orientation of the bonds was perpendicular to the surface given that the majority of the second layer was shown to be mostly composed of reacted monomers, while the first layer contained the vast majority of non-bonded species A monomers. This assumption is also made on the basis that inter-layer distance is consistent with the expected 1.122σ bond length, based on simulation parameters. This effect was also shown to be greater in simulations where the interaction between species A monomers and the surface was proportionally greater than the interaction between species B monomers and the surface. To validate this hypothesis, a bond orientation analysis was performed.

This was done by isolating all the bonds that existed up to a maximum distance of 1.5σ from the surface, which includes only monomers from the first two layers. The

orientation vectors for all bonds inside this region were calculated, and the angles they formed with the surface were measured. An angle of 90^{o} corresponds to a perpendicular orientation between bond and surface, while angles of 0^{o} or 180^{o} correspond to a parallel orientation.

Table 6.3: Mean angles between surface and bonds, up to 1.5σ from the surface, for all simulations. A value of 90^{o} would correspond to a perpendicular angle with the surface.

Simulation	Mean angle (^{o})	Standard deviation (^{o})
1.0ϵ	79.73	10
1.2ϵ	80.15	9
1.4ϵ	80.44	9
1.6ϵ	80.86	8
1.8ϵ	80.84	9
2.0ϵ	80.89	9

Table 6.3 shows the average angle value, formed between molecular bonds and the surface, alongside its respective standard deviations for every simulation. Table 6.3 shows that the average angle is slightly greater when the interaction between monomer species A and the surface is also greater. However, the standard deviation values place all these values within range of each other, so any variations of the bond orientation are minor. Despite of this, the preferred bond orientation near the surface tends to be almost perpendicular in the first polymer layer, and this effect is more prevalent when the interaction between surface and one monomer species is higher. This behaviour is consistent with the hypothesis that species B monomers in the second layer are mostly bonded with species A monomers in the first layer, making polymer bonds that stretch outwards from the surface into the centre film.

6.4 Conclusions

The introduction of a surface into a binary mixture prior to crosslinking showed an evident reduction on the extent of reaction, as well as a decrease in the average polymer length, in terms of monomer units. This effect is sufficient to be statistically relevant, meaning that the presence of the surface is sufficient to affect the structure of the

crosslinked network. However, distribution plots for the surface system are still in full agreement with Flory's, further attesting to the robustness of my crosslink model developed in Chapter 5.

Liquid simulations with a surface, and varying degrees of affinity between one particular molecular species and the surface, showed that when this affinity is increased, the molecular chemical species in question will attempt to adsorb to the surface. In doing so, other molecular species are displaced from the interface region, and move towards the centre film region. This causes an inbalance in the sterochemical proportions of both species along the simulation box, which has repercussions in the structure of the crosslinked network.

The impact of changing the affinity between a single molecular species and the surface was shown to affect the structure of the crosslinked networks, after curing. When the ratio between the interaction strengths of both species to the surface was greater, the lower the final extent of reaction achieved under the same simulation time was. When the affinity of one of the species is much larger than the other, that species fully adsorbs to the surface, fully blocking it from other species in the system. This adsorbed layer, being mostly composed of a single species, has limited reaction capability since it exists in excess near the surface. The few bonds that are able to be formed in this region are perpendicular to the surface and propagate away from it. however, the large amount of unreacted particles in this region, in proportion, to the rest of the system, prevents the network from fully developing, affecting its properties.

7. Conclusion and Outlook

The aim of this thesis work is to investigate how a carbon fibre surface affects the properties of epoxy composites. Typically, epoxy liquid mixture components are mixed with fibres and then cured. It is hypothesised that the liquid structure of the epoxy liquid mixture differs near the carbon fibre surface because of the different degrees of molecular attraction that each molecular species has with the surface. An excess of a molecular species at the surface can cause a stoichiometric imbalance that disrupts the optimal molecular ratios to achieve a fully cured material. Molecular simulations methods were utilised to investigate this effect by studying the interface region in composite materials, which is difficult to study experimental given its small scale. In addition, this effect was studied with recourse to an epoxy-based model system as well as a generic polymer model.

First the structure of an epoxy liquid mixture near a graphene surface was investigated. It was found that a stoichiometric imbalance between both molecular species existed and that and excess of EPON-862 was present near the surface while away from it the opposite occurred and an excess of DDS existed. This imbalance can lead to less extensive crosslinked network being formed in the interface. In addition, molecular orientation relative to the surface was also found to be different at the interface, with molecules preferring to lay flat on the graphene surface, further limiting bonding between EPON-862 and DDS molecules.

To investigate the crosslinking, a generic model was developed, based on the LJ model, that could simulate the polymerisation process at a surface. The model included an angle restriction parameter which allowed simulations to yield more realistic crosslinked network structures for binary polymers. Polymer structures obtained via this model were bench-marked against theoretical prediction done with Flory's polymer growth theory for linear polymers, and proved to be in good agreement with it.

This model was the used to model polymerisation at a surface. It was found that the stoichiomeric imbalance between molecular species observed in the epoxy simu-

lations was also present and that it did affect polymerisation in the interface. When one molecular species was observed to be more attracted to the surface than the other, it caused the excess present in the first layer adjacent to the surface to remain mostly unbonded. The excess of the less attracted species was mostly verified on the second layer of the interface and was observed to be fully bonded, unlike the excess of the most attracted species in the first layer. further verification showed that this occurred because most of the bonds formed were perpendicular to the surface.

These findings show that the liquid structure of the pre-polymer mixtures, which is an often overlooked factor, does play an important role in determining the structure and maximum achievable extent of reaction of cured carbon fibre reinforced polymer composites. The molecular ratio between molecular species can be adequately adjusted by predicting which molecule is more closely attracted to the surface to maximise the changes of a fully cured material. In addition, the model developed for crosslinking of generic polymer models offers an streamlined way of predicting the stoichiometry, as a function of distance from the surface, based on know molecular interactions between chemical species.

This work focused mainly on studying the structural properties of epoxy mixtures, however dynamic properties such as mean squared displacement could also be investigated further by performing larger simulations than the ones used in the work. It would also be interesting to be able to directly apply the developed crosslinking model to an EPON-862/DETDA system and investigate if results obtained via generic bead-spring models are accurately represent more chemical-significant systems.

In addition, the bead-spring model developed and used in this work was only used to investigate linear chain formation, as a means of establishing a benchmark and retrieve some initial results. It is natural that further work would expand upon this and makes use of this model to study systems with increased degrees of complexity, such as systems with more than two particle types. The presence of additive or catalyst molecules and its effect on crosslinking could also be studied by introducing more monomer species with varying degrees of size and complexity, as well as different interactions with baseline monomer species.

One more noteworthy question of research concerns to the improvement and further validation of the model developed in this work. In this work, bead-spring simulations were performed in batches, each containing 100 instances of a similar system with a different starting configuration. The reason behind this experiment design was, as was already mentioned in chapter 6, due to computational limitations of the current model implementation in LAMMPS. By updating the model to be able to run in parallel, the work on chapter 6 could be replicated using a single large simulation instead.

A. Appendix

A.1 Force fields models for EPON-862, DETDA and DDS

A.1.1 OPLS-AA and OPLS-UA models

The OPLS-AA force field is a fully atomistic model that treats all atoms explicitly, whereas the OPLS-UA force field treats the alkyl and aryl hydrogen atoms and their bonded carbons as single united atoms. The OPLS-AA and OPLS-UA force fields use the harmonic potential to describe the bond stretch between two atoms and the angle bend between three atoms. The harmonic bond stretch energy, $E_b(r)$, is given by

$$E_b(r) = \frac{1}{2}K_r(r - r_0)^2 = k_r(r - r_0)^2 \tag{A.1}$$

where r is the distance between atoms, r_0 is the equilibrium distance, and $k_r = \frac{1}{2}K_r$, where K_r is the bond force constant. Similarly, the harmonic angle energy, $E_a(\theta)$, is of the form

$$E_a(\theta) = \frac{1}{2}K_\theta(\theta - \theta_0)^2 = k_\theta(\theta - \theta_0)^2 \tag{A.2}$$

where θ is the angle between the three atoms, θ_0 is the equilibrium angle, and $k_\theta = \frac{1}{2}K_\theta$, where K_θ is the angle force constant. Dihedrals are described using the Fourier form

$$E_d(\phi) = \sum_{i=1}^{3} \frac{1}{2}k_i[1 + \cos(i\phi)] \tag{A.3}$$

where ϕ is the dihedral angle and the k_i coefficients give the dihedral strength. Non-bonded van der Waals interactions are described by the Lennard-Jones (LJ) potential

$$E_{\mathrm{LJ}}(r) = 4\epsilon\left[\left(\frac{\sigma}{r}\right)^{12} - \left(\frac{\sigma}{r}\right)^{6}\right] \tag{A.4}$$

where r is the distance between two atoms, σ is the distance when E_{LJ} equals zero, and ϵ is the depth of the minimum. The cutoff for the LJ potential is set at 10 Å for

OPLS force fields. Arithmetic mixing rules are used. Electrostatic interactions are described using the Coulomb potential

$$E_{coul} = \frac{q_i q_j}{4\pi\epsilon_r r} = \frac{C q_i q_j}{\epsilon_r r} \tag{A.5}$$

where C is the energy-conversion constant, q_i and q_j are the charges on atoms i and j and ϵ_r is the dielectric constant. The cutoff for the direct computation of the electrostatic interactions is at 8 Å.

For EPON-862, DETDA and DDS, the OPLS-AA and OPLS-UA parameters were taken from Jorgensen *et al.* [59].

OPLS-AA parameters for EPON-862

The atom labels for the EPON-862 molecule as described by the OPLS-AA force field are shown in Figure A.1.

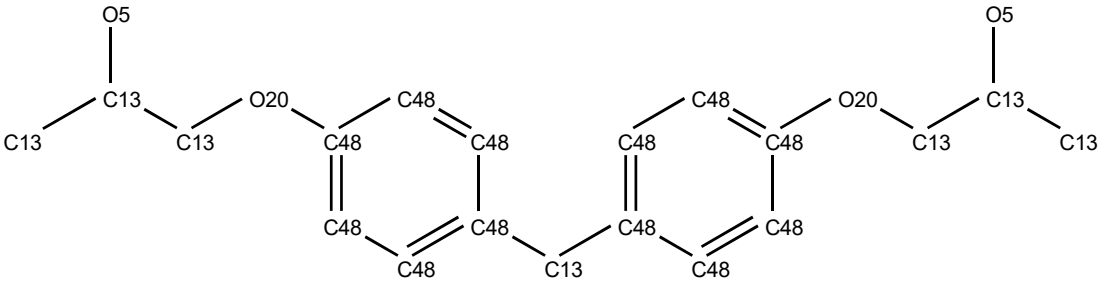

Figure A.1: EPON-862 atom labels for OPLS-AA force field. Hydrogen atoms are omitted for clarity: aliphatic, aromatic and hydroxyl hydrogens have designations "H49", "H46" and "H7" respectively.

The OPLS-AA bond parameters for EPON-862 are shown in Table A.1. The OPLS-AA angle parameters for EPON-862 are shown in Table A.2. The OPLS-AA dihedral parameters for EPON-862 are shown in Table A.3. The OPLS-AA LJ parameters for EPON-862 are shown in Table A.4. The OPLS-AA partial charges for EPON-862 are shown in Figure A.2.

Table A.1: OPLS-AA bond parameters for EPON-862.

Bonds		
Description	k_r (kcal Å^{-2})	r_0 (Å)
C13-H46	340	1.09
C13-C13	268	1.53
C13-O5	320	1.41
O5-H7	551	0.95
C13-O20	320	1.41
O20-C48	450	1.36
C48-C48	469	1.40
C48-H49	367	1.08
C48-C13	317	1.51

Table A.2: OPLS-AA angle parameters for EPON-862.

Angles		
Description	k_θ (kcal rad^{-2})	θ_0 ($^{\circ}$)
C13-C13-C13	58.4	112.7
C13-C13-H46	37.5	110.7
C13-C13-O20	50.0	109.5
H46-C13-O20	35.0	109.5
C13-C48-C48	70.0	120.0
C13-O20-C48	75.0	111.0
C13-O5-H7	55.0	108.5
C48-C13-C48	40.0	109.5
C48-C13-H46	35.0	109.5
C48-C48-C48	63.0	120.0
C48-C48-H49	35.0	120.0
C48-C48-O20	70.0	120.0
H46-C13-H46	33.0	107.8

Table A.3: OPLS-AA dihedral parameters for EPON-862.

Dihedrals			
Type	k_1 (kcal rad^{-2})	k_2 (kcal rad^{-2})	k_3 (kcal rad^{-2})
C13-C13-C13-H46	0	0	0.30
C13-C13-C13-O20	1.3	-0.05	0.20
C13-C13-O20-C48	0.65	-0.25	0.67
C13-C13-O20-C13	0.65	-0.25	0.67
C13-C13-O5-H7	-0.36	-0.17	0.49
C13-C48-C48-C48	0	7.3	0
C48-C13-C48-C48	0	0	0
C48-C48-O20-C13	0	3.0	0
H46-C13-C13-O20	0	0	0.47
H46-C13-O20-C48	0	0	0.76
H46-C13-O5-H7	0	0	0.35
O20-C13-C13-O5	4.3	0	0

Table A.4: OPLS-AA LJ parameters for EPON-862.

	Lennard-Jones	
Pair	ϵ (kcal Å^{-2})	σ (Å)
C13	0.066	3.50
C48	0.070	3.55
H46	0.030	2.50
H7	0	0
H49	0.030	2.50
O5	0.170	3.12
O20	0.140	2.90

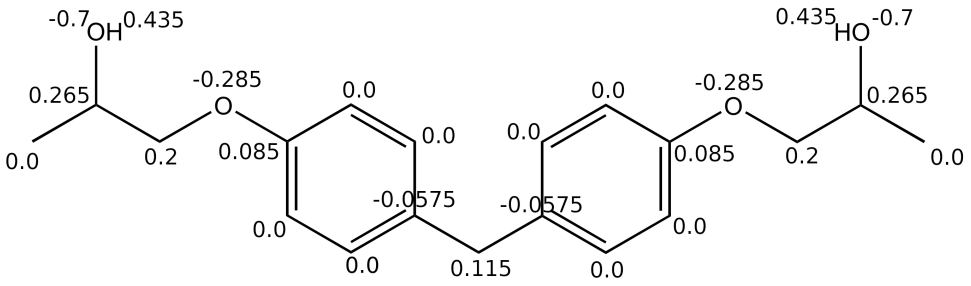

Figure A.2: OPLS-AA partial atomic charges for EPON-862.

OPLS-UA parameters for EPON-862

The atom labels for the EPON-862 molecule as described by the OPLS-UA force field is shown in Figure A.3.

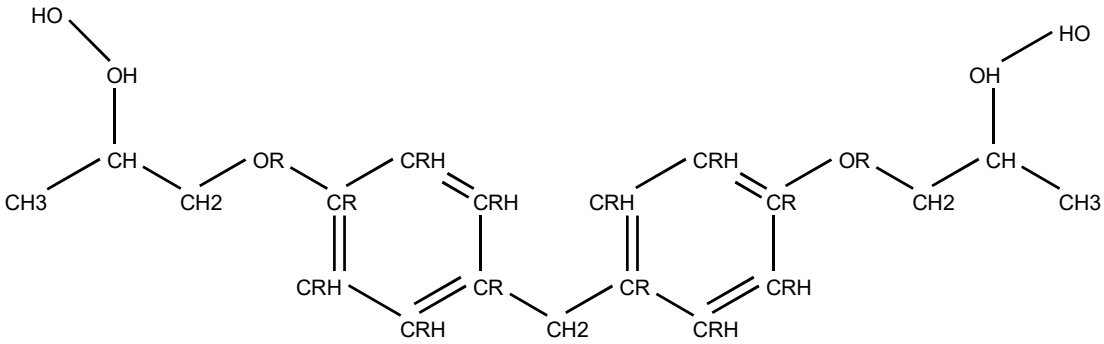

Figure A.3: EPON-862 atom labels for OPLS-UA force field.

The OPLS-UA bond parameters for EPON-862 are shown in Table A.5. The OPLS-UA angle parameters for EPON-862 are shown in Table A.6. The OPLS-UA dihedral parameters for EPON-862 are shown in Table A.7. The OPLS-UA LJ parameters for EPON-862 are shown in Table A.8. The OPLS-UA partial charges for EPON-862 are shown in Figure A.4.

Table A.5: OPLS-UA bond parameters for EPON-862. Bond constant (k_r) given in kcal/Å^2 and equilibrium distance (r_0) given in Å.

Bonds		
Description	k_r	r_0
CH3-CH	260	1.53
CH-CH2	260	1.53
CH-OH	386	1.43
OH-HO	553	0.945
CH2-OR	320	1.43
OR-CR	450	1.37
CR-CRH	469	1.40
CRH-CRH	469	1.40
CRH-CR	469	1.40
CR-CH2	317	1.51

Table A.6: OPLS-UA angle parameters for EPON-862. Spring constant (k_θ) given in kcal/rad^2 and equilibrium distance (θ_0) given in degrees.

Angles		
Description	k_θ	θ_0
CR-OR-CH2	100	111.8
CR-CRH-CRH	85.0	120.0
CR-CR-CR	40.0	109.5
HO-OH-CH	55.0	108.5
OH-CH-CH3	80.0	109.5
OH-CH-CH2	80.0	109.5
OR-CR-CRH	70.0	120.0
OR-CH2-CH	80.0	109.5
CH3-CH-CH2	63.0	112.4
CRH-CR-CRH	85.0	120.0
CRH-CR-CR	70.0	120.0

Table A.7: OPLS-UA dihedral parameters for EPON-862. Dihedral constants (k_i) given in kcal/rad^2.

Dihedrals			
Type	k_1	k_2	k_3
CR-OR-CH2-CH	0.65	-0.25	0.67
CR-CRH-CRH-CR	0	7.3	0
HO-OH-CH-CH3	0.3	0	0.50
HO-OH-CH-CH2	0.3	0	0.50
OH-CH-CH2-OR	4.3	0	0
OR-CR-CRH-CRH	0	7.3	0
CH3-CH-CH2-OR	1.7	-0.5	0.66
CRH-CR-OR-CH2	0	3.0	0
CRH-CR-CRH-CRH	0	7.3	0
CRH-CR-CR-CR	0	0	0
CRH-CRH-CR-CR	0	7.3	0

Table A.8: OPLS-UA van der Waals parameters for EPON-862. LJ equilibrium energy (ϵ) and distance at zero energy (σ) given in kcal/Å^2.

	Lennard-Jones	
Pair	ϵ	σ
CH3	0.207	3.78
CH, CH2	0.066	3.50
CR	0.0700	3.55
CRH	0.110	3.75
CH2*	0.118	3.91
HO	0	0
OH	0.170	3.07
OR	0.140	2.90

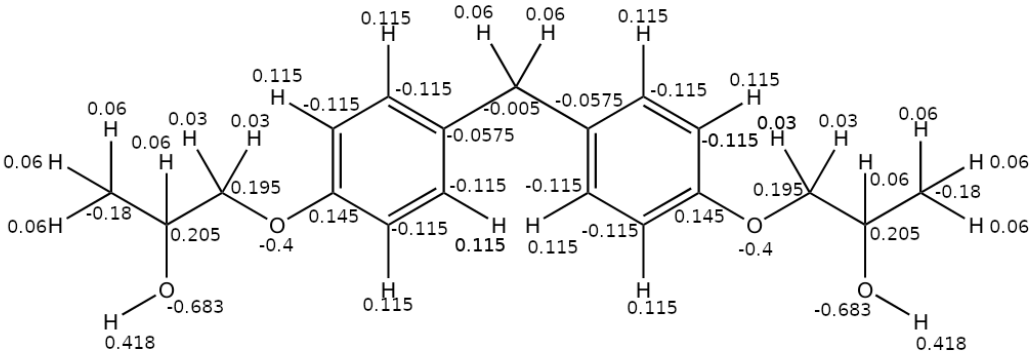

Figure A.4: OPLS-UA partial atomic charges for EPON-862.

OPLS-UA parameters for DETDA

The atom labels for the EPON-862 molecule as described by the OPLS-AA force field are shown in Figure A.5.

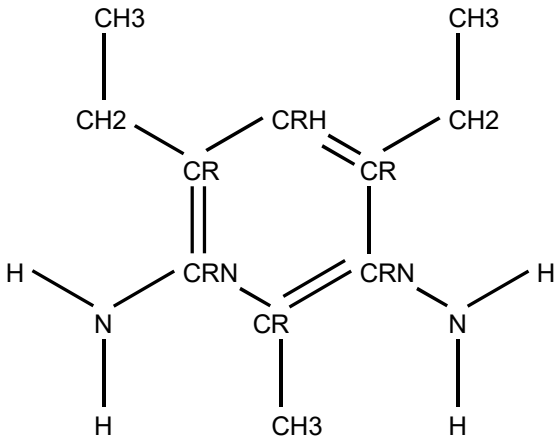

Figure A.5: DETDA atom labels for OPLS-UA force field.

The OPLS-AA bond parameters for DETDA are shown in Table A.9. The OPLS-AA angle parameters for DETDA are shown in Table A.10. The OPLS-AA dihedral parameters for DETDA are shown in Table A.11. The OPLS-AA LJ parameters for DETDA are shown in Table A.12. The OPLS-AA partial charges for DETDA are shown in Figure A.6.

Table A.9: OPLS-UA bond parameters for DETDA. Bond constant (k_r) given in kcal/Å^2 and equilibrium distance (r_0) given in Å.

Bonds		
Description	k_r	r_0
CH2-CH3	260	1.53
CH2-CR	317	1.51
CR-CRH	469	1.40
CR-CRN	469	1.40
CRN-N	481	1.34
N-H	434	1.01
CRH-CH3	317	1.51

Table A.10: OPLS-UA angle parameters for DETDA. Spring constant (k_θ) given in kcal/rad^2 and equilibrium distance (θ_0) given in degrees.

Angles		
Description	k_θ	θ_0
CH2-CR-CRH	70.0	120.0
CH2-CR-CRN	70.0	120.0
CH3-CH2-CR	63.0	114.0
CH3-CR-CRN	70.0	120.0
CR-CRH-CR	63.0	120.0
CR-CRN-CR	63.0	120.0
CR-CRN-N	70.0	120.0
CRH-CR-CRN	63.0	120.0
CRN-CR-CRN	63.0	120.0
CRN-N-H	50.0	108.6
H-N-H	43.6	106.4

Table A.11: OPLS-UA dihedral parameters for DETDA. Dihedral constants (k_i) given in kcal/rad^2.

Dihedrals			
Type	k_1	k_2	k_3
CH2-CR-CRH-CR	0	7.25	0
CH2-CR-CRN-CR	0	7.25	0
CH2-CR-CRN-N	0	7.25	0
CH3-CH2-CR-CRH	0	0	0
CH3-CH2-CR-CRN	0	0	0
CH3-CR-CRN-CR	0	7.25	0
CH3-CR-CRN-N	0	7.25	0
CR-CRN-N-H	0	2.03	0
CRH-CR-CRN-CR	0	7.25	0
CRH-CR-CRN-N	0	7.25	0
CRN-CR-CRH-CR	0	7.25	0
CRN-CR-CRN-CR	0	7.25	0
CRN-CR-CRN-N	0	7.25	0

Table A.12: OPLS-UA LJ parameters for DETDA. LJ equilibrium energy (ϵ) and distance at zero energy (σ) given in kcal/Å^2.

	Lennard-Jones	
Pair	ϵ	σ
CH2	0.175	3.91
CH3	0.118	3.91
CR	0.0500	3.80
CRH	0.145	3.96
CRN	0.070	3.55
H	0	0
N	0.170	3.30

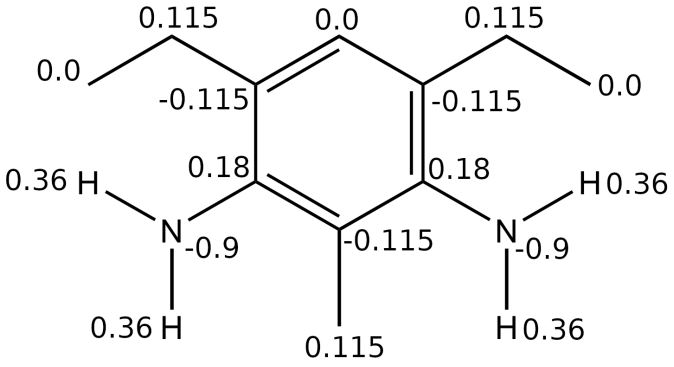

Figure A.6: OPLS-UA partial atomic charges for DETDA.

OPLS-UA parameters for DDS

The atom labels for the DDS molecule as described by the OPLS-UA force field is shown in Figure A.7.

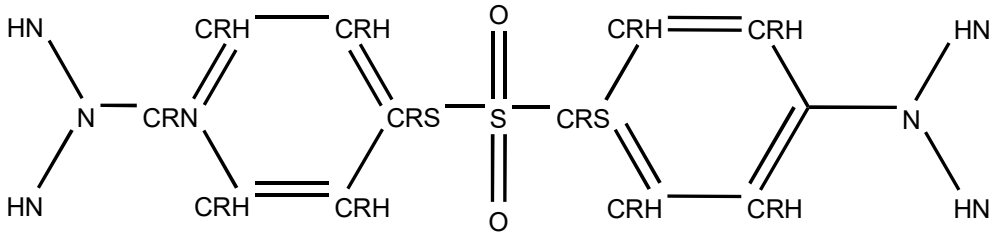

Figure A.7: DDS atom labels for OPLS-UA force field.

The OPLS-UA bond parameters for DDS are shown in Table A.13. The OPLS-UA angle parameters for DDS are shown in Table A.14. The OPLS-UA dihedral parameters for DDS are shown in Table A.15. The OPLS-UA LJ parameters for DDS are shown in Table A.16. The OPLS-UA partial charges for DDS are shown in Figure A.8.

Table A.13: OPLS-UA bond parameters for DDS. Bond constant (k_r) given in kcal/Å^2 and equilibrium distance (r_0) given in Å.

Bonds		
Description	k_r	r_0
CRH-CRH	469	1.40
CRH-CRN	469	1.40
CRH-CRS	469	1.40
CRS-S	340	1.77
CRN-N	481	1.34
N-HN	434	1.01
S-O	700	1.44

Table A.14: OPLS-UA angle parameters for DDS. Spring constant (k_θ) given in kcal/rad^2 and equilibrium distance (θ_0) given in degrees.

Angles		
Description	k_θ	θ_0
CRH-CRH-CRN	63.0	120.0
CRH-CRH-CRS	63.0	120.0
CRH-CRN-CRH	63.0	120.0
CRH-CRN-N	70.0	120.0
CRH-CRS-CRH	63.0	120.0
CRH-CRS-S	85.0	119.4
CRN-N-HN	35.0	116.0
CRS-S-CRS	85.0	119.4
CRS-S-O	74.0	107.2
HN-N-HN	43.6	106.4
O-S-O	104	119.0

Table A.15: OPLS-UA dihedral parameters for DDS. Dihedral constants (k_i) given in kcal/rad^2.

Dihedrals			
Type	k_1	k_2	k_3
CRH-CRH-CRN-CRH	0	7.25	0
CRH-CRH-CRN-N	0	7.25	0
CRH-CRH-CRS-CRH	0	7.25	0
CRH-CRH-CRS-S	0	0	0.452
CRH-CRN-N-HN	0	2.03	0
CRH-CRS-S-CRS	0	0.90	0
CRH-CRS-S-O	0	0	0
CRN-CRH-CRH-CRS	0	7.25	0

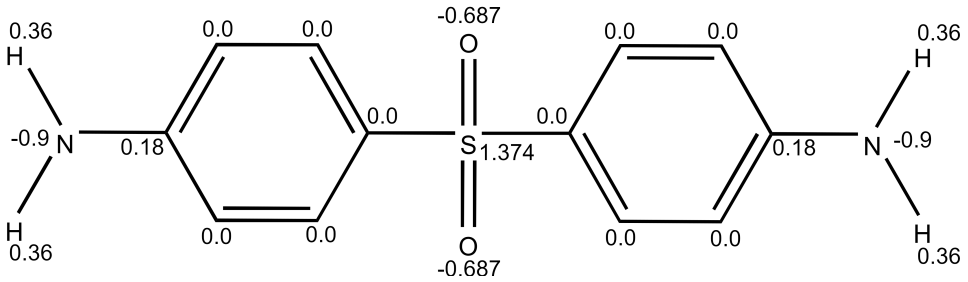

Figure A.8: OPLS-UA partial atomic charges for DDS.

Table A.16: OPLS-UA van der Waals parameters for DDS. LJ equilibrium energy (ϵ) and distance at zero energy (σ) given in kcal/Å^2.

	Lennard-Jones	
Pair	ϵ	σ
CRH	0.0700	3.55
CRN	1.07	4.55
CRS	2.07	5.55
HN	0	0
N	0.170	3.30
O	0.170	2.96
S	0.250	3.55

GraFF parameters for the graphite surface

Functional form for GraFF carbon atoms is identical to OPLS. Bonds are harmonic and have a force constant of 469 kcal/Å^2 and an equilibrium distance of 1.4 Å. Angles have a force constant of 63 kcal/rad^2 and an equilibrium angle of 120 $^{\circ}$. For dihedrals, only k_2 has a non-zero value of 7.25 kcal/rad^2. For non-bonding interqactions, LJ potential is used and equilibrium energy and distance are respectively 0.02 kcal/Å^2 and 3.55 Å. Arithmetic mixing rules apply to determine pair interactions with other system atoms.

A.1.2 DREIDING force field models

The original DREIDING force fields, which we have denoted DREIDING/LJ, use harmonic potentials for the bond stretch and angle, as described previously in equations A.1 and A.2. Dihedrals are described using the following form

$$E_d(\phi) = k_\phi(1 + d\ cos(\phi)) \tag{A.6}$$

where ϕ is the dihedral angle, d a unitless parameter that takes the form of either a positive or negative one depending on force field to define the harmonic style, n is a positive integer and k_ϕ is the dihedral strength. Non-bonded van der Waals interactions are described using the LJ potential in equation A.4 with a cutoff of 12 Å. The original DREIDING force field does not include partial charges. We have denoted the original DREIDING force field as DREIDING/LJ. All parameters used for EPON-862 and DETDA were taken from Mayo *et al.* [75].

A variation of the DREIDING force field, denoted DREIDING/X6, replaces the LJ potential with the Buckingham potential

$$E_{\mathrm{X6}}(r) = A \exp\left[\frac{-r}{\rho}\right] - \frac{C}{r^6} \tag{A.7}$$

where A, ρ and C are parameters. These parameters can be related to LJ sigma and

epsilon via the following relations [70]

$$C = \left(\frac{\alpha}{\alpha - 6}\right) \epsilon \sigma^6 \tag{A.8}$$

$$\rho = \frac{\sigma}{\alpha} \tag{A.9}$$

and

$$A = \epsilon \left(\frac{6}{\alpha - 6}\right) e^{\alpha} \tag{A.10}$$

Setting $\alpha = 12$ means that the Buckingham potential is close to the LJ potential at small values of r. This was the value used by Li *et al.* [67] and we have used these parameters for our DREIDING/X6 parameters. We have denoted this version of the DREIDING force field as DREIDING/X6.

Variations of the DREIDING force field include partial atomic charges, and we have denoted these as DREIDING/LJ/Q and DREIDING/X6/Q. Partial charges for EPON-862 and DETDA were taken from Demir *et al.* [32]. Electrostatic interactions are directly calculated up to a cutoff of 8 Å, after which the remaining interactions are calculated by EWALD mesh.

DREIDING parameters for EPON-862

Bond, angle, and dihedral parameters are the same for all DREIDING variants for each molecule. Only four atom designations exist for EPON-862: alkyl carbons (C_3), aromatic carbons (C_R), oxigens (O_3) and hydrogens (H_) as denoted in Figure A.9. Bonding parameters are in tables A.17, A.18 and A.19. Non-bonding parameters are in table A.20 and Figure A.10.

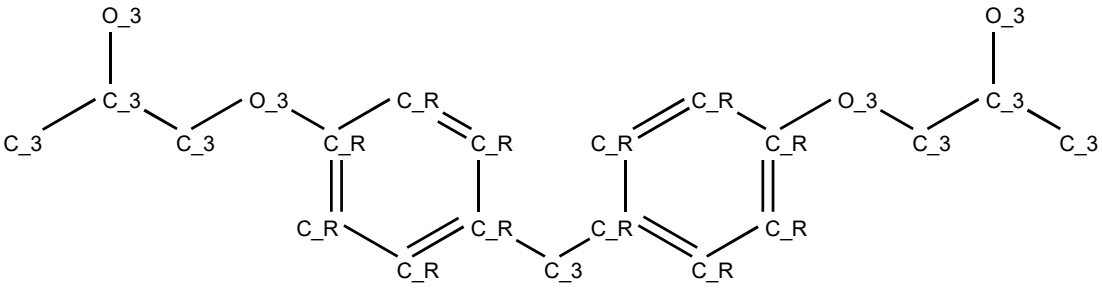

Figure A.9: EPON-862 atom labels for DREIDING force field. Hydrogens are omitted and have single label "H_".

Table A.17: DREIDING bond parameters for EPON-862. Bond constant (k_r) given in kcal/Å^2 and equilibrium distance (r_0) given in Å.

Bonds		
Description	k_r	r_0
C_3-H_	350	1.09
C_3-C_3	350	1.53
C_3-O_3	350	1.42
O_3-H_	350	0.98
O_3-C_R	350	1.35
C_R-C_R	525	1.39
C_R-H_	350	1.02
C_R-C_3	350	1.46

Table A.18: DREIDING angle parameters for EPON-862. Spring constant (k_θ) given in kcal/rad^2 and equilibrium distance (θ_0) given in degrees.

Angles		
Description	k_θ	θ_0
C_3-C_3-C_3	50	109.47
C_3-O_3-C_R	50	104.50
C_R-C_R-C_R	50	120.00

Table A.19: DREIDING dihedral parameters for EPON-862. Dihedral constant (k_ϕ) given in kcal/rad^2 and orientation (d) and multiplicity (n) are unitless.

Dihedrals			
Description	k_ϕ	d	n
X-C_3-C_3-X	0.33	-1	3
X-O_3-C_3-X	0.33	-1	3
X-C_R-C_R-X	6.3	-1	2
C_R -C_R-C_3-X	0.083	-1	6
X-O_3-C_R-X	0.50	-1	2

Table A.20: DREIDING LJ and X6 parameters for EPON-862. LJ equilibrium energy (ϵ) and distance at zero energy (σ) given in kcal/Å^2 and X6 parameters A, B and C are unitless quantities derived from LJ parameters.

	Lennard-Jones		**Buckingham**		
Pair	ϵ (kcal)	σ (kcal Å^{-2})	A	B	C
C_3	0.0951	3.473	15480	0.3249	667.5
C_R	0.0951	3.473	15480	0.3249	667.5
H_	0.0152	2.846	2474	0.2663	32.34
O_3	0.0957	3.033	15580	0.2837	98.08

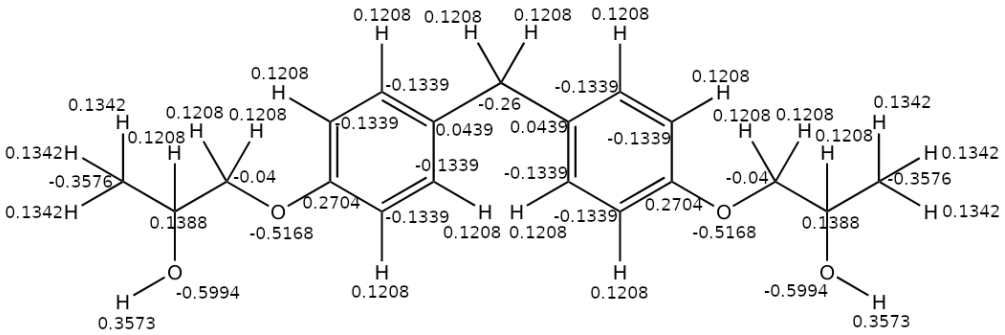

Figure A.10: DREIDING partial atomic charges for EPON-862.

DREIDING parameters for DETDA

Bond, angle, and dihedral parameters are the same for all DREIDING variants for each molecule. Only four atom designations exist for EPON-862: alkyl carbons (C_3), aromatic cabons (C_R), nitrogen (N_2) and hydrogens (H_) as denoted in Figure A.11. Bonding parameters are in tables A.21, A.22 and A.23. Non-bonding parameters are in table A.24 and Figure A.12.

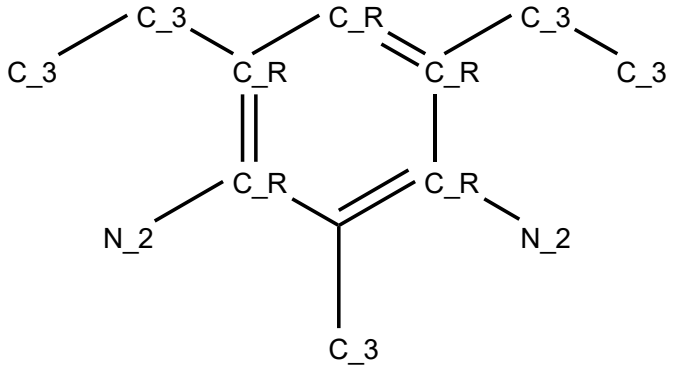

Figure A.11: DETDA atom labels for DREIDING force field. Hydrogens are omitted and have single label "H_".

Table A.21: DREIDING bond parameters for DETDA. Bend constant (k_r) given in kcal/Å^2 and equilibrium distance (r_0) given in Å.

Bonds		
Description	k_r	r_0
C_R-H_	350	1.01
C_R-C_3	350	1.46
C_3-C_3	350	1.53
C_3-H_	350	1.09
N_2-H_	350	0.935
C_R-C_R	525	1.39
C_R-N_2	700	1.305

Table A.22: DREIDING angle parameters for DETDA. Spring constant (k_θ) given in kcal/rad^2 and equilibrium distance (θ_0) given in degrees.

Angles		
Description	k_θ	θ_0
C_R-C_3-C_3	50	109.47
C_3-C_3-H_	50	109.47
C_R-C_3-H_	50	109.47
H_-C_3-H_	50	109.47
C_R-C_R-CR	50	120.00
C_R-C_R-H_	50	120.00
C_R-C_R-N_2	50	120.00
H_-N_2-C_R	50	120.00
C_R-C_R-H_	50	120.00
H_-N_2-H_	50	120.00

Table A.23: DREIDING dihedral parameters for EPON-862. Dihedral constant (k_ϕ) given in kcal/Å^2 and orientation (d) and multiplicity (n) are unitless.

Dihedrals			
Description	k_ϕ	d	n
C_R-C_R-C_R-C_3	6.25	-1	2
C_R-C_R-C_R-H_	6.25	-1	2
C_R-C_R-C_R-N_2	6.25	-1	2
C_R-C_R-C_R-C_R	6.25	-1	2
H_-C_R-C_R-C_R	6.25	-1	2
N_2-C_R-C_R-C_R	6.25	-1	2
C_R-C_R-N_2-H_	6.25	-1	2
H_-C_3-C_3-H_	0.500	-1	3
H_-C_3-C_3-H_	1.00	-1	3
C_R-C_R-C_3-C_3	0.250	-1	6
C_R-C_R-C_3-H_	0.250	-1	6

Table A.24: DREIDING X6 parameters for EPON-862. A, B and C are derived from LJ parameters.

	Buckingham		
Pair	A	B	C
C_3 C_R	15484	0.36464	1335.6
H_	2474	0.2989	64.67
N_2	12600	0.3426	746.8

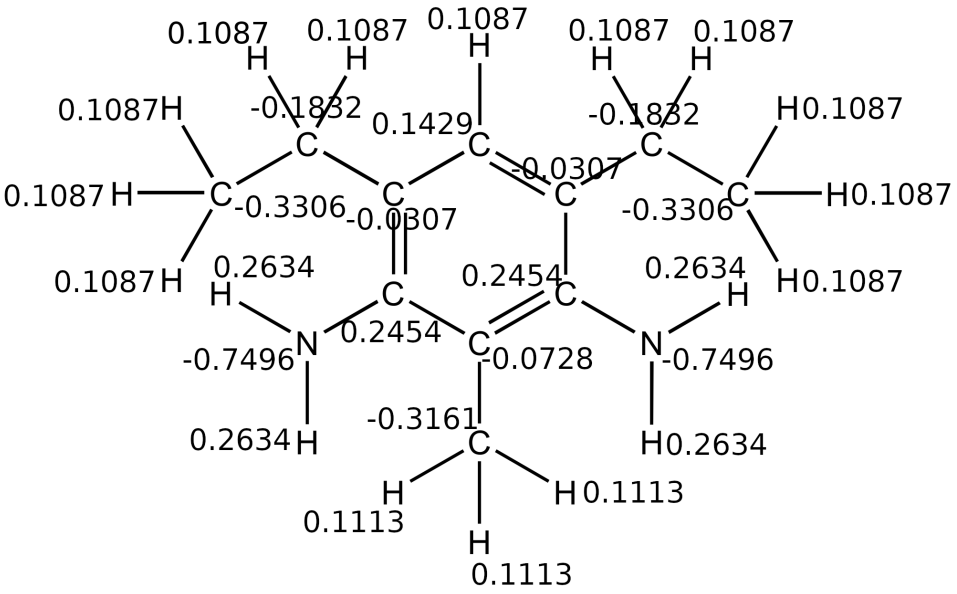

Figure A.12: DREIDING partial atomic charges for DETDA.

A.2 Equilibration for EPON-862, DETDA and DDS

The equilibration of the systems was performed by matching simulation density of pure liquids, at 300 K, to other computational works as well as experimental values. These initial simulations deemed 4 ns to be more than sufficient to achieve target density and density was averaged over the next 10 ns. All six mentioned force field variants were tested on a liquid EPON-862 system yielding the density plots in Figure A.13.

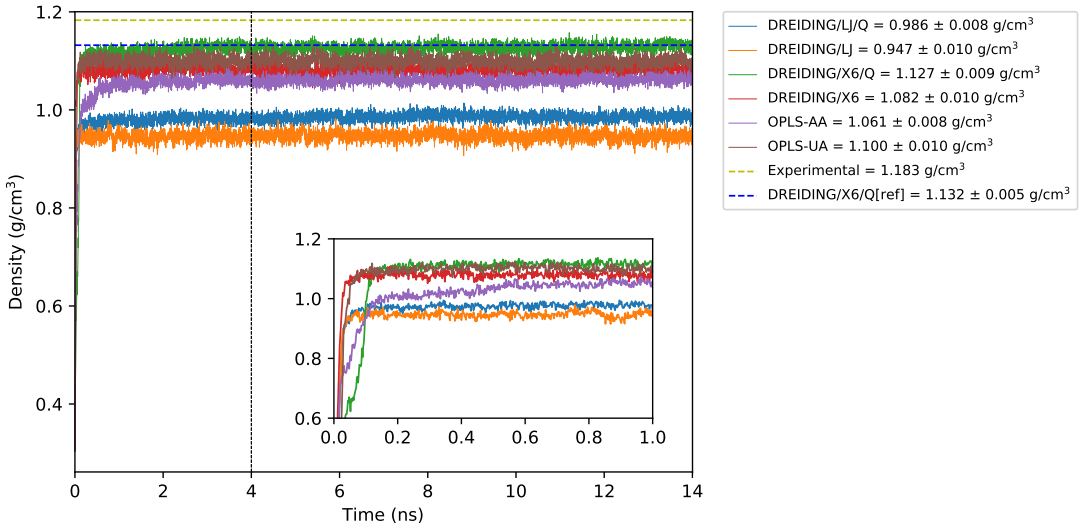

Figure A.13: Density equilibration with all force fields on bulk EPON-862at 300 K.

Density for DETDA and DDS for the final selected force field, OPLS-UA, can be found in Figures A.14 and A.15 showing that OPLS-UA behaves consistently across all three molecules.

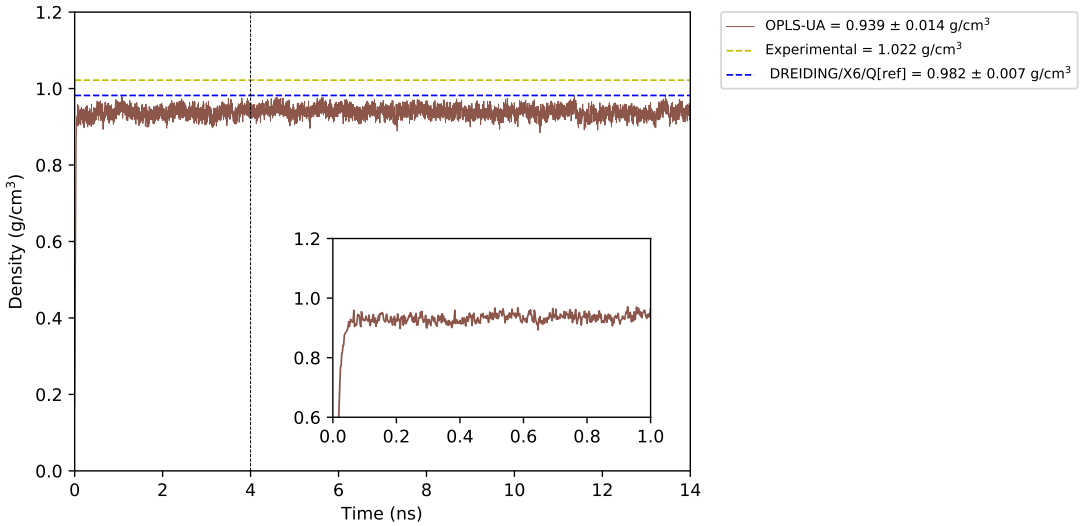

Figure A.14: Density equilibration with OPLS-UA for bulk DETDA at 300 K.

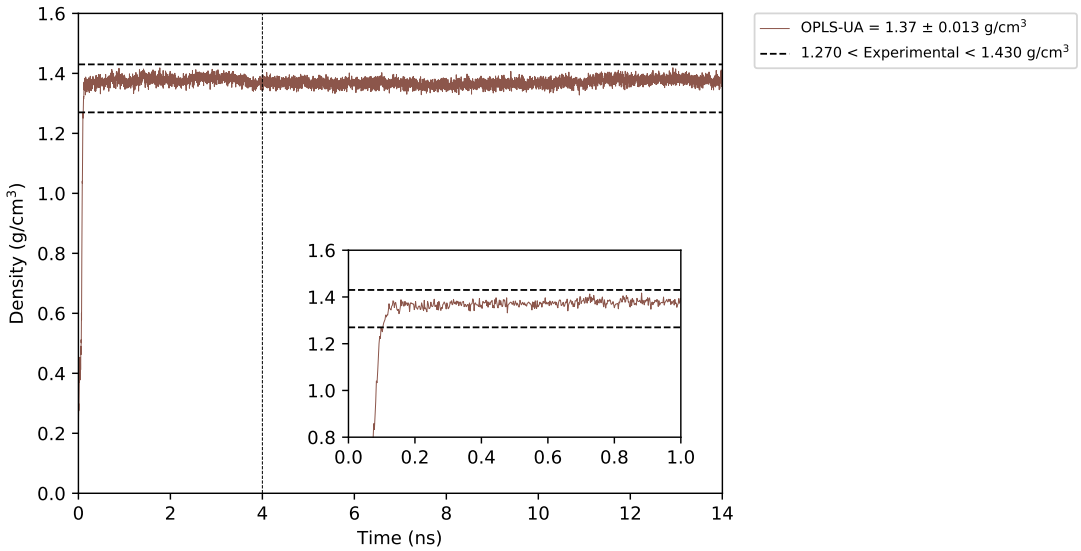

Figure A.15: Density equilibration with OPLS-UA for bulk DDS at 300 K.

Bibliography

[1] https://pubchem.ncbi.nlm.nih.gov/compound/Dapsone, accessed on 2021-03-01.

[2] https://www.albemarle.com/storage/wysiwyg/cur-0003_detda_tds_102417.pdf, accessed on 2021-02-12.

[3] https://www.chemicalbook.com/ChemicalProductProperty_EN_CB0152851.htm, accessed on 2021-02-12.

[4] https://www.hexion.com/en-US/product/epikote-resin-862, accessed on 2020-12-16.

[5] https://www.hexion.com/en-US/product/epon-resin-862#tds, accessed on 2020-12-16.

[6] https://www.nist.gov/mml/csd/chemical-informatics-group/lennard-jones-fluid-properties, accessed on 2021-10-27.

[7] http://www.chemspider.com/Chemical-Structure.2849.html, accessed on 2021-03-01.

[8] ABRAMS, C. F., AND KREMER, K. Combined coarse-grained and atomistic simulation of liquid bisphenol a-polycarbonate: Liquid packing and intramolecular structure. *Macromolecules 36* (2003), 260–267.

[9] AKKERMANS, R. L., TOXVAERD, S., AND BRIELS, W. J. Molecular dynamics of polymer growth. *Journal of Chemical Physics 109*, 7 (1998), 2929–2940.

[10] ALBERDI, A., ARTAZA, T., SUÁREZ, A., RIVERO, A., AND GIROT, F. An experimental study on abrasive waterjet cutting of CFRP/Ti6Al4V stacks for drilling operations. *The International Journal of Advanced Manufacturing Technology 2015 86:1 86*, 1 (2015), 691–704.

[11] ALDER, B. J., AND WAINWRIGHT, T. E. Studies in Molecular Dynamics. I. General Method. *The Journal of Chemical Physics 31*, 2 (1959), 459.

[12] ARNOLD, C. L., EYCKENS, D. J., SERVINIS, L., NAVE, M. D., YIN, H., MARCEAU, R. K., PINSON, J., DEMIR, B., WALSH, T. R., AND HENDERSON, L. C. Simultaneously increasing the hydrophobicity and interfacial adhesion of carbon fibres: a simple pathway to install passive functionality into composites. *Journal of Materials Chemistry A 7*, 22 (2019), 13483–13494.

[13] ATIF, R., SHYHA, I., AND INAM, F. Mechanical, thermal, and electrical properties of graphene-epoxy nanocomposites—a review. *Polymers 8*, 8 (2016), 281.

[14] ATKINSON, K. E. *An introduction to numerical analysis*, 2 ed. John Wiley & Sons, 1989.

[15] BAKSHI, S. R., LAHIRI, D., AGARWAL, . A., AND AGARWAL, A. Carbon nanotube reinforced metal matrix composites-a review. *International Materials Reviews 55*, 1 (2013), 41–64.

[16] BALASUBRAMANIAN, K., SULTAN, M. T., AND RAJESWARI, N. Manufacturing techniques of composites for aerospace applications. In *Sustainable Composites for Aerospace Applications*. Woodhead Publishing, 2018, pp. 55–67.

[17] BALJON, A. R. C., WILLIAMS, S., BALABAEV, N. K., PAANS, F., HUDZINSKYY, D., AND LYULIN, A. V. Simulated glass transition in free-standing thin polystyrene films. *Journal of Polymer Science B 48* (2010), 1160.

[18] BARBER, A. H., COHEN, S. R., KENIG, S., AND WAGNER, H. D. Interfacial fracture energy measurements for multi-walled carbon nanotubes pulled from a polymer matrix. *Composites science and technology 64*, 15 (2004), 2283–2289.

[19] BARNES, J. C., PATON, J. D., JR., J. R. D., AND MISLOW, K. Crystal and molecular structure of diphenylmethane. *Journal of Organic Chemistry 46*, 24 (1981), 4975–4979.

[20] BEHR, M. J., LANDES, B. G., BARTON, B. E., BERNIUS, M. T., BILLOVITS, G. F., HUKKANEN, E. J., PATTON, J. T., WANG, W., WOOD, C., KEANE, D. T., RIX, J. E., AND WEIGAND, S. J. Structure-property model for polyethylene-derived carbon fiber. *Carbon 107* (2016), 525–535.

[21] BERENDSEN, H. J. C., POSTMA, J. P. M., VAN GUNSTEREN, W. F., DINOLA, A., AND HAAK, J. R. Molecular dynamics with coupling to an external bath. *The Journal of Chemical Physics 81*, 8 (1984), 3684–3690.

[22] BIRDSALL, C. K., AND LANGDON, A. B. *Plasma physics via computer simulation*, 1 ed. Taylor & Francis, 2005.

[23] BÖHM, M. C., AND GLEITER, R. A CNDO/INDO molecular orbital formalism for the elements H to Br. theory. *Theoretica chimica acta 1981 59:2 59*, 2 (1981), 127–151.

[24] BORN, M., AND OPPENHEIMER, R. Zur Quantentheorie der Molekeln. *Annalen der Physik 389*, 20 (1927), 457–484.

[25] CERCIGNANI, C., AND PENROSE, R. *Ludwig Boltzmann: The Man Who Trusted Atoms*. Oxford University Press, 2006.

[26] CHUNG, D. *Carbon fiber composites*, 1 ed. Butterworth-Heinemann, Boston, 1994.

[27] COLEMAN, J. N., KHAN, U., BLAU, W. J., AND GUN'KO, Y. K. Small but strong: A review of the mechanical properties of carbon nanotube–polymer composites. *Carbon 44*, 9 (2006), 1624–1652.

[28] CORTI, D. S. Isothermal-isobaric ensemble for small systems. *Physical Review E 64*, 1 (2001), 016128.

[29] CRAMER, C. J. *Essential of Computational Chemistry. Theories and Models*, 2 ed. John Wiley & Sons, Chichester, 2004.

[30] DAVIM, J. P., AND REIS, P. Drilling carbon fiber reinforced plastics manufactured by autoclave—experimental and statistical study. *Materials Design 24*, 5 (2003), 315–324.

[31] DEMIR, B., HENDERSON, L. C., AND WALSH, T. R. Design Rules for Enhanced Interfacial Shear Response in Functionalized Carbon Fiber Epoxy Composites. *ACS Applied Materials & Interfaces 9*, 13 (2017), 11846–11857.

[32] DEMIR, B., AND WALSH, T. R. A robust and reproducible procedure for cross-linking thermoset polymers using molecular simulation. *Soft Matter 12*, 8 (2016), 2453–2464.

[33] DEMIR, B., AND WALSH, T. R. A robust and reproducible procedure for cross-linking thermoset polymers using molecular simulation. *Soft Matter 12*, 8 (2016), 2453–2464.

[34] DEVRIES, P. L., AND HASBUN, J. E. *A first course in computational physics*, 2nd ed. Jones and Bartlett Publishers, Inc, 2010.

[35] DOIG, M., AND CAMP, P. J. The structures of hexadecylamine films adsorbed on iron-oxide surfaces in dodecane and hexadecane. *Physical Chemistry Chemical Physics 17*, 7 (2015), 5248–5255.

[36] DOIG, M., WARRENS, C. P., AND CAMP, P. J. Structure and friction of stearic acid and oleic acid films adsorbed on iron oxide surfaces in squalane. *Langmuir 30*, 1 (2014), 186–195.

[37] DUNWEG, B., AND PAUL, W. Brownian dynamics simulations without gaussian random numbers. *International Journal of Modern Physics C 02*, 03 (1991), 817–827.

[38] EVERAERS, R., KARIMI-VARZANEH, H. A., FLECK, F., HOJDIS, N., AND SVANEBORG, C. Kremer–Grest Models for Commodity Polymer Melts: Linking Theory, Experiment, and Simulation at the Kuhn Scale. *Macromolecules 53*, 6 (2020), 1901–1916.

[39] FARAH, K., LANGELOTH, M., BÖHM, M. C., AND MÜLLER-PLATHE, F. Surface-Induced Interphases During Curing Processes Between Bi- and Pentafunctional Components: Reactive Coarse-Grained Molecular Dynamics Simulations. *The Journal of Adhesion 88* (2012), 903–923.

[40] FARAH, K., LEROY, F., MÜLLER-PLATHE, F., AND BÖHM, M. C. Interphase formation during curing: Reactive coarse grained molecular dynamics simulations. *Journal of Physical Chemistry C 115*, 33 (2011), 16451–16460.

[41] FARAH, K., MÜLLER-PLATHE, F., AND BÖHM, M. C. Classical reactive molecular dynamics implementations: State of the art. *ChemPhysChem 13*, 5 (2012), 1127–1151.

[42] FIORE, V., DI BELLA, G., AND VALENZA, A. Effect of Sheep Wool Fibers on Thermal Insulation and Mechanical Properties of Cement-Based Composites. *Journal of Natural Fibers 17*, 10 (2019), 1532–1543.

[43] FLORY, P. *Principles of polymer chemistry*. 1953.

[44] FRANK, E., STEUDLE, L. M., INGILDEEV, D., SPÖRL, J. M., AND BUCHMEISER, M. R. Carbon fibers: Precursor systems, processing, structure, and properties. *Angewandte Chemie - International Edition 53*, 21 (2014), 5262–5298.

[45] GAITONDE, V. N., KARNIK, S. R., RUBIO, J. C., CORREIA, A. E., ABRÃO, A. M., AND DAVIM, J. P. Analysis of parametric influence on delamination in high-speed drilling of carbon fiber reinforced plastic composites. *Journal of Materials Processing Technology 203*, 1-3 (2008), 431–438.

[46] GASSON, P. C. Asm handbook vol 21—composites sd henry et al asm international, materials park, oh 44073-0002, usa. 2001. distributed by american technical publishers, 27-29 knowl piece, wilbury way, hitchin, herts sg4 osx, uk. 1201pp. illustrated.£ 177. isbn 0-87170-703-9. *The Aeronautical Journal 106*, 1064 (2002), 582–582.

[47] GAVRILOV, A. A., KOMAROV, P. V., AND KHALATUR, P. G. Thermal properties and topology of epoxy networks: A multiscale simulation methodology. *Macromolecules 48*, 1 (2015), 206–212.

[48] GRØNBECH-JENSEN, N., AND FARAGO, O. A simple and effective Verlet-type algorithm for simulating Langevin dynamics. *Molecular Physics 111*, 8 (2013), 983–991.

[49] HADDEN, C., JENSEN, B., BANDYOPADHYAY, A., ODEGARD, G., KOO, A., AND LIANG, R. Molecular modeling of epon-862/graphite composites: Interfacial characteristics for multiple crosslink densities. *Composites Science and Technology 76* (2013), 92 – 99.

[50] HADDEN, C. M., KLIMEK-MCDONALD, D. R., PINEDA, E. J., KING, J. A., REICHANADTER, A. M., MISKIOGLU, I., GOWTHAM, S., AND ODEGARD, G. M. Mechanical properties of graphene nanoplatelet/carbon fiber/epoxy hybrid composites: Multiscale modeling and experiments. *Carbon 95* (2015), 100–112.

[51] HANNA, D., AND GOODMAN, S. H. *Handbook of Thermoset Plastics.*, 3rd ed. Elsevier Science, 2013.

[52] HOOVER, W. G. Canonical dynamics: Equilibrium phase-space distributions. *Physical Review A 31*, 3 (1985), 1695–1697.

[53] HORIE, K., BARÓN, M., FOX, R. B., HE, J., HESS, M., KAHOVEC, J., KITAYAMA, T., KUBISA, P., MARÉCHAL, E., MORMANN, W., STEPTO, R. F., TABAK, D., VOHLÍDAL, J., WILKS, E. S., AND WORK, W. J. Definitions of terms relating to reactions of polymers and to functional polymeric materials: (IUPAC Recommendations 2003). *Pure and Applied Chemistry 76*, 4 (2004), 889–906.

[54] HUGHES, J. D. The carbon fibre/epoxy interface—A review. *Composites Science and Technology 41*, 1 (1991), 13–45.

[55] HUGHES, J. D., MORLEY, H., AND JACKSON, E. E. Aligned carbon fibre com-

posite which approaches theoretical strength. *Journal of Physics D: Applied Physics 13*, 6 (1980), 921.

[56] IANNUCCI, L., DAWOOD, M. S. I. S., GREENHALGH, E. S., AND ARIFFIN, A. K. Delamination control in composite beams using piezoelectric actuators.

[57] ISMAIL, I. K., AND VANGSNESS, M. D. On the improvement of carbon fiber/matrix adhesion. *Carbon 26*, 5 (1988), 749–751.

[58] JOHNSTON, K., AND HARMANDARIS, V. Properties of Short Polystyrene Chains Confined Between two Gold Surfaces Through a Combined Density Functional Theory and Classical Molecular Dynamics Approach. *Soft Matter 8* (2012), 6320–6332.

[59] JORGENSEN, W. L., MAXWELL, D. S., AND TIRADO-RIVES, J. Development and Testing of the OPLS All-Atom Force Field on Conformational Energetics and Properties of Organic Liquids. *Journal of American Chemical Society 118*, 45 (1996), 11225–11236.

[60] JORGENSEN, W. L., AND TIRADO-RIVES, J. The OPLS Potential Functions for Proteins. Energy Minimizations for Crystals of Cyclic Peptides and Crambin. *Journal of the American Chemical Society 110*, 6 (1988), 1657–1666.

[61] KIMBERLY CHENOWETH, , ADRI C. T. VAN DUIN, AND WILLIAM A. GODDARD, I. ReaxFF Reactive Force Field for Molecular Dynamics Simulations of Hydrocarbon Oxidation. *Journal of Physical Chemistry A 112*, 5 (2008), 1040–1053.

[62] KREMER, K., AND GREST, G. S. Dynamics of entangled linear polymer melts: A molecular-dynamics simulation. *The Journal of Chemical Physics 92*, 8 (1990), 5057–5086.

[63] KURDI, A., KAN, W. H., AND CHANG, L. Tribological behaviour of high performance polymers and polymer composites at elevated temperature. *Tribology International 130* (2019), 94–105.

[64] LI, C., AND STRACHAN, A. Molecular dynamics predictions of thermal and mechanical properties of thermoset polymer EPON862/DETDA. *Polymer 52* (2010), 2920–2928.

[65] LI, C., AND STRACHAN, A. Molecular simulations of crosslinking process of thermosetting polymers. *Polymer 51*, 25 (2010), 6058–6070.

[66] LI, C., AND STRACHAN, A. Molecular simulations of crosslinking process of thermosetting polymers. *Polymer 51* (2010), 6058–6070.

[67] LI, C., AND STRACHAN, A. Molecular Scale Simulations on Thermoset Polymers : A Review. *Journal of Polymer Science Part B: Polymer Physics 53*, 2 (2015), 103–122.

[68] LI, Y., HUANG, X., ZENG, L., LI, R., TIAN, H., FU, X., WANG, Y., AND ZHONG, W.-H. A review of the electrical and mechanical properties of carbon nanofiller-reinforced polymer composites. *Journal of Materials Science 54*, 2 (2019), 1036–1076.

[69] LIM, T. C. Mathematical relationships for development of a molecular potential function converter. *Match - Communications in mathematical and in computer chemistry 49*, 4 (2003), 155–169.

[70] LIM, T. C. Scaling function between the Exponential-6 and the generalized Lennard-Jones potential functions. *Journal of Mathematical Chemistry 33*, 4 (2003), 279–285.

[71] LIU, H., LI, M., LU, Z. Y., ZHANG, Z. G., AND SUN, C. C. Influence of Surface-Initiated Polymerization Rate and Initiator Density on the Properties of Polymer Brushes. *Macromolecules 42*, 7 (2009), 2863–2872.

[72] LIU, Y., AND KUMAR, S. Polymer/carbon nanotube nano composite fibers-A review. *ACS Applied Materials and Interfaces 6*, 9 (2014), 6069–6087.

[73] LOPATTANANON, N., KETTLE, A. P., TRIPATHI, D., BECK, A. J., DUVAL, E., FRANCE, R. M., SHORT, R. D., AND JONES, F. R. Interface molecular engi-

neering of carbon-fiber composites. *Composites Part A: Applied Science and Manufacturing 30*, 1 (1999), 49–57.

[74] LUSTIG, R. Statistical thermodynamics in the classical molecular dynamics ensemble. I. Fundamentals. *The Journal of Chemical Physics 100*, 4 (1998), 3048.

[75] MAYO, S. L., OLAFSON, B. D., AND GODDARD, W. A. DREIDING: A generic force field for molecular simulations. *Journal of Physical Chemistry 94*, 26 (1990), 8897–8909.

[76] MAYO, S. L., OLAFSON, B. D., AND WILLIAM A. GODDARD III. DREIDING: A Generic Force Field for Molecular Simulations. *J. Phys. Chem. 94* (1990), 8897–8909.

[77] MCKECHNIE, D., ANKER, S., ZAHID, S., MULHERAN, P. A., SEFCIK, J., AND JOHNSTON, K. Interfacial Concentration Effect Facilitates Heterogeneous Nucleation from Solution. *The Journal of Physical Chemistry Letters 11*, 6 (2020), 2263–2271.

[78] METROPOLIS, N., ROSENBLUTH, A. W., ROSENBLUTH, M. N., TELLER, A. H., AND TELLER, E. Equation of State Calculations by Fast Computing Machines. *The Journal of Chemical Physics 21*, 6 (1953), 1087.

[79] MEUWLY, M., BECKER, O. M., STOTE, R., AND KARPLUS, M. NO rebinding to myoglobin: a reactive molecular dynamics study. *Biophysical Chemistry 98*, 1-2 (2002), 183–207.

[80] MORIN, D. *Introduction to Classical Mechanics*, 1 ed. Cambridge University Press, New York, 2008.

[81] MORSALI, A., GOHARSHADI, E. K., ALI MANSOORI, G., AND ABBASPOUR, M. An accurate expression for radial distribution function of the Lennard-Jones fluid. *Chemical Physics 310*, 1-3 (2005), 11–15.

[82] MULLER, P. Glossary of terms used in physical organic chemistry: (IUPAC

Recommendations 1994). *Pure and Applied Chemistry 66*, 5 (1994), 1077–1184.

[83] NEWMARK, N. M. A Method of Computation for Structural Dynamics. *Journal of the Engineering Mechanics Division 85*, 3 (1959), 67–94.

[84] NOSÉ, S. A unified formulation of the constant temperature molecular dynamics methods. *The Journal of Chemical Physics 81*, 1 (1984), 511–519.

[85] NOSÉ, S., AND KLEIN, M. Constant pressure molecular dynamics for molecular systems. *Molecular Physics 50*, 5 (1983), 1055–1076.

[86] PARK, S. J. *Carbon Fibers*, 2 ed. Springer, Singapore, 2018.

[87] PARK, S. J., KIM, M. H., LEE, J. R., AND CHOI, S. Effect of Fiber–Polymer Interactions on Fracture Toughness Behavior of Carbon Fiber-Reinforced Epoxy Matrix Composites. *Journal of Colloid and Interface Science 228*, 2 (2000), 287–291.

[88] PEARSON, E. M., HALICIOGLU, T., AND TILLER, W. A. Laplace-transform technique for deriving thermodynamic equations from the classical microcanonical ensemble. *Physical Review A 32*, 5 (1985), 3030.

[89] PEREZ, M., LAME, O., LEONFORTE, F., AND BARRAT, J. L. Polymer chain generation for coarse-grained models using radical-like polymerization. *Journal of Chemical Physics 128*, 23 (2008), 234904–234914.

[90] PERSSON, E., ERIKSSON, I., AND ZACKRISSON, L. Effects of hole machining defects on strength and fatigue life of composite laminates. *Composites Part A: Applied Science and Manufacturing 28*, 2 (1997), 141–151.

[91] PHIRI, J., GANE, P., AND MALONEY, T. C. General overview of graphene: Production, properties and application in polymer composites. *Materials Science and Engineering: B 215* (2017), 9–28.

[92] PHIRI, J., GANE, P., AND MALONEY, T. C. General overview of graphene: Production, properties and application in polymer composites. *Materials Science and Engineering: B 215* (2017), 9–28.

[93] PIGGOTT, M. R. The interface in carbon fibre composites. *Carbon 27*, 5 (1989), 657–662.

[94] PLIMPTON, S. Fast Parallel Algorithms for Short-Range Molecular Dynamics. *Journal of Computational Physics 117* (1995), 1–19.

[95] QIAN, D., DICKEY, E. C., ANDREWS, R., AND RANTELL, T. Load transfer and deformation mechanisms in carbon nanotube-polystyrene composites. *Applied Physics Letters 76*, 20 (2000), 2868–2870.

[96] RIBEIRO, B., BOTELHO, E., COSTA, M., AND BANDEIRA, C. Carbon nanotube buckypaper reinforced polymer composites: A review. *Polímeros 27* (2017).

[97] ROSENBLUTH, M. N., AND ROSENBLUTH, A. W. Further Results on Monte Carlo Equations of State. *The Journal of Chemical Physics 22*, 5 (1954), 881.

[98] RUAN, S., GAO, P., YANG, X., AND YU, T. Toughening high performance ultrahigh molecular weight polyethylene using multiwalled carbon nanotubes. *Polymer 44* (2003), 5643–5654.

[99] RUBINSTEIN, M., AND COLBY, R. *Polymer Physics*. Oxford University Press, 2003.

[100] SAFADI, B., ANDREWS, R., AND GRULKE, E. A. Multiwalled carbon nanotube polymer composites: Synthesis and characterization of thin films. *Journal of Applied Polymer Science 84*, 14 (2002), 2660–2669.

[101] SANDLER, J., PEGEL, S., ČADEK, M., GOJNY, F., VAN ES, M., LOHMAR, J., BLAU, W., KARL, S., WINDLE, A., AND SHAFFER, M. A comparative study of melt spun polyamide-12 fibres reinforced with carbon nanotubes and nanofibres. *Polymer 45* (2004), 2001–2015.

[102] SCHNEIDER, T., AND STOLL, E. Molecular-dynamics study of a three-dimensional one-component model for distortive phase transitions. *Physical Review B 17*, 3 (1978), 1302–1322.

[103] SERVINIS, L., BEGGS, K. M., SCHEFFLER, C., WOLFEL, E., RANDALL, J. D., GENGENBACH, T. R., DEMIR, B., WALSH, T. R., DOEVEN, E. H., FRANCIS, P. S., AND HENDERSON, L. C. Electrochemical surface modification of carbon fibres by grafting of amine, carboxylic and lipophilic amide groups. *Carbon 118*, 17 (2017), 393–403.

[104] SHAFFER, M. S. P., AND WINDLE, A. H. Fabrication and characterization of carbon nanotube/poly(vinyl alcohol) composites. *Advanced Materials 11*, 11 (1999), 937–941.

[105] SHARMA, M., GAO, S., MÄDER, E., SHARMA, H., WEI, L. Y., AND BIJWE, J. Carbon fiber surfaces and composite interphases. *Composites Science and Technology 102* (2014), 35–50.

[106] SHENOY, A. *Thermoplastic Melt Rheology and Processing*, 1st ed. CRC Press, 1996.

[107] SHUKLA, M. K., AND SHARMA, K. Improvement in mechanical and thermal properties of epoxy hybrid composites by functionalized graphene and carbon-nanotubes. *Materials Research Express 6*, 12 (2019), 125323.

[108] SINCLAIR, R. C., SUTER, J. L., AND COVENEY, P. V. Graphene-Graphene Interactions: Friction, Superlubricity, and Exfoliation. *Advanced Materials 30*, 13 (2018), 1705791.

[109] SODDEMANN, T., DÜ, B., AND KREMER, K. Dissipative particle dynamics: A useful thermostat for equilibrium and nonequilibrium molecular dynamics simulations.

[110] SODDEMANN, T., DÜNWEG, B., AND KREMER, K. Dissipative particle dynamics: A useful thermostat for equilibrium and nonequilibrium molecular dynamics sim-

ulations. *Physical Review E - Statistical Physics, Plasmas, Fluids, and Related Interdisciplinary Topics 68*, 4 (2003), 046702.

[111] SOUTIS, C. Fibre reinforced composites in aircraft construction. *Progress in Aerospace Sciences 41*, 2 (2005), 143–151.

[112] SPITALSKY, Z., TASIS, D., PAPAGELIS, K., AND GALIOTIS, C. Carbon nanotube–polymer composites: Chemistry, processing, mechanical and electrical properties. *Progress in Polymer Science 35*, 3 (2010), 357–401.

[113] STEPHAN, S., AND DEITERS, U. K. Characteristic Curves of the Lennard-Jones Fluid. *International Journal of Thermophysics 41*, 10 (2020), 1–24.

[114] STEPHAN, S., THOL, M., VRABEC, J., AND HASSE, H. Thermophysical Properties of the Lennard-Jones Fluid: Database and Data Assessment. *The Jounral of Chemical Information and Modeling 59*, 10 (2019), 4248–4265.

[115] SUN, H. Compass: An ab initio force-field optimized for condensed-phase applications - Overview with details on alkane and benzene compounds. *Journal of Physical Chemistry B 102*, 38 (1998), 7338–7364.

[116] SUN, H. COMPASS: An ab Initio Force-Field Optimized for Condensed-Phase ApplicationssOverview with Details on Alkane and Benzene Compounds. *Journal of Physical Chemistry 102*, 38 (1998), 7338–7364.

[117] SWOPE, W. C., ANDERSEN, H. C., BERENS, P. H., AND WILSON, K. R. A computer simulation method for the calculation of equilibrium constants for the formation of physical clusters of molecules: Application to small water clusters. *The Journal of Chemical Physics 76*, 1 (1982), 637–649.

[118] TARFAOUI, M., LAFDI, K., AND EL MOUMEN, A. Mechanical properties of carbon nanotubes based polymer composites. *Composites Part B: Engineering 103* (2016), 113–121.

[119] TODD, B. D., AND DAIVIS, P. J. Statistical Mechanical Foundations. In *Nonequilibrium Molecular Dynamics*. Cambridge University Press, Cambridge, 2017, pp. 31–58.

[120] TOTRY, E., MOLINA-ALDAREGUÍA, J. M., GONZÁLEZ, C., AND LLORCA, J. Effect of fiber, matrix and interface properties on the in-plane shear deformation of carbon-fiber reinforced composites. *Composites Science and Technology 70*, 6 (2010), 970–980.

[121] VAN DUIN, A. C., DASGUPTA, S., LORANT, F., AND GODDARD, W. A. ReaxFF: A reactive force field for hydrocarbons. *Journal of Physical Chemistry A 105*, 41 (2001), 9396–9409.

[122] VARSHNEY, V., PATNAIK, S. S., ROY, A. K., AND FARMER, B. L. A Molecular Dynamics Study of Epoxy-Based Networks : Cross-Linking Procedure and Prediction of Molecular and Material Properties. *Macromolecules 41*, 18 (2008), 6837–6842.

[123] VARSHNEY, V., PATNAIK, S. S., ROY, A. K., AND FARMER, B. L. A Molecular Dynamics Study of Epoxy-Based Networks : Cross-Linking Procedure and Prediction of Molecular and Material Properties. *Macromolecules 41*, 18 (2008), 6837–6842.

[124] VERLET, L. Computer Experiments on Classical Fluids. I. Thermodynamical Properties of Lennard-Jones Molecules. *Physical Review 159*, 1 (1967), 98–103.

[125] VLUGT, T. J., VAN DER EERDEN, J. P. J. M., DIJKSTRA, M., SMIT, B., AND FRENKEL, D. *Introduction to Molecular Simulation and Statistical Thermodynamics*, 1 ed. Delft, 2008.

[126] VUKOVIĆ, F., AND WALSH, T. R. Moisture ingress at the molecular scale in hygrothermal aging of fiber–epoxy interfaces. *ACS Applied Materials & Interfaces 12*, 49 (2020), 55278–55289.

[127] VUKOVIĆ, F., AND WALSH, T. R. Practical atomistic models of carbon fiber surfaces with tuneable topology and topography. *Composites Science and Technology 216* (2021), 109049.

[128] WANG, X., JIN, J., AND SONG, M. An investigation of the mechanism of graphene toughening epoxy. *Carbon 65* (2013), 324–333.

[129] WANG, Z., LIANG, Z., WANG, B., ZHANG, C., AND KRAMER, L. Processing and property investigation of single-walled carbon nanotube (swnt) buckypaper/epoxy resin matrix nanocomposites. *Composites Part A: applied science and manufacturing 35*, 10 (2004), 1225–1232.

[130] WEEKS, J. D., CHANDLER, D., AND ANDERSEN, H. C. Role of repulsive forces in determining the equilibrium structure of simple liquids. *The Journal of Chemical Physics 54*, 12 (1971), 5237–5247.

[131] WHITE, S. R., MATHER, P. T., SMITH, M. J., ENGINEERING, A., AND BEACH, R. Characterization of the Cure-State of DGEBA-DDS Epoxy Using Ultrasonic, Dynamic Mechanical, and Thermal Probes. *Polymer Engineering and Science 42*, 1 (2002), 51–67.

[132] WIGNALL, G. D., AND LONGMAN, G. W. Investigation of short range ordering in polymers by means of radial distribution functions derived from X-ray diffraction Part 1 Bisphenol-A polycarbonate. *JOURNAL OF MATERIALS SCIENCE 8* (1973), 1439–1448.

[133] WOOD, W. W., AND PARKER, F. R. Monte Carlo Equation of State of Molecules Interacting with the Lennard-Jones Potential. I. A Supercritical Isotherm at about Twice the Critical Temperature. *The Journal of Chemical Physics 27*, 3 (1957), 720.

[134] WU, C., AND XU, W. Atomistic molecular modelling of crosslinked epoxy resin. *Polymer 47*, 16 (2006), 6004–6009.

[135] YAGYU, H., AND UTSUMI, T. Coarse-grained molecular dynamics simulation of nanofilled crosslinked rubber. *Computational Materials Science 46*, 2 (2009), 286 – 292.

[136] YELASH, L., VIRNAU, P., BINDER, K., AND PAUL, W. Three-step decay of time correlations at polymer-solid interfaces. *Europhysics Letters 98* (2012), 28006.

[137] ZHAO, Z., TENG, K., LI, N., LI, X., XU, Z., CHEN, L., NIU, J., FU, H., ZHAO, L., AND LIU, Y. Mechanical, thermal and interfacial performances of carbon fiber reinforced composites flavored by carbon nanotube in matrix/interface. *Composite Structures 159* (2017), 761–772.